

Masterarbeit
von cand. M. Sc. Saeed Izadi

**Charakterisierung von Druckzerstäubern für einen Einzeldüsen-flüssig-
FLOX[®]-Brenner mit Hilfe optischer und Laserdiagnostik**

Februar 2018

ausgegeben von
Prof. Dr.-Ing. M. Aigner
Institut für Verbrennungstechnik der Luft- und Raumfahrt (IVLR)
Universität Stuttgart

mitbetreut und angefertigt bei
Dr. Oliver Lammel
Deutsches Zentrum für Luft und Raumfahrt e.V. (DLR)

Master Thesis

by cand. M. Sc. Saeed Izadi

**Characterization of Pressure Atomizers for a
Single Nozzle Liquid FLOX® Burner Using
Optical and Laser Diagnostics**

February 2018

Issued by

Prof. Dr.-Ing. M. Aigner

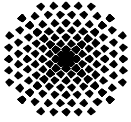
Institute of Combustion Technology for Aerospace Engineering (IVLR)

University of Stuttgart

Supervised by

Dr. Oliver Lammel

German Aerospace Center (DLR)



Masterarbeit

für Herrn cand. aer. Saeed Izadi

Charakterisierung von Druckzerstäubern für einen Einzeldüsen-flüssigFLOX[®]-Brenner mit Hilfe optischer und Laserdiagnostik

Aufgabenstellung:

Am Institut für Verbrennungstechnik des Deutschen Zentrums für Luft- und Raumfahrt e.V. (DLR) in Stuttgart wird ein Range Extender (REX) für elektrische Fahrzeuge entwickelt. Dieser soll auf einer Mikrogasturbine (MGT) basieren. Durch die Integration von 3 neuartigen FLOX[®]-basierten Einzeldüsenbrennern in eine C30 MGT der Firma Capstone soll eine deutliche Reduktion der Schadstoffemissionen erreicht werden. Die MGT soll eine elektrische Leistung von 30 kW liefern, was einer thermischen Leistung von 115 kW entspricht. Als Brennstoff soll Heizöl als Dieselerersatz verwendet werden. Ein Rekuperator innerhalb der MGT dient zur Vorheizung der Prozessluft auf 460°C vor dem Eintritt in die Brennkammer. In einem ersten Schritt wird im Rahmen dieser Masterarbeit ein Einzeldüsenbrenner untersucht. Insbesondere soll der Einsatz handelsüblicher Druckzerstäuber erprobt werden. Frühere Arbeiten haben gezeigt, dass hohe Vorheiztemperaturen dabei oft zu Verkokungen am Düsenaustritt führen und somit signifikanten Einfluss auf die Brennstoffverteilung haben. Um die Qualität der Zerstäubung und deren Auswirkung auf die Flamme bei hohen Eintrittstemperaturen zu untersuchen, muss eine systematische Untersuchung unterschiedlicher Zerstäuber mittels optischer Messtechnik unter Laborbedingungen erfolgen. Dazu wird die Flammencharakteristik unter den typischen Bedingungen einer MGT erfasst.

Arbeitsschritte:

- Einarbeitung in das Themengebiet/Literaturrecherche
- Recherche und Auflisten einer Reihe von handelsüblichen Druckzerstäubern
- Aufbau eines reaktiven atmosphärischen Prüfstands für hohe Vorheiztemperaturen
- Aufbau laserbasierter- und optischer Messtechnik (Mie-Streuung und OH*-Chemolumineszenz)
- Durchführung von systematischen OH*- Chemolumineszenz Messungen zur Untersuchung von Flammeneigenschaften
- Durchführung von einzelnen Mie-Streuungsmessungen
- Auswertung der Messungen
- Diskussion und Dokumentation

Ort und Dauer:

Die Studienarbeit ist am IVLR durchzuführen und innerhalb von 6 Monaten abzuschließen.

Betreuer:

Dr. Oliver Lammel

Ausgabe: 17.10.2017

Abgabe: 26.02.2018

Prof. Dr.-Ing. M. Aigner

Eigenständigkeitserklärung

Hiermit versichere ich, dass ich diese Masterarbeit

1. selbstständig mit Unterstützung des Betreuers Dr. Oliver Lammel angefertigt habe,
 2. keine anderen als die angegebenen Quellen benutzt und alle wörtlich oder sinngemäß aus anderen Werken übernommenen Aussagen als solche gekennzeichnet sind,
 3. dass die eingereichte Arbeit weder vollständig noch in wesentlichen Teilen Gegenstand eines anderen Prüfungsverfahrens gewesen ist,
 4. dass die Arbeit weder vollständig noch in Teilen ohne Zustimmung der Prüferin bzw. des Prüfers bereits veröffentlicht wurde,
 5. dass das elektronische Exemplar mit den anderen Exemplaren übereinstimmt,
 6. dass ich bei der Erstellung der Arbeit die einschlägigen Bestimmungen zum Urheberschutz fremder Beiträge entsprechend den Regeln guter wissenschaftlicher Praxis eingehalten zu haben.
- Soweit meine Arbeit fremde Beiträge (z.B. Bilder, Zeichnungen, Textpassagen etc.) enthält, habe ich diese Beiträge als solche gekennzeichnet (Zitat, Quellenangabe) und eventuell erforderlich gewordene Zustimmungen der Urheber zur Nutzung dieser Beiträge in meiner Arbeit eingeholt. Mir ist bekannt, dass ich im Falle einer schuldhaften Verletzung dieser Pflichten die daraus entstehenden Konsequenzen zu tragen habe.

Stuttgart, 26.02.2018,.....Saeed Izadi

Kurzfassung

In einem Einzeldüsen-FLOX[®]-Brenner wurde der Einfluss einer Reihe von handelsüblichen Druckzerstäubern auf die Flammenstruktur experimentell untersucht. Das Hauptaugenmerk lag in der Anwendbarkeit bei hohen Luftvorwärmtemperaturen. Diese hohen Eintrittstemperaturen sind charakteristisch für den geplanten Einsatz in der Brennkammer einer Mikrogasturbine mit Rekuperator, die als Range Extender Unit für elektrisch betriebene Kraftfahrzeuge verwendet werden soll. Als Brennstoff wurde extra leichtes Heizöl (als Ersatz für Diesel) genutzt.

Für flüssige Brennstoffe sind Untersuchungen zur Flammenstabilisierung sowie zur Brennstoffzerstäubung und Verdunstung der Tropfen unerlässlich, um eine stabile und zuverlässige Verbrennung zu gewährleisten. Der Einsatz optischer und laserdiagnostischer Methoden ermöglicht es, die Auswirkungen der Zerstäubung auf die Flammen zu verstehen, was zur Optimierung des Verbrennungsprozesses genutzt werden kann.

Die hier vorgestellte Studie befasst sich mit Designparametern, die Flammenlage und -stabilität beeinflussen. Bei atmosphärischem Druck wurde der Brenner in weiten Parameterbereichen betrieben: Variationen a) des Brennstoffeindüsungspunkts (Abstand der Brennstofflanze vom Mischdüsenaustritt) im Bereich von 0 – 16 cm, b) der Luftzahl λ (1 – 2,3), c) der Luftvorheiztemperatur (460 – 530°C), sowie d) der Luftgeschwindigkeit (80 – 120 m/s). Insgesamt wurden 6 verschiedene Druckzerstäuber getestet. Die thermische Leistung der Flammen betrug 9 – 50 kW. Während alle getesteten Injektoren bei hohen Luftvorwärmtemperaturen keine Verkokung zeigten, hatten einige Injektoren einen begrenzten Arbeitsbereich, bevor extreme thermoakustische Pulsation auftraten.

Während der Variation der Design- und Betriebsparameter wurde die Lage der Wärmefreisetzung mit OH* Chemolumineszenz gemessen, um das Flammenverhalten zu untersuchen. Aus den gemittelten Bildern der OH* CL wurden die flammenstrukturellen Eigenschaften extrahiert, aufgezeichnet und ausgewertet. Die Ergebnisse zeigten, dass die Flammenabhebehöhe abnahm, wenn die Brennstofflanze weiter zurückgezogen wurde. Dies bewirkte eine verbesserte Verdunstung der Brennstofftropfen im Brennerplenum.

Zusätzlich wurden Mie-Streuungsmessungen für einen ausgewählten Druckzerstäuber durchgeführt, um die Verteilung der Brennstofftropfen an der Luftdüse zu visualisieren. Dazu wurden die Luftzahl und die Tiefe der Brennstofflanze variiert.

Abstract

In a single nozzle FLOX[®] burner, the influence of a series of commercially available off-the-shelf pressure atomizers on the flame structural properties was experimentally investigated. The main focus was on the operability of the injectors at high air preheating temperatures. These high inlet temperatures are characteristic for the planned application in the combustion chamber of a micro gas turbine with an exhaust gas heat recuperator, which will be deployed as a range extender unit for electrically driven vehicles. The fuel used was extra-light heating oil as a substitute for diesel.

For liquid fuels, investigations of flame stabilization as well as fuel atomization and droplet vaporization are vital to establish a steady and reliable combustion. The usage of optical and laser diagnostic methods allows the understanding of the impact of atomization on flames, which in return enables the optimization of the combustion process.

The present study seeks the understanding of the design parameters that influence flame shape and stability. At atmospheric pressure, the combustor was operated within a wide range of operating conditions: variations of a) the fuel injection point (distance of the fuel lance from the mixture nozzle exit) in a range of 0 – 16 cm, b) the air equivalence ratio λ (1 – 2.3), c) the air preheat temperature (460 – 530°C), as well as d) the air velocity (80 – 120 m/s). Overall, 6 different pressure atomizers were tested. The thermal powers of the combustor covered 9 – 50 kW. While all of the tested injectors showed no coking at high air preheat temperatures, a few injectors had limited operating range, before extreme thermos-acoustic pulsation were encountered.

OH* chemiluminescence was used to detect the position of the heat release zone within the combustion chamber while design parameters were varied. From OH* chemiluminescence averaged images, flame structural properties were extracted, plotted and evaluated. The results showed an upstream shift of the flame base as fuel lance was moved away from the nozzle exit. This was characterized as improved fuel droplet vaporization within the burner plenum.

In addition, Mie scattering measurements were done for one of the best performing pressure atomizers to visualize the fuel drop distribution at the burner head. The air equivalence ratio and fuel lance depth were varied to study their effect on fuel drop evaporation. The Mie scattering results showed increased fuel drop evaporation while the fuel lance was placed at a lower position.

Acknowledgements

I would also like to express my sincere gratitude to my supervisor Dr. Oliver Lammel for his continuous and highly qualified guidance. The regular meetings and his valuable direction always helped me with the progress of my work. I am grateful to Oliver for giving me the opportunity to work on this project.

Special thanks to Dominik Schäfer, who tirelessly helped me to operate and troubleshoot the test rig. I am grateful for all of the support Jochen Eichhorn offered me throughout the experiments. Lots of thanks to Dr. Holger Ax for his instructions. I appreciate the time and the effort of all of the Combustion Diagnostic department staff for making this work possible.

Finally, I would like to thank my family: Anna and Helena. Thank you for your support, encouragement, and for being there for me.

Dankeschön.

Saeed Izadi

Stuttgart 2018

Table of Contents

1 Introduction.....	1
1.1 Battery Electric Vehicles	1
1.2 Extended Range Electric Vehicles.....	3
1.3 Micro Gas Turbine Engines	4
1.4 FLOX® Gas Turbine Burners	7
1.5 Atomizing Nozzles.....	8
1.6 Liquid Pressure Atomizer	10
1.6.1 Plain orifice.....	11
1.6.2 Pressure-Swirl (Simplex).....	11
1.6.3 Duplex.....	12
1.7 Motivation of the Work	13
2 Basics & Current State of the Research	14
2.1 Basics of Atomization Theory	14
2.2 Fundamentals of Combustion Technology	18
2.3 Basics of Low-Emission Combustion.....	20
2.4 Previous Work	23
3 Experimental Setup	26
3.1 Single Nozzle Burner for Range Extender.....	26
3.2 Combustion Chamber	28
3.3 Premixture Plenum.....	29
3.4 Fuel Lance.....	30
3.5 Air Nozzles	31
3.6 Fuel Nozzles.....	32
3.7 Experimental Infrastructure	33
4 Measurement Tools.....	36
4.1 OH* Chemiluminescence	36
4.2 Conventional RGB Camera	38
4.3 Mie Scattering.....	39
5 Data Evaluation and Results.....	42
5.1 Operation Limits	42
5.2 Overall Flame Structure Visualization.....	44
5.3 OH*-Chemiluminescence Measurements.....	47

5.3.1 Data Evaluation.....	47
5.3.2 Air Equivalence Ratio Variation.....	53
5.3.3 Preheat Temperature Variation.....	58
5.3.4 Air Velocity Variation	60
5.3.5 Fuel Lance Depth Variation.....	63
5.4 Nozzle Pressure Drop	65
5.5 Mie Scattering Measurements.....	67
6 Error Assessment	70
7 Summary, Conclusions, and Recommendation.....	73
7.1 Summary.....	73
7.2 Conclusions.....	74
7.3 Recommendation	75
8 References	74
9 Appendices.....	78
Appendix 1 Mie Scattering.....	79
Appendix 2 Averaged OH*-CL Images	81
Appendix 3 RMS OH*-CL Images.....	94
Appendix 4 Graphs: Flame Structural Properties	103

List of Tables

Table 2.1 Combustion parameters of Gounder's experiments [2016, Gounder et al.]	24
Table 3.1 Summary of the fuel nozzle examined within the scope of this work - * at 10 bars - ** at 10 bars, kin. viscosity $\nu = 3.4 \text{ mm}^2/\text{s}$, density $\rho = 840 \text{ kg/m}^3$ - *** at 3 bars	32
Table 4.1 Formation reactions of the excited hydroxyl radical (OH^*) and the methylidyne radical (CH^*) and their characteristic wavelengths [2010, Ballester <i>et al.</i>]	37
Table 5.1 Overview of burner and combustion parameters	43
Table 5.2 List of maximum applied λ for all nozzles at various air velocities; maximum applied λ for the nozzle Dan45°S corresponds with its LBO	43
Table 5.3 Overview of the divider factors and threshold correction of each camera and image	51
Table 5.4 List of investigated nozzles with their nominal pressure drop and the corresponding flow capacity	66

List of Figures

Figure 1.1 New York taxi cab in about 1901, a battery electric vehicle [2012, Larminie <i>et al.</i>]	2
Figure 1.2 Schematic of an extended range electric vehicle powertrain showing its characterizing parts [2010, Lu <i>et al.</i>]	4
Figure 1.3 Overview of MGT main components and working cycle; a) characterizing components of the Capstone C30 micro gas turbine engine, b) schematic working principle of a recuperated MGT, c) T-s diagram of a recuperated MGT, showing a Brayton cycle [2010, C30-Datasheet, 2012, Friedrich <i>et al.</i>]	5
Figure 1.4 A typical FLOX [®] burner in a circular 12-nozzle alignment, with quartz glass wall configuration [2012, Roediger <i>et al.</i>]	8
Figure 1.5 Typical atomization process [1980, Bachalo]	10
Figure 1.6 Swirl distributor and chamber of simplex atomizer, top view (left), side view (right) [2000, Delavan-Nozzles]	11
Figure 1.7 A cut view of a simplex pressure nozzle (left); spray shape configurations (right) [2000, Delavan-Nozzles]	12
Figure 1.8 Basic principles of pressure atomizers, plain-orifice, simplex, and duplex [2017, Lefebvre <i>et al.</i>]	13
Figure 2.1 Emissions characteristics of gas turbine engines as a function of percent of takeoff power (100% = maximum fan rotation speed) and engine fuel consumption [2010, Lefebvre <i>et al.</i>]	22
Figure 2.2 Zizin's burner with Ø20mm air nozzle (left), vaporizer with 12 - nozzle burner (right) [2015, Zizin <i>et al.</i>]	24
Figure 2.3 Setup of Schäfer's two-nozzle FLOX [®] burner [2017, Schäfer]	25
Figure 3.1 Single nozzle burner along with other equipment used during the experiments	27
Figure 3.2 Detailed dimensions of the combustor along with the fuel lance and the air nozzle	29
Figure 3.3 Cross-section of burner's premixture plenum	30
Figure 3.4 Demonstration of fuel lance depth variation, a) 0 cm, b) 1 cm, c) 8 cm, and d) 16 cm	31

Figure 3.5 Overview of air nozzles; left) conical , right) semi-conical	31
Figure 3.6 Examined fuel nozzles; a) Danfoss oil nozzle [2014, Danfoss], b) Steinen oil nozzle [2016, Steinen], c) DIVA.....	33
Figure 3.7 Schematics of Coriolis flow sensor [CORI-FLOW-Data-Sheet]	34
Figure 3.8 Overview mini CORI-FLOW™ along with its components.....	34
Figure 3.9 Screenshot of the developed VI used for controlling the MFCs and monitoring pressures and temperatures	35
Figure 4.1 a) View areas of the Roper ICCD cameras on the burners cross section; b) sketch of the OH*- chemiluminescence imaging setup	38
Figure 4.2 Mie scattering intensity (a.u.) as a function of scattering angle [1993, Singham <i>et al.</i>]: Mie scattering intensity highest at 0° scattering angle and decays by increasing scattering angle	40
Figure 4.3 Setup of the Mie scattering experiment.....	41
Figure 5.1 Maximum applied air equivalence ratio λ of the nozzles as a function of the air velocity at various lance depth positions	44
Figure 5.2 Overall view of the Dan45°S flames at $T_{pre} = 460^{\circ}\text{C}$, different velocities, air equivalence ratios λ , and fuel lance depths.....	46
Figure 5.3 Camera characteristics correction and statistical processing of OH* emissions of the upstream part of the flame: a) 5 instantaneous images captured within 1 second, b) dark and white field corrected images, c) averaged image, d) threshold version of the average image, e) RMS image, f) threshold version of the RMS image	48
Figure 5.4 Iterative procedure of finding an intensity correction factor for the upper camera; a) overlapping area of one of the 10 selected averaged images, b) contour plot of the averaged image with magnification of its overlapping area, c) contour plot of the upper image.....	50
Figure 5.5 Flame structural properties extraction method used for determination of flame height, axial position of maximum intensity, and lift-off height	52

Figure 5.6 Influence of an air equivalence ratio sweep on flame heat release intensity by means of averaged OH*-CL images of Dan45°S at constant $v_{air}=100$ m/s, $T_{pre}=460^{\circ}\text{C}$, Lance 0 cm (upper images), 2 cm (lower images), max count scale 1400.....	53
Figure 5.7 Assumed explanation of the wider flame of Dan45°S at lance depth 0 cm, operated at $v_{air}=100$ m/s and $T_{pre}=460^{\circ}\text{C}$	54
Figure 5.8 Graphs of lift-off height (left) and flame height (right) of Dan45°S at $v_{air}=100$ m/s and $T_{pre}=460^{\circ}\text{C}$	55
Figure 5.9 Graphs of flame height (left) and lift-off height (right) of all of the nozzles at $v_{air}=100$ m/s and $T_{pre}=460^{\circ}\text{C}$	57
Figure 5.10 RMS OH*-CL images showing flame fluctuations of Dan45°S at constant $v_{air}=100$ m/s, $T_{pre}=460^{\circ}\text{C}$, lance 0 cm (upper images), 2 cm (lower images).....	58
Figure 5.11 Effect of preheat temperature on flame height (left) and lift - off height (right) of various fuel nozzles measured at constant $v_{air}=100$ m/s, 8 cm lance depth and $\lambda=1.7$	60
Figure 5.12 Effect of the air velocity (upper graphs) as a function of air equivalence ratio on flame height (left graph) and flame lift-off height (right graph) for Dan45°S at 0 cm lance depth and $T_{pre}=460^{\circ}\text{C}$; OH*-CL averaged images (lower images) along with RGB photos of flames at $v_{air}=80-120$ m/s, $\lambda=1.7$ $T_{pre}=460^{\circ}\text{C}$, and lance depth of 0 cm	61
Figure 5.13 Representation of flame height (left) and lift-off height (right) of DIVA as a function of air equivalence ratio $\lambda=1.3-2.3$ and air velocity $v_{air}=80-120$ m/s at constant $T_{pre}=460^{\circ}\text{C}$ and 8 cm lance depth.....	63
Figure 5.14 Graph demonstrating the effect of a fuel lance depth variation on the flame lift-off height (upper right) and overall intensity of flames over the height above the burner (upper left); OH*-CL averaged images (lower right) at various lance depth positions of Dan45°S at constant $v_{air}=100$ m/s, $T_{pre}=460^{\circ}\text{C}$, and $\lambda=1.5$	64
Figure 5.15 Air equivalence ratio variation of all the examined nozzles' pressure drop (left) and flame lift-off height (right) at constant $T_{pre}=460^{\circ}\text{C}$ and $v_{air}=100$ m/s	66
Figure 5.16 Normalized Mie scattering averaged images of Dan45°H placed on the air nozzle for variation of air equivalence ratio λ and constant $T_{pre}=460^{\circ}\text{C}$, $v_{air}=100$ m/s, and 1 cm lance depth	68

Figure 5.17 Normalized Mie scattering averaged images of Dan45°H placed on the air nozzle for variation of lance depth 1 cm (left) and 8 cm (right) at constant $T_{\text{pre}} = 460^{\circ}\text{C}$, $v_{\text{air}} = 100 \text{ m/s}$, and $\lambda = 1.8$69

List of Abbreviations and Symbols

Abbreviation	Full Meaning
AC	Alternating Current
AN	Air Nozzle
APMI	Axial Position of Maximum Intensity
AVG	Average
BEV	Battery Electric Vehicle
C ₂ *	Diatomic Carbon Radical
C30	Capstone Micro Gas Turbine Model 30 kW _{el}
CC	Combustion Chamber
CH*	Methylidyne Radical
CH ₄	Methane
CO	Carbon Monoxide
CO ₂	Carbon Dioxide
CO ₂ *	Carbon Dioxide Radical
DC	Direct Current
DLR	Deutsches Zentrum für Luft- und Raumfahrt (German Aerospace Center)
EREV	Extended Range Electric Vehicle
FH	Flame Height
FLOX [®]	Flameless Oxidation
FN	Flow Number / Fuel Nozzle
GPH	US Gallon per Hour
H ₂ O	Water (Vapor)
HAB	Height Above Burner
HIPOT	High Pressure Optical Test Rig
ICCD	Intensified Charge-Coupled Device
ICE	Internal Combustion Engine
LBO	Lean Blow Out
Li-ion	Lithium-ion
LOH	Lift-Off Height
MFC	Mass Flow Controller
MGT	Micro Gas Turbine

MMD	Mass Mean Diameter
N ₂	Nitrogen
Nd:YAG	Neodymium-Doped Yttrium Aluminum Garnet
NO	Nitric Oxide
NO ₂	Nitric Dioxide
NO _x	Nitric Oxide + Nitric Dioxide
NVH	Noise Vibration Harshness
O ₂	Oxygen
Oh	Ohnesorge Number
OH*-CL	Hydroxyl Radical Chemiluminescence
PNG	Image Format: Portable Network Graphic
Re	Reynolds Number
REX	Range Extender
RGB	Red-Green-Blue
RMS	Root Mean Square
SMD	Sauter Mean Diameter
TIT	Turbine Inlet Temperature
UHC	Unburned Hydrocarbon
VI	Virtual Instrument
We	Weber Number

Subscript	Meaning
------------------	----------------

a	Air Core
crit	Critical
L	Liquid
MAX	Maximum
O	Orifice
pre	Preheat
rel	Relative
SI	International System of Units
st	Stoichiometric

Symbol	Meaning	Unit
A	Area	(m ²)
c	Speed of Light	(m/s)
C _D	Drag Coefficient	(-)
D	Diameter	m
F	Force / Mass of Fuel	(N) / (kg)
g	Gaseous	
h	Planck Constant	(J s)
H	Hollow	
O	Mass of Oxidizer	(kg)
R	Radius / Reaction	(m) / -
S	Solid	
T	Temperature	(°C)
t	Film Thickness	(m)
v	Velocity	(m/s)
x	Size of Scattering Particle	(-)
λ	Wave Length	(m)
ν	Kinematic Viscosity	(mm ² /s)
η	Dynamic Viscosity	(Pa s)
θ	Cone Half Angle	(°)
λ	Air Equivalence Ratio / Wavelength	(-) / (m)
ρ	Density	(kg/m ³)
σ	Surface Tension	(N/m)
φ	Equivalence Ratio	(-)

1 INTRODUCTION

1.1 Battery Electric Vehicles

Battery electric vehicles (BEVs) are among the most commonly investigated technologies of modern transportation. It is generally accepted that BEVs could replace the current internal combustion engine (ICE) vehicles as the sole driver of transport worldwide. Battery electrically driven motors have the potential to substitute ICEs as they offer a variety of advantages that are very appealing to manufacturers.

Some remarkable features of BEVs are their reduced noise and pollution; they also offer higher efficiencies considering their motor, converting electric power into mechanical. This can help reduce the dependency of transport on oil – considering that the power comes from sources other than oil. The energy for electric vehicles is required to be produced from non-fossil-fuel sources such as alternative energy sources in order to achieve zero carbon emissions.

Well over a century ago, electric vehicles, as shown in Figure 1.1, were among the first personal vehicles to roll their wheels on the roads as there was not yet an efficient, compact, and at the same time sufficiently lighter alternative powertrain to be fitted into a personal vehicle. With the gradual improvements in the internal combustion engines, battery electric vehicles gave their place to pure ICE driven vehicles. Currently, other electric transportation vehicles such as trains are among the most well-developed wired electric vehicles. Meanwhile, street transport has recently found its point where major vehicle manufacturers are setting their plans to produce electric cars, both full-battery and hybrid cars in increasing numbers.



Figure 1.1 New York taxi cab in about 1901, a battery electric vehicle [2012, Larminie *et al.*]

Smaller transportation vehicles such as bicycles and golf buggies have enjoyed wider use of electric drive, whereas road vehicles are taken over by the vastly successful ICEs, which generally cover much longer ranges and are easily refueled. Improving BEV's core technology, i.e. its batteries, can lead to a breakthrough in BEV's acceptability by the consumers. In his analysis of electric vehicles, [2010, Mock] reports significant development of the technology in the near future, especially in Li-Ion battery technology that is currently promising great technical potentials.

The core problem of a BEV is its range and charge time, which are the two main reasons for the common consumers not to fully treat BEVs as a typical transportation. Finding a viable solution on how to extend the range of the vehicle without compromising the idea of low-cost and low-emission is not easy. Therefore, researchers are stretching their knowledge to meet the requirements of lighter structure weights and lower battery production costs.

Obtaining an acceptable charge time is crucial for securing the future of BEVs as it plays an important role on whether or not electric vehicles can be socially accepted. The fear of running out of charge in the middle of nowhere is the primary challenge that manufacturers are required to address before introducing their BEV to the consumers' market. This particular issue is supplemented by the charge time, which has not been fully resolved. The concept of extending the range of the electric vehicles using an additional internal combustion system promises great potentials.

1.2 Extended Range Electric Vehicles

An alternative solution, though somewhat regressive, is the use of a range extender (REX) unit that recharges the batteries when it is necessary. Such approach might not be at first the most efficient way of solving the current challenges of the pure BEVs but it indeed helps to fill the shortcomings of them. As a result, a new concept known as Extended Range Electric Vehicles (EREV) or hybrid vehicles are developed.

REX units assist/recharge the batteries in long travels or at higher speed ranges. Researchers currently seek the best option for a range extender unit that can provide EREVs a sufficient range and recharge time. Some of REX technologies are:

- Micro gas turbine
- 2 & 4 stroke ICE (both diesel & gasoline)
- Fuel cell
- Free-piston engine
- Rotary engine (Wankel)

Each of these technologies holds key advantages to the other by promising smaller packaging, higher power density, lower operation costs, better emissions, broader fuel flexibility, better scalability, improved noise vibration harshness (NVH), and higher efficiency [2012, Friedrich *et al.*]

As schematically depicted in Figure1.2, an EREV is composed of parts of an ICE powered vehicles as well as battery electric vehicles. A set of batteries provide enough power for the vehicle to reach a certain range; however, having an ICE on board allows for using extra mechanical power to boost the vehicle's range and/or speed up its charge time. The engine's mechanical power is converted into electrical power using a generator. A rectifier is then used to convert the generator's alternating current (AC) into direct current (DC). Finally, a DC powered traction motor is used to drive the vehicle.

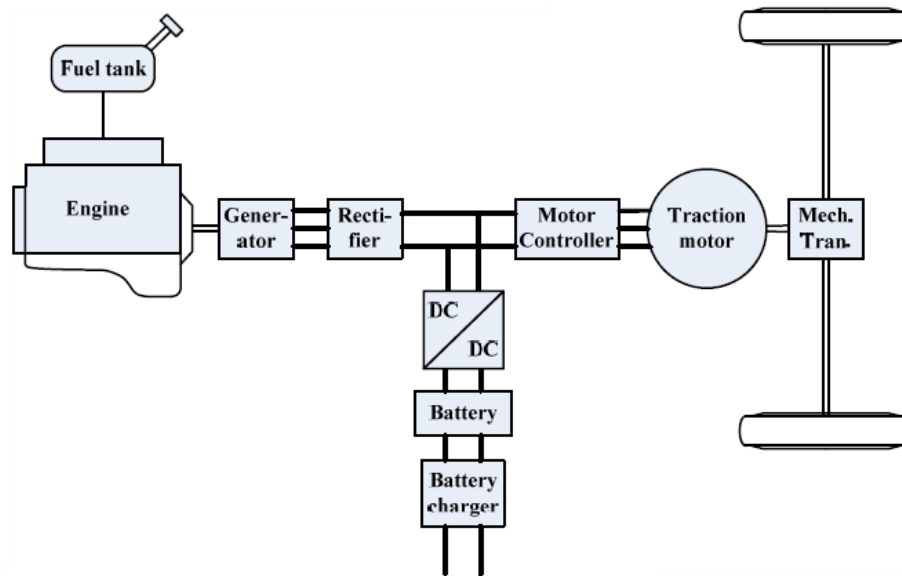


Figure 1.2 Schematic of an extended range electric vehicle powertrain showing its characterizing parts [2010, Lu *et al.*]

Two crucial selection criteria of REX units are their efficiency and emissions. A thorough study [2012, Friedrich *et al.*] conducted by Institute of Vehicle Concepts of DLR Stuttgart evaluated and compared different REX technologies for their proper application potentials. For instance, the study covered which of the REX technologies are better suited for different vehicle concepts.

Originally, range extender vehicles were designed as serial hybrids, i.e. the ICE drives the electrical generator when it is needed. [2014, Kinigadner *et al.*] reported that the overall efficiency of serial hybrids is not only dependent on the efficiency of the engine and the generator, but also charging and discharging losses of the battery. The efficiency of the overall EREV drops at high driving speeds due to power conversion losses, if REX unit drives the vehicle directly [2007, Kirchner].

1.3 Micro Gas Turbine Engines

Micro gas turbines (MGTs) are set to carry a vital role in the future of hybrid electric vehicles. As illustrated in Figure 1.3 a), MGTs are integrated power plants that consist of a generator, a compressor, usually a recuperator, a combustion chamber (CC), a turbine, and power electronics [1999, Hamilton]. Figure 1.3 b) describes MGT's working principle, where air is

sucked into a compressor (1) and then led through a recuperator (2). Within the recuperator, heat is exchanged between the turbine's (4) exhaust gas and the compressed air. The preheated compressed air enters the combustion chamber (3) where air is drastically heated up and directly toward the turbine blades, so that the blades can extract air's enthalpy. The extracted energy is then converted into mechanical power and subsequently to electrical using a generator (6). Finally, turbine exhaust gas runs through the recuperator and lastly exits the unit through exhaust outlet (5).

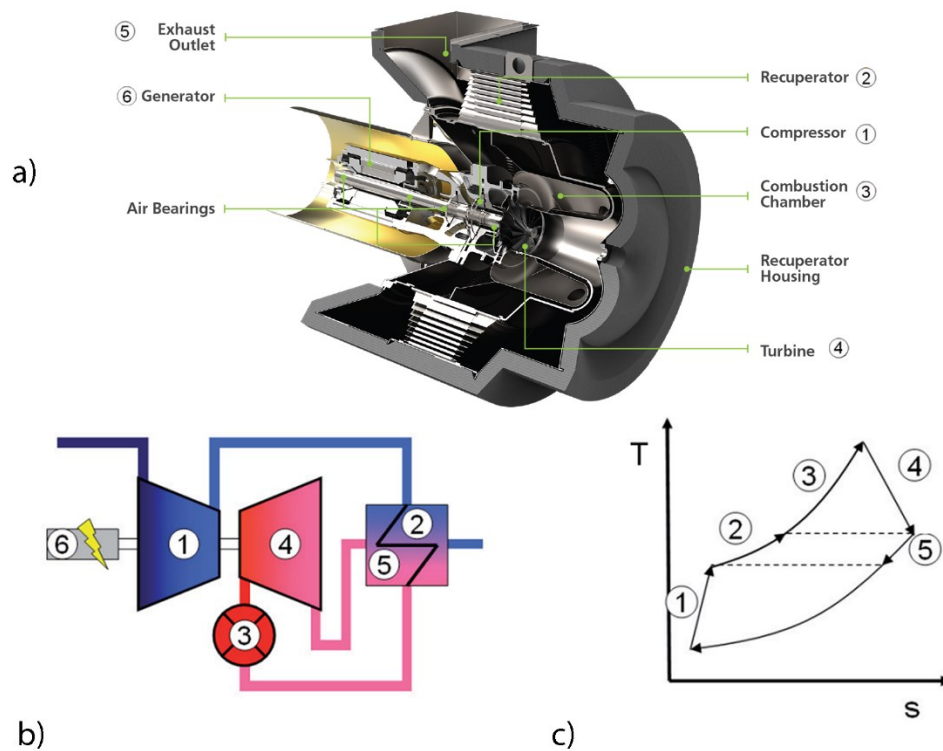


Figure 1.3 Overview of MGT main components and working cycle; a) characterizing components of the Capstone C30 micro gas turbine engine, b) schematic working principle of a recuperated MGT, c) T-s diagram of a recuperated MGT, showing a Brayton cycle [2010, C30-Datasheet, 2012, Friedrich *et al.*]

MGTs follow the Brayton cycle as an open system; the cycle is demonstrated in Figure 1.3 c) where each sequence is highlighted with the related component number. A typical power capacity of MGT generators ranges between 15 to 250 kW [2003, Hamilton].

Since the turbine inlet temperature (TIT) of MGTs is lower than an aircraft gas turbine engine due to absence of high-end materials and cooling used in the turbine section of the engine and

due to a low compression ratio ($\pi < 5$) realized, a lower efficiency is achieved that leads to use of a heat exchanger, which is usually referred to as a recuperator [2003, Hamilton]. The recuperator exchanges the excess exhaust heat to the compressed air before entering the combustion chamber. In addition, it is responsible for higher efficiency with simple components and relatively low operating temperatures.

Some of the features of MGTs are [2003, Hamilton]:

- Low maintenance
- Low NO_x emission levels (at full load operation)
- Fuel flexibility
- Modularity and scalability
- Low NVH
- High efficiency

A few disadvantage of a MGT recuperator are:

- Heavy weight and large volume
- High manufacture costs due to its complex construction

Lower maintenance

MGTs are commonly known for their distinctive “single moving part”. The rotating shaft that connects the generator and the compressor with the turbine is the only moving part in the engine which lowers maintenance to a significant level.

Low NO_x emission levels

It is recognized that MGTs emit extremely low NO_x among all generators, small or large. Some brands may show better emissions than others, however, comparing them to conventional ICE engines, they tend to achieve best emission results [2003, Hamilton].

Fuel flexibility

A striking feature of MGTs is its compatibility with a wide variety of fuels, including natural gas, propane, diesel, etc. Renewable fuels such as biogas add to its leading advantage among other REX units for its effect on economics and environment.

Modularity and scalability

A useful characteristic of a MGT unit lies in its scalability. By increasing the compressor and thus turbine power, a significant shift in operating point is achievable. When stacking multiple units next to each other along with a suitable control system, a surge in power output is realizable as well. This way, REX units can reach better efficiencies without making the system overly complicated.

Low noise, vibration and harshness NVH

Due to MGT's single moving part (shaft, compressor and turbine), it generates very little vibration and noise. This of course applies to the most modern models, as the old types of MGTs were very loud [2003, Hamilton].

High efficiency

Harnessing the thermal power of MGT's exhaust gas helps naturally to increase the electrical output of the generator. A numerical sensitivity analysis conducted by [2012, Friedrich *et al.*] regarding a typical MGT equipped with a recuperator shows that in case of using a recuperator with an efficiency of 90%, an increase of overall 2.5% efficiency on MGT is realizable.

There are many considerations that validate the superiority of MGTs with respect to emission levels and most importantly specific power. The robustness and design parameters are to be improved in the coming years as there are numerous researchers worldwide working on challenges facing this unique REX technology.

1.4 FLOX[®] Gas Turbine Burners

FLOX[®] (acronym for flameless oxidation) was discovered by accident during experiments in 1989 by J. A. Wüning. A primary advantage of flameless oxidation lies in its ability to suppress thermal nitric oxide formation even when air is highly preheated [Wüning].

FLOX[®] gas turbine burners typically consist of several air/fuel nozzles that are aligned in one or more concentric circles (see Figure 1.4). Fuel and air are partially premixed and fed into a combustion chamber without any swirl. The concept of aligning the fuel nozzles in circular matter creates a pronounced recirculation that helps to stabilize the flame. The intensive mixing by high velocities helps to homogenize the local mixture fraction, and thus, distributes the heat release and avoids temperature peaks that leads to decreasing thermal NO_x emission. A unique

characteristic of FLOX[®]-burners is their pronounced inner recirculation zone throughout the combustion chamber. In addition, a precise mixture ratio regulation within the combustion chamber allows for better emission levels. This is achieved as a result of temperature peaks prevention and homogenization of temperature distribution [2015, Meier].

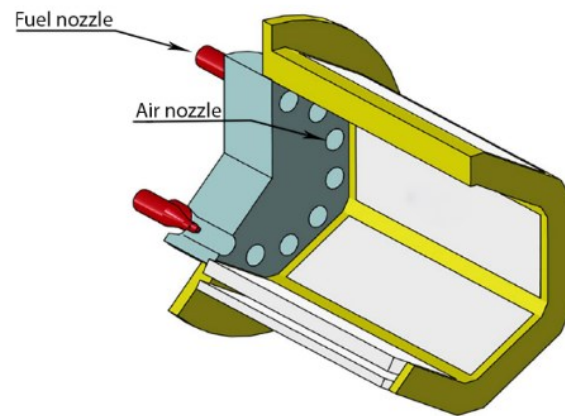


Figure 1.4 A typical FLOX[®] burner in a circular 12-nozzle alignment, with quartz glass wall configuration [2012, Roediger *et al.*]

Some of the FLOX[®] gas turbine burner potentials are [2015, Zanger *et al.*]:

- high fuel flexibility
- low exhaust gas pollutants
- high efficiency

A feasibility study conducted by [2015, Zanger *et al.*] regarding operation compatibility of a Turbec T100 MGT with the new FLOX[®] burner using natural gas showed a reliable operating behavior. However, it showed that the carbon monoxide (CO) emission levels were reduced whereas the nitric oxide (NO_x) emissions exceeded the emission levels of the standard MGT burner.

1.5 Atomizing Nozzles

The atomizing nozzle is one of the most important hardware parts in liquid fuel combustion systems. In spite of its tiny size, it carries partial responsibilities like combustion stability, emission levels, and burner efficiency. Some of the reasons for utilizing atomizing nozzles for combustion systems are [2015, Fansler *et al.*]:

- In order to make a combustible mixture of fuel and air, fuel must be first atomized to help its vaporization prior to the combustion process
- For establishing a steady flame, continuous supply of adequately atomized fuel must be fed into the combustion zone
- Easier ignition, higher volumetric heat release rates, and wider operational ranges can be achieved

Atomization is essentially a disruption of the consolidating influence of droplet surface tension by the action of internal and external forces [2010, Lefebvre *et al.*].

Fuel nozzles tend to break up the existing surface tension of liquids that pulls it together. Through surface tension, the liquid forms a sphere that requires the least surface energy. Once the consolidating surface tension of a droplet is exceeded, liquid can be disintegrated.

The process of atomization (also designated as spray) is achieved through several techniques. These techniques differ in construction or setup but basically deliver the same output, i.e. breaking up liquids into small droplets. In this process, a high-velocity stream of liquid is fed through an orifice and subsequently splashed by either a high-velocity flow of air or a rotating or vibrating mechanical part [2017, Lefebvre *et al.*].

A typical atomization process illustrated in Figure 1.5 details pressurized liquid fuel injection through a nozzle and the gradual creation of the spray. First stage of atomization starts with formation of a liquid sheet that depends on liquid properties, discharge coefficient, spray cone angle, spray sheet thickness, and turbulence characteristics. This stage is followed by instabilities within the liquid sheet and marks as the primary breakup of the injected liquid. Droplets start forming after the liquid sheet breakup that is followed by secondary breakup through drop collision and combination. Lastly, droplets are vaporized within the reaction zone in the combustion chamber.

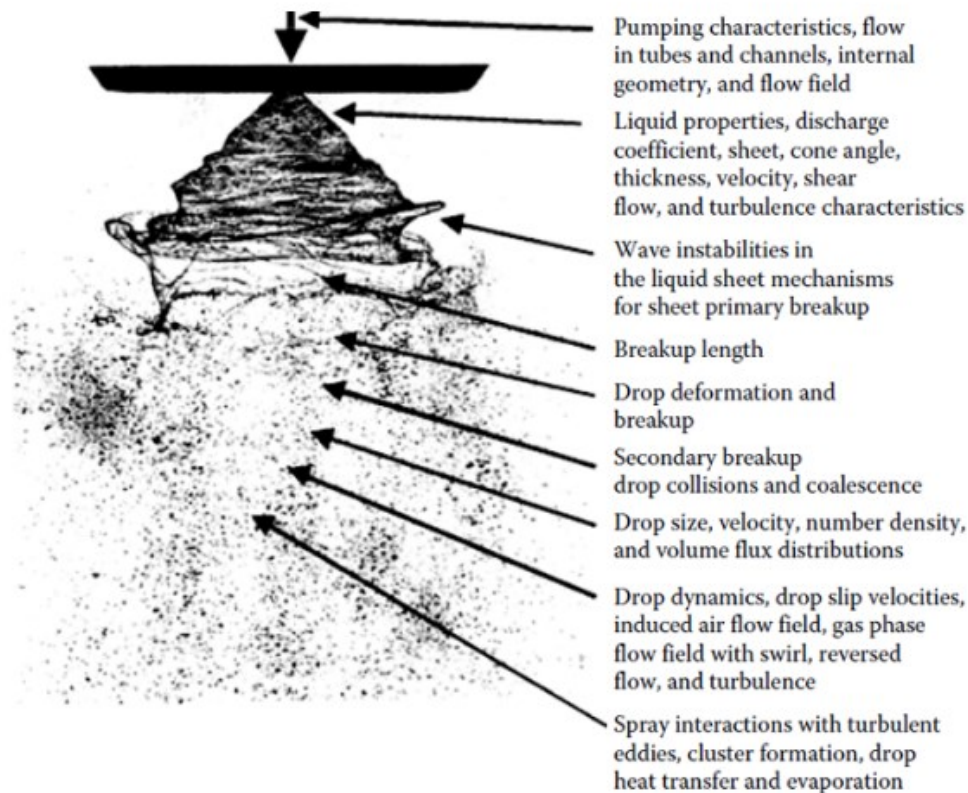


Figure 1.5 Typical atomization process [1980, Bachalo]

1.6 Liquid Pressure Atomizer

The simplest kind of pressure atomizers is the water sprayer that are used for every day uses. The concept of building a liquid pressure behind an opening orifice allows for disintegration of liquid into droplets as pressure energy is converted into kinetic energy (velocity). Atomizing liquids using pressure can be achieved in the following manners:

It is widely known that atomizing liquid fuel has its own boundaries. Realizing a fine spray and a thorough mixture are not easy tasks. Air, normally in turbulent condition, enters a 3-dimensional geometry and spreads accordingly to form a combustible mixture with the fuel. Attaining small drop sizes helps to evaporate and, thus, to trigger a complete chemical reaction, i.e. oxidation of the fuel [2006, Joos]. As a result, extensive researches are dedicated to improve the atomization process.

1.6.1 Plain orifice

By simply passing a high-pressure liquid through a hole, atomization is achieved. As easy as it sounds, the higher the pressure, the better the spray and the smaller the droplets. However, experiments have shown difficulties with orifices that are smaller than 0.3 mm in diameter due to deposition of particles in applications such as: turbojet afterburners, ramjets, and diesel engines [2017, Lefebvre *et al.*].

1.6.2 Pressure-Swirl (Simplex)

Plain-orifice atomizers produce a fairly narrow cone angles that are not favorable for some applications; pressure-swirl atomizers, on the other hand, have a much wider cone angle [2010, Lefebvre *et al.*].

Liquid flows through a swirl-generating chamber prior to a circular orifice to produce a fine mist. In pressure-swirl (simplex) nozzles, atomization is accomplished by releasing the pressurized liquid through a set of slots or holes, which are tangentially cut to create a high angular velocity (rotation) inside the chamber (see Figure 1.6) caused by centrifugal forces [2000, Delavan-Nozzles]. An air core can thus be formed by the swirling liquid that is compelled out of the orifice under axial as well as radial forces. In addition, the hollow conical sheet stretches from the opening of the nozzle to the end of the swirl chamber (see Figure 1.7 right).

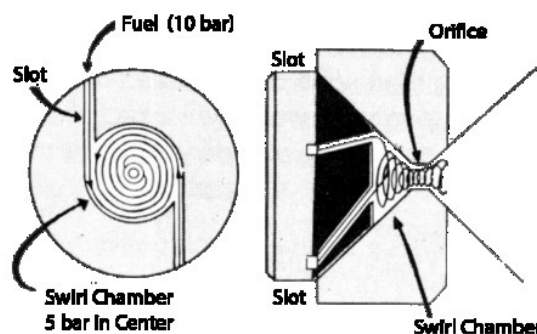


Figure 1.6 Swirl distributor and chamber of simplex atomizer, top view (left), side view (right) [2000, Delavan-Nozzles]

The atomized liquid occurs from the opening in a conical shape that gradually grows outward to the end of the spray [2017, Lefebvre *et al.*]. The cone angle can be varied by design and

often is provided in 6 standard angles: 30°, 45°, 60°, 70°, 80°, and 90° [2000, Delavan-Nozzles].

The finest droplets can be obtained by increasing the pressure and widening the spray angle [2017, Lefebvre *et al.*]. Figure 1.7 (left) shows a cut view of a typical simplex pressure nozzle along with its composing parts. Here, the pressurized fuel flows through a brass sintered filter prior to entering into a steel distributor that is equipped with tangential slots. These slots help forcing the liquid tangentially towards a swirl chamber that ends with an orifice. The fuel exits the nozzle in a shape of a hollow or a solid cone depending on the design of the nozzle.



Figure 1.7 A cut view of a simplex pressure nozzle (left); spray shape configurations (right) [2000, Delavan-Nozzles]

Beside the hollow cone simplex nozzles, there are solid cone sprayers that offer potentials of their own that are advantageous for some applications. Principally, both concepts function the same way, with the difference that an axial jet is needed to fill the hollow conical spray pattern [2017, Lefebvre *et al.*].

Simplex atomizers have a major disadvantage when it comes to increasing the liquid flow rate. [2010, Lefebvre *et al.*] report that the flow rate grows as the square root of the injection pressure differential. Thus, in order to double the flow rate, a fourfold of the injection pressure is needed.

1.6.3 Duplex

An important characteristic of a nozzle is that it should operate under various operating conditions without requiring very high pressures. As a result of simplex's drawback at higher flow rates, a new type of swirl pressure atomizer was developed, known as duplex. This kind

of nozzle allows higher flow rates at lower injection pressures than a simplex nozzle by simply supplying the swirl chamber over two sets of distributor slots, where each has its own source of liquid (see Figure 1.8) [2017, Lefebvre *et al.*]. In other words, duplex consists of two simplex nozzles placed into another. The two sets of slots are designated as primary, with smaller orifice, and secondary slots, with relatively larger orifice. The major objective of duplex is to allow the liquid flow through the primary slots at low flow rates and once the flow is increased, through opening a regulated valve, the secondary slots allow the liquid to enter into the swirl chamber [2011, Ashgriz].

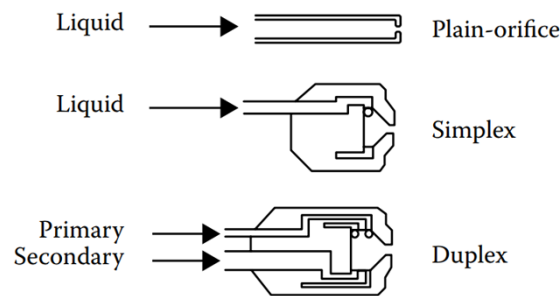


Figure 1.8 Basic principles of pressure atomizers, plain-orifice, simplex, and duplex [2017, Lefebvre *et al.*]

1.7 Motivation of the Work

This work focuses on finding a suitable off-the-shelf commercial fuel nozzle that can provide the operating conditions and meets the given specifications. A set of six pressure atomizers with a variety of spray cone angle and shape, flow capacity, and manufacturer along with two different air nozzles was investigated. Influence of individual nozzle on flame shape and heat release zones within the flame was to be measured for comparing purposes. Design parameters varied in this work are expected to have partial to major effects on flame behavior, which can help to understand the parameter interaction mechanisms.

2 BASICS & CURRENT STATE OF THE RESEARCH

2.1 Basics of Atomization Theory

Understanding the basics of atomization allows for further developing of combustion processes. Motivation on acquiring information regarding drop size, spray geometry, and angle has increased significantly in the recent years.

As previously mentioned, pressure atomizers use potential energy (pressure) to force a liquid through an orifice. This creates a fine mist of liquid that has an angle and a nozzle specific range of drop size and shape, which vary as the liquid properties change. In the literature, the range of drop sizes is usually referred to as drop size distribution.

Factors concerning how the drop size is affected are primarily:

- Nozzle capacity and type
- Fluid injection pressure and flow rate
- Fluid physical properties
- Spray shape and angle
- Fluid temperature

The solid cone sprayers typically produce the largest drop sizes, whereas hollow spray cone nozzles show better results in terms of size of the drops. The liquid injection pressure, as previously discussed, affects the atomization size in a reversed manner, i.e. smaller drops are achieved at greater pressures and vice versa. Another influencing factor is by changing the spray angle as different drop sizes can be realized by increasing and decreasing the angle. Likewise, liquid properties have remarkable influences on the spray quality. Low viscous liquids and, thus, increased surface tensions tend to make the atomization process more challenging in a way that the sum of energy needed to atomize the liquid increases, if the pressure energy is not sufficient enough. An increase in liquid temperature leads to lower

viscosity and consequently to smaller drop sizes. A further significant parameter for calculation and evaluation of an atomization processes is the drop mean diameter.

It is of vital importance to take the process of drop breakup into consideration. A few factors play important roles on how atomization is attained. An influencing factor is the Weber number, We , that describes the ratio of disruptive aerodynamic force to the consolidating surface tension force [2010, Lefebvre *et al.*]:

Aerodynamic force:

where,

F_D = Drag force, (N)

c_D = Drag coefficient, (-)

ρ_{air} = Air density, (kg/m³)

v_{rel} = relative velocity

(air to liquid), (m/s)

$$D = \text{Drop diameter, (m)} \quad F_D = \frac{1}{2} c_D \rho_{air} v_{rel}^2 \left(\frac{\pi}{4} \right) D^2 \quad (2.1)$$

The surface tension forces act to keep a drop in its hemispheric shape, where the least formation energy is needed. These forces act along the edge of the hemispherical film in a circular manner. The magnitude of the force resulting from each surface of the hemispherical film is the product of the surface tension σ and the sphere's circumference ($2\pi R = \pi D$).

A liquid drop disintegrates once the aerodynamic drag is just equal or greater than the surface tension force, i.e. [2010, Lefebvre *et al.*]:

$$\sigma D \pi = \frac{1}{2} c_D \rho_{air} v_{rel}^2 \left(\frac{\pi}{4} \right) D^2 \quad (2.2)$$

Refurbishing the equation above results in the following dimensionless set of parameters:

$$\left(\frac{\rho_{air} v_{rel}^2 D}{\sigma} \right)_{crit} = 8/c_D \quad (2.3)$$

where subscript "crit" refers to a reached critical condition.

Weber number

$$We = \frac{\text{fluid's inertia}}{\text{fluid's surface tension}} = \frac{\rho_{air} v_{rel}^2 D}{\sigma} \quad (2.4)$$

[2010, Lefebvre *et al.*] report that for low-viscosity fuels, with an experimentally obtained c_D the term $8/c_D$ can be rounded to 12, i.e.,

$$We_{crit} = 12 \quad (2.5)$$

Consequently, the maximum stable drop size is attainable from equation (2.3)

Maximum stable drop size

$$D_{max} = \frac{12\sigma}{\rho_{air}v_{rel}^2} \quad (2.6)$$

The maximum drop diameter is of great importance as it enables us to calculate some of the spray characteristics such as spray evaporation time [2010, Lefebvre *et al.*].

Early experiments on the effect of the viscosity, fluid density, surface tension as well as orifice diameter on the breakup of the liquid jets were carried by Ohnesorge 1936; he correlated the atomization specific parameters into a dimensionless group [2006, Joos]. This dimensionless group is known as Ohnesorge number.

Ohnesorge number:

$$Oh = \frac{\sqrt{We}}{Re} \quad (2.7)$$

Reynolds number:

$$Re = \frac{\rho_{liquid} v_{rel}^2 D}{\eta_{liquid}} \quad (2.8)$$

η_{liquid} = dynamic viscosity, (Pa s)

Characteristic Mean Drop Diameter

The mean drop diameter represents a unified way of averagely describing how fine or coarse an atomization process is, i.e. average drop diameter. Mean drop sizes help to better compare nozzles in the same class. Some of representative diameters include the following [2008, Schick].

$D_{0.1}$: The value indicates drop diameter such that 10% of total atomized liquid volume consists of smaller diameters.

$D_{0.32}$: The value indicates drop diameter such that 32% of total atomized liquid volume consists of smaller diameters. This diameter is especially useful for

calculating the efficiency and mass transfer rates in chemical reactions. This value is generally known as Sauter Mean Diameter which is the most important mean diameter in combustion applications [2010, Lefebvre *et al.*].

$D_{0.5}$: The value indicates drop diameter such that 50% of total atomized liquid volume consists of smaller diameters. This value is generally known as (Volume) or Mass Mean Diameter VMD or MMD.

$D_{0.9}$: The value indicates drop diameter such that 90% of total atomized liquid volume consists of smaller diameters. This measurement is used when complete evaporation of the spray is needed [2008, Schick].

Flow Number

An additional way of describing pressure atomizers is their effective flow area as a flow number. This designates the ratio of the nozzle mass flow to the square root of the fuel injection-pressure differential. For a reliable reading of flow numbers the following formula is commonly used [2010, Lefebvre *et al.*]:

$$FN_{SI} = \frac{\text{Flow rate, kg/s}}{(\text{Pressure differential, Pa})^{0.5} (\text{Liquid density, kg/m}^3)^{0.5}} \quad (2.9)$$

A factor on the evaporation time of the fuel drops is the spray cone angle for a given burner geometry. This particularly influences the desired drop-size distribution of a sprayer. It is recognized that by increasing the cone angle, the exposure area of the spray with the surrounding air is increased that results in faster evaporation and a more efficient combustion. This is valid only when spray drops spread unhindered and do not collide with the burner wall. The premixture plenum used in this work is a cylindrical tube with 40 mm in diameter and 160 mm in length, which is relatively narrow for a spray angle of 45° not to collide with its walls.

The cone angle is measured by drawing two straight lines extending from the opening of the atomizer orifice alongside with the spray contours to a specified distance [2010, Lefebvre *et al.*].

$$\text{Cone Angle (hollow)} \quad \cos^2 \theta = \frac{1 - X}{1 + X} \quad (2.10)$$

$$X = \frac{\text{Air core area}}{\text{Discharge orifice area}} = \frac{A_a}{A_o} \quad (2.11)$$

where:

$$\frac{A_a}{A_o} = \frac{(D_o - 2t)^2}{D_o^2} \quad (2.12)$$

θ = cone half-angle, ($^\circ$)
 A_a = air core area, (m^2)
 A_o = discharge orifice area, (m^2)
 t = film thickness, (m)
 D_o = discharge orifice diameter, (m)

Film Thickness

where:

$$t = \frac{0.00805 \sqrt{\rho_L} FN}{D_o \cos \theta} \quad (2.13)$$

ρ_L = Liquid density, (kg/m^3)
FN = Flow number, (m^2)

Sometimes the spray cone non-uniformity causes combustion instabilities and higher NO_x , CO and UHC emission levels, this is due to hot and relative cold spots existing in the combustion chamber [2004, Phillips *et al.*].

When selecting an atomizer for a specific application, the designer should be aware of a few factors such as: fuel type, type of atomizer, injection pressure, required flame length, and atomization process energy consumption. In addition, environmental conditions that affect the nozzle must be taken into consideration [2002, Nasr *et al.*].

2.2 Fundamentals of Combustion Technology

A chemically reacting flow that grows rapidly and is highly exothermic is called combustion. Its interdisciplinary nature comprises with thermodynamics, chemical kinetics, fluid dynamics, and transport phenomena [2006, Law].

Thermodynamics

In a combustion process, heat is released due to conversion of chemical into thermal energy. Reactants are converted into products by a chain of exothermic reactions. The released heat can be utilized for various purposes. Calculation of the heat produced in such reactions along with their equilibrium energy is achieved in thermodynamics.

Chemical Kinetics

Thermodynamics links the initial and final combustion state, whereas chemical kinetics account for the path and how long such a reaction lasts.

Fluid Mechanics

A key to understanding many combustion phenomena is to study fluid mechanics. Pressure and temperature drops and rises that occur during combustion inside a combustion chamber can have significant effects on the reacting fuel and oxidizer.

Transport Phenomena

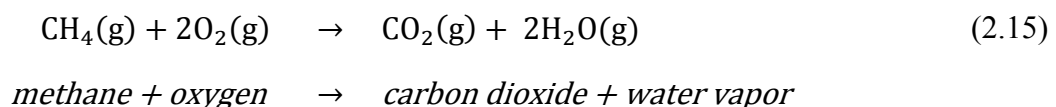
In a combustion process, chemical reactions rapidly happen in highly localized regions of a flame. In lower temperature regions where lower concentrations of product dominate the field, higher concentrations of reactant can be found. In the global level, as a result of having temperature and concentration gradients, energy travels from a high temperature region to a lower one in form of heat.

For simple reaction calculations, the molar concentration of the air can be defined as 21 percent oxygen and 79 percent nitrogen. The minimal concentration of Argon in air can be neglected for practical uses. This means that for every mole of oxygen there are 3.76 moles of nitrogen in 4.76 moles of air.

$$\text{Air} = 0.21\text{O}_2 + 0.79\text{N}_2 \quad (2.14)$$

Thermal energy of combustion is reduced due to nature of nitrogen as an inert gas, i.e. an amount of energy is used to heat it up during the burning process. If an application requires so, an oxygen-rich air or even pure oxygen can be used for yielding higher combustion temperatures.

The amount of heat released during a combustion process depends on the relative concentrations of fuel and oxidizer. Adjusting their chemical concentration in a way that a correct balance is achieved yields the conversion of all the reactants (fuel + oxidizer) into products. Thus, a maximum thermal energy is released that is known as stoichiometric combustion. A way of demonstrating this state is to burn methane (CH_4) with oxygen (O_2).



s shown in the above reaction, the sole products are water and carbon dioxide and there are neither excess fuel (methane) nor excess oxidizer (oxygen) coming out of the reaction. This state is known as stoichiometrically balanced reaction.

A fuel-oxidizer ratio, F/O , can be defined to quantify the relative concentration to fuel and oxidizer in a mixture. This ratio simply defines the mass of fuel to the mass of oxidizer in a reaction. Identically a fuel-air ratio, F/A , is defined for reactions that involve air as the primary oxidizer. In order to tell alternation of a premixture from its stoichiometry state, an equivalence ratio Φ or its reciprocal value $\lambda = \frac{1}{\Phi}$ is used that is defined as

Equivalence Ratio, Φ

$$\Phi = \frac{1}{\lambda} = \frac{(F/O)}{(F/O)_{st}} \quad (2.16)$$

Fuel-Oxidizer Ratio, F/O

$$F/O = \frac{\text{mass of fuel}}{\text{mass of oxidizer}} \quad (2.17)$$

where index “st” indicates the stoichiometric state. This way, $\lambda < 1$, $\lambda = 1$, and $\lambda > 1$, respectively, designate fuel-rich, stoichiometric, and fuel-lean combustion. In this work air-to-fuel equivalence ratio λ will be used to correspond to the combustion operating points’ drift from stoichiometric state.

2.3 Basics of Low-Emission Combustion

Comparing the emissions released by a typical ICE in the 1950s to the modern low emission ICEs can give an insight on the improvements achieved in the combustion technology. A major concern of our society is pollution and health. Identifying most important pollutants and their sources can lead to solutions for their reduction. Pollutants like soot, nitric oxide (NO_x), unburned hydrocarbons (UHC), and carbon monoxide (CO) build the list for the most unwanted pollutants [2006, Law]. Carbon dioxide (CO_2) and water vapor (H_2O) are not regarded as pollutants as they are the natural product of complete combustion of hydrocarbon fuels. Nevertheless, they do contribute to global warming and the only way to reduce them is to burn less fuel or use of non-hydrocarbon fuels. Improving thermal efficiency of an engine

and thus reducing pollutants is directly coupled with minimizing direct operation costs [2010, Lefebvre *et al.*].

To further discuss the mechanisms of pollutant formation, a brief overview of how principal pollutants are created is described below:

NO_x

NO_x is the sum of nitric oxide (NO) and nitric dioxide (NO₂) and is formed during combustion either from N₂ in the atmosphere or the nitrogen within the fuel. The NO_x that originates from the atmospheric nitrogen is produced under high temperature oxidation and is known as thermal NO_x. The formation of the fuel bounded NO_x is highly dependent on sort of fuel use in the combustion and is known as fuel nitric oxide. A further mechanism leading to nitric oxide formation depends on the reaction of N₂ with fuel radicals at fuel rich combustion conditions that is known as prompt NO.

NO_x emissions from combustion are primarily in the form of NO. According to the Zeldovich equations, NO emissions are produced at temperatures above 1300°C [2010, Lefebvre *et al.*]. Generation of thermal NO is dependent on the F/O, and is accelerated when the mixture is on the fuel-lean side of the stoichiometric ratio [1999, EPA-Report].

Definition of NO_x:



Zeldovich Equations:



Due to environmental considerations, many modern combustion technologies deploy NO_x prevention methods in order to reduce their NO_x emissions. A few technical provisions offer smart solutions on how to prevent or at least reduce NO_x generation.

Combustion temperatures have great influence on NO_x emissions. By simply avoiding the stoichiometric ratio and moving to the lean-fuel side of the mixture, a lower flame temperature can be realized. Technically, thermal energy is diluted as a result of excess air being present in the flame zone. Similarly, combustion temperature can be reduced by moving the F/O to fuel-rich side by limiting the amount of oxygen available. Injecting water or steam into the combustion chamber leads to temperature drop as well as partial prevention of nitrogen from

becoming ionized [2010, Lefebvre *et al.*]. Reducing residence time of the combustion gas in the high-temperature zones also contributes on lowering the NO_x emissions.

CO

As mentioned before, concentration levels of pollutant in exhaust emissions are related directly to the temperature, the fuel drop residence time, and the fuel used in the combustion process. On the one hand, formation of CO and UHC increases at lower thermal power operating points and they decrease by increasing engine power (see Figure 2.1). On the other hand, NO_x formation diminishes by decreasing engine power and increases in higher engine powers [2010, Lefebvre *et al.*]. For better understanding of these characteristics, a graph is depicted in Figure 2.1.

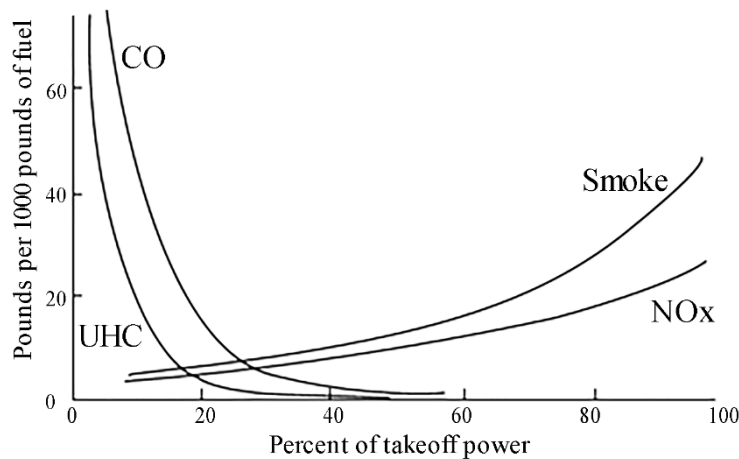


Figure 2.1 Emissions characteristics of gas turbine engines as a function of percent of takeoff power (100% = maximum fan rotation speed) and engine fuel consumption [2010, Lefebvre *et al.*]

In a fuel-rich combustion process the amount of CO rises as there is not sufficient oxygen to react with to form CO_2 . This is not always the case, as CO is formed during near stoichiometric or even light fuel-lean conditions due to dissociation of CO_2 into CO [2010, Lefebvre *et al.*].

Unburned Hydrocarbons (UHC)

Unburned hydrocarbons in the exhaust gas are formed due to incomplete combustion of the fuels caused by local flame quenching. During reaction process, different sizes of hydrocarbons can be formed from the fuel, which do not completely oxidize under local conditions. UHC

formation mechanism is greatly more complex than CO. However, it is commonly accepted that those influencing factor regarding CO emissions are interconnected with UHC emissions the same way [2006, Joos].

2.4 Previous Work

Some works regarding jet-stabilized liquid fuel combustors have been conducted at the Institute of Combustion Technology of the German Aerospace Center (DLR). In this section, an overview of the previous work on the combustor for C30 micro gas turbine range extender will be given to lead over the current work's motivation and goals. It is worth mentioning that the burner section, on which the current experiments were carried out, originates from the very first test bed that was used for initial researches of small scale single nozzle liquid FLOX[®] combustor.

First experiments conducted by [2015, Zizin *et al.*] based on “Development of a Jet-stabilized Low-emission Combustor for Liquid Fuels”. In their work, the ongoing development of a liquid fuel combustor in terms of investigation of flame stabilization of jet flames as well as fuel atomization, spray dispersion and evaporation were investigated. “An axisymmetric single nozzle combustion chamber was chosen for the initial setup. A variety of burner configurations was tested in order to investigate the influence of different design parameters on the flame shape, the flame stability, and emissions” [2015, Zizin *et al.*].

In addition, “a twelve-nozzle FLOX[®] burner with pre-evaporator was designed and characterized. The combustor was operated at atmospheric pressure with preheated air (300°C) and in a range of air equivalence ratios between $\lambda = 1.05 - 2$. The maximum thermal power was 40 kW” [2015, Zizin *et al.*]. In their experiments, [2015, Zizin *et al.*] varied the nozzle depth to investigate the vaporization effect on the flame (see Figure 2.2 left).

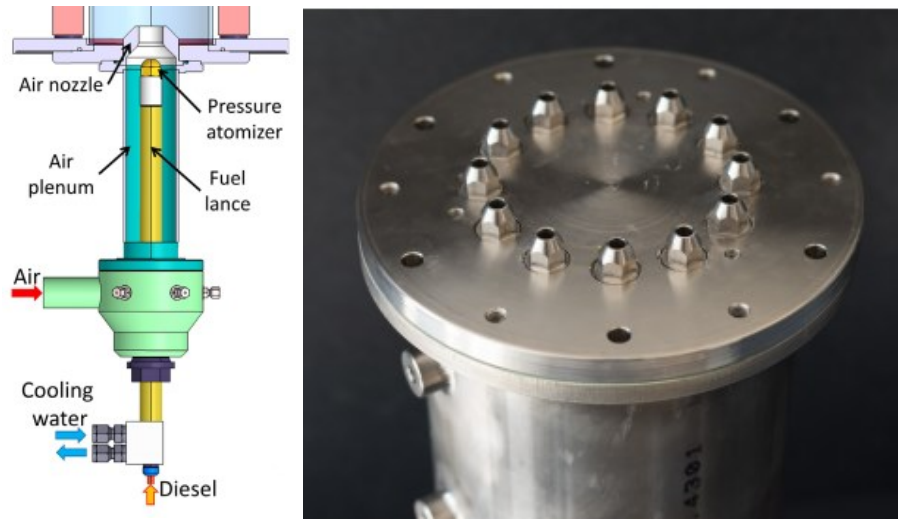


Figure 2.2 Zizin's burner with Ø20mm air nozzle (left), vaporizer with 12 - nozzle burner (right) [2015, Zizin *et al.*]

A further study was conducted by Gounder *et al.* concerning “Spray Characteristics Measured in a New FLOX[®] Based Low-emission Combustor for Liquid Fuels using Laser and Optical Diagnostics” [2016, Gounder *et al.*].

“A spray FLOX[®] burner was designed for testing at the High Pressure Optical Test rig (HIPOT), at DLR Stuttgart. The design of this burner was based on earlier work from [2015, Zizin *et al.*], which was carried out at atmospheric pressure. The main application of the burner was for operation at a thermal load (P_{th}) of 155 kW_{th} and the corresponding pressure of 3.5 bars, in order to meet the electric power output requirement of 48 kW_{el} from the micro gas turbine of a car range extender” [2016, Gounder *et al.*].

Their experiments were conducted in the following conditions:

Parameter	Value	Unit
Pressure	3.5	bar
Velocity	80 – 140	m/s
Air equivalence ratio λ	1.25 – 2.0	-
Air preheat temperature	300	°C
Thermal power	155	kW
Number of nozzles	8	-

Table 2.1 Combustion parameters of Gounder's experiments [2016, Gounder *et al.*]

After the first development steps of a FLOX[®] burner (Figure 2.3) for an MGT-REX application were conducted by [2015, Zizin *et al.*, 2016, Gounder *et al.*], [2017, Schäfer] further investigated the new twelve-nozzle FLOX[®]-based burner, which was designed to be integrated into Capstone C30 micro gas turbine. Primarily, he examined fuel injector nozzles and their effect on the performance of the FLOX[®] burner at 3.5 bars and 460°C. For these experiments, a two-nozzle liquid FLOX[®] burner was used. A variety of commercially available pressure fuel nozzles were analyzed at the high pressure test rig HIPOT. In order to characterize the atomization behavior of the fuel nozzles, a variety of non-reactive experiments were also conducted at atmospheric pressure. In addition, spray shape and angle of each fuel nozzle were measured.

Schäfer's findings showed that commercially available pressure atomizers that were used in the burner suffered from significant deterioration of performance regarding the atomization process at the high preheat temperature of 460°C. A major issue detected while experimenting with nozzles was nozzle blockage that led to instable operation of the burner. In his work, flame lengths ranged from 40 – 80 mm. [2017, Schäfer] claims that the droplet size played a major role in defining the flame length. The reported exhaust gas emissions range from NO_x and CO below 3 and 5 ppm, respectively.

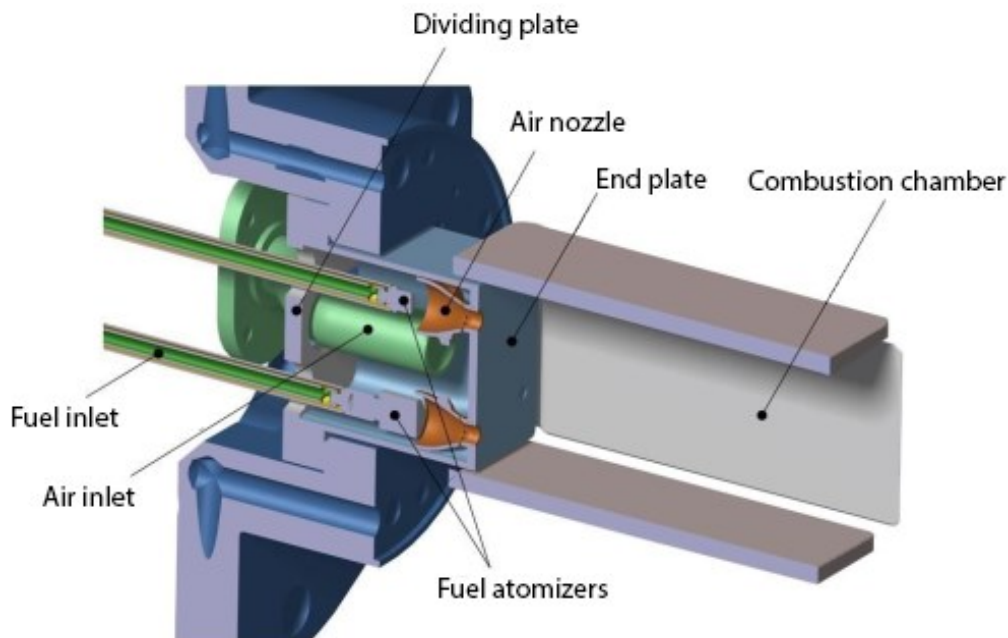


Figure 2.3 Setup of Schäfer's two-nozzle FLOX[®] burner [2017, Schäfer]

3 EXPERIMENTAL SETUP

3.1 Single Nozzle Burner for Range Extender

In the original configuration, the combustion chamber of the C30 Capstone micro gas turbine operates with three air blast atomizers, which tangentially inject fuel into its combustor. In an effort to make the C30 MGT a viable range extender for electric vehicles, the department of Micro Gas Turbines of the Institute of Combustion Technology DLR Stuttgart plans to replace the original recuperator, the burners, the combustion chamber, and the atomizers with more efficient components. Retaining the original three nozzle configuration helps increasing operability of individual nozzles and decreases modification of the original C30 MGT. In addition, utilizing the three-nozzle configuration prevents coking effects that occurred during the 12-nozzle configuration used by [2017, Schäfer]. It is worth mentioning that the 12-nozzle concept was dropped and replaced with the 3-nozzle configuration that allowed for higher fuel mass flow per single nozzle, which in return translates into larger nozzle exit orifice than the previous configuration. Except for the crossflow of the exhaust gases and the air pressure in the original C30 combustion chamber, all other features such as a) air preheat temperature, b) thermal power, and c) air nozzle diameter are realized in the present work's single nozzle burner.

A single nozzle burner with a nominal thermal power of 38 kW, at 100 m/s air nozzle exit velocity, and air preheat temperature of 460°C was used to study the atomization behavior of a series of off-the-shelf oil spray nozzles. One or few nozzles are then to be used and further investigated in the Capstone C30 micro gas turbine. Most of the original operating conditions of the Capstone C30 MGT were taken into consideration to provide as transferable results as possible.

In this chapter, a detailed overview of the experimental setup and the combustion parameters used in this work will be described. In order to replicate the existing thermal and the intended geometrical conditions of the Capstone C30 MGT combustion chamber with the new liquid

fuel burner. In this regard, a preheat temperature of 460°C was realized to mimic the CC inlet temperature and an air nozzle with $\varnothing 25.2$ mm outlet diameter was used to realize an air mass flow of 100 m/s air nozzle exit velocity. The fuel mass flow was adjusted accordingly to cover a thermal power range of 9 – 50 kW.

As shown in Figure 3.1, pressurized air entered a mass flow controller (MFC) of the manufacturer *Brooks* prior to entering an in-house built 15 kW air preheater. The 460°C preheated air flowed the single nozzle burner with a mass flow range of 18.6 – 28 g/s. The varying air mass flow enabled the variation of the flow velocity of 80 – 120 m/s for the previously mentioned air mass flows, respectively. Air and fuel were then premixed before reaching the plenum's exit, here designated as air nozzle.

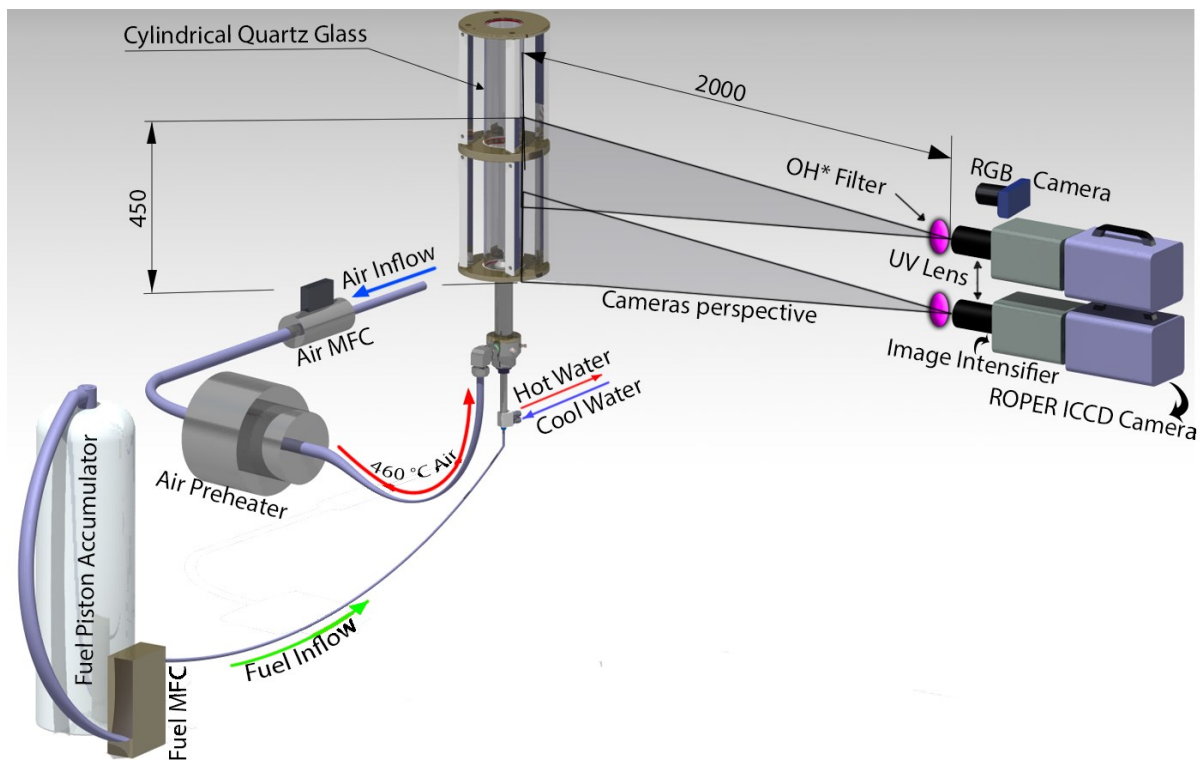


Figure 3.1 Single nozzle burner along with other equipment used during the experiments

The liquid fuel was supplied to the mass flow controller using a piston accumulator, which was driven by pressurized nitrogen gas. In order to regulate the inflow of the fuel, a liquid MFC of the manufacturer *Bronkhorst* was utilized to remotely monitor, control, and document the fuel mass flow. As further explained in section 3.3 Premixture Plenum, a water-cooled fuel lance received the fuel and consequently fed it to the fuel nozzle. To prevent abrupt vaporization and chemical decomposition of the fuel inside the lance, and to cool the fuel nozzle preventing it

from fuel deposition and thus blockage, the lance was cooled by constantly flowing water through its body. After the fuel droplets and air were mixed within the plenum, an air nozzle with a contracting area connected the plenum with the combustion chamber where the premixed fuel and hot air were manually ignited using a hydrogen torch.

For measuring the flame properties such as chemical reactions within the flame, flame height (FH), and flame lift off height (LOH), two intensified charge-coupled device (ICCD) cameras (resolution 512x512) were used to detect the chemiluminescence of hydroxyl radicals (OH^*) inside the flame zone. In addition, a conventional red-green-blue (RGB) camera was used to capture the visible emission of the flame. These cameras were placed perpendicular to the burner vertical axis at a distance of two meters. Separate computers captured the output of the ICCD cameras simultaneously during each operating point. The data were then recorded and post-processed using *DaVis 8.3.1* of the company *LaVision* (see section 5.3.1).

A total of six fuel nozzles (see sections 3.6 & 5.1) of different spray angles and capacities were taken into consideration to examine their atomization behavior under the previously mentioned thermal and geometrical conditions. Their nominal spray angles were 30° and 45° , with capacities of 0.35 (~ 0.362 g/s) and 1 US gallon per hour (~ 1.033 g/s), and spray cone shapes of hollow (H) and solid (S).

3.2 Combustion Chamber

The initial configuration of the combustor originated from previously conducted studies on atomization process by [2015, Zizin *et al.*]. As shown in Figure 3.2, the single nozzle burner consisted of two main sections. The upper cylindrical section was designed as a two-part combustion chamber of 300 mm length each and a diameter of \varnothing 95 mm.

The usage of quartz glass as the wall of the combustion chamber offered optical access to the flame as well as to unevaporated spray drops. Two tubular quartz glasses were connected with four flanges and an aluminum frame (see Figure 3.2). To prevent the structure from deformation or any other thermal hazards, a water cooling system was included in the frame. Multiple air blowers were mounted near the optical combustion chamber walls to direct ambient air toward its wall. The exhaust gas was directed through a duct installed above the combustion chamber and an exhaust gas extractor fan.

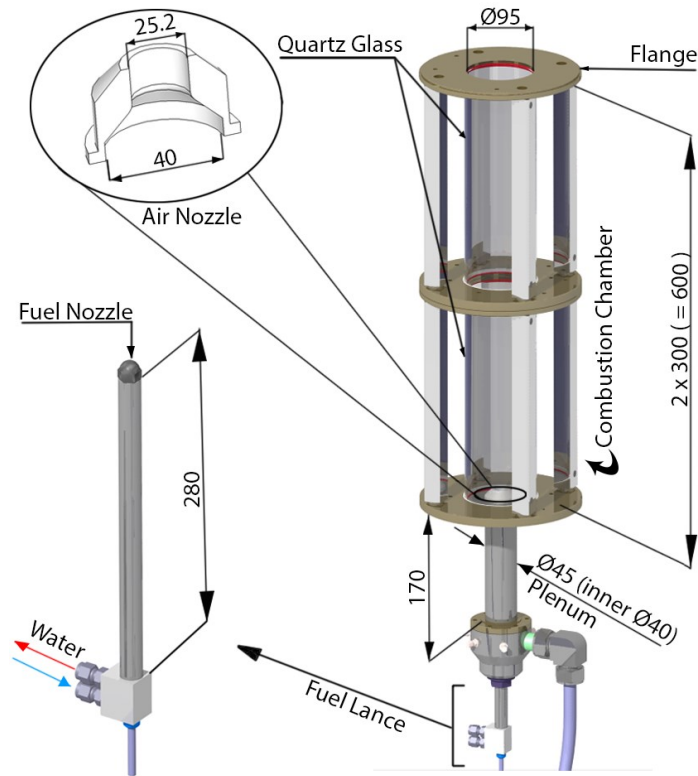


Figure 3.2 Detailed dimensions of the combustor along with the fuel lance and the air nozzle

3.3 Premixture Plenum

The lower section of the combustor, termed as premixture plenum, was arranged in a way that an exchangeable fuel lance (6 in Figure 3.3) could be mounted in a variable distance to the air nozzle exit. The cylindrically shaped plenum had an inner diameter of Ø 40 mm and a length of 160 mm (13 in Figure 3.3).

In order to preserve the heat provided by the air preheaters, the plenum wall was insulated. On the inflow of the plenum, a perforated plate (7 in Figure 3.3) was fitted that was used to direct the perpendicularly entering air towards the air nozzle. For redundantly reading the actual temperature inside the plenum, two k-type thermocouples (8 in Figure 3.3) were mounted on two spots of the plenum's mounting part. This was used as the nominal plenum temperature neglecting any temperature loss downstream the flow.

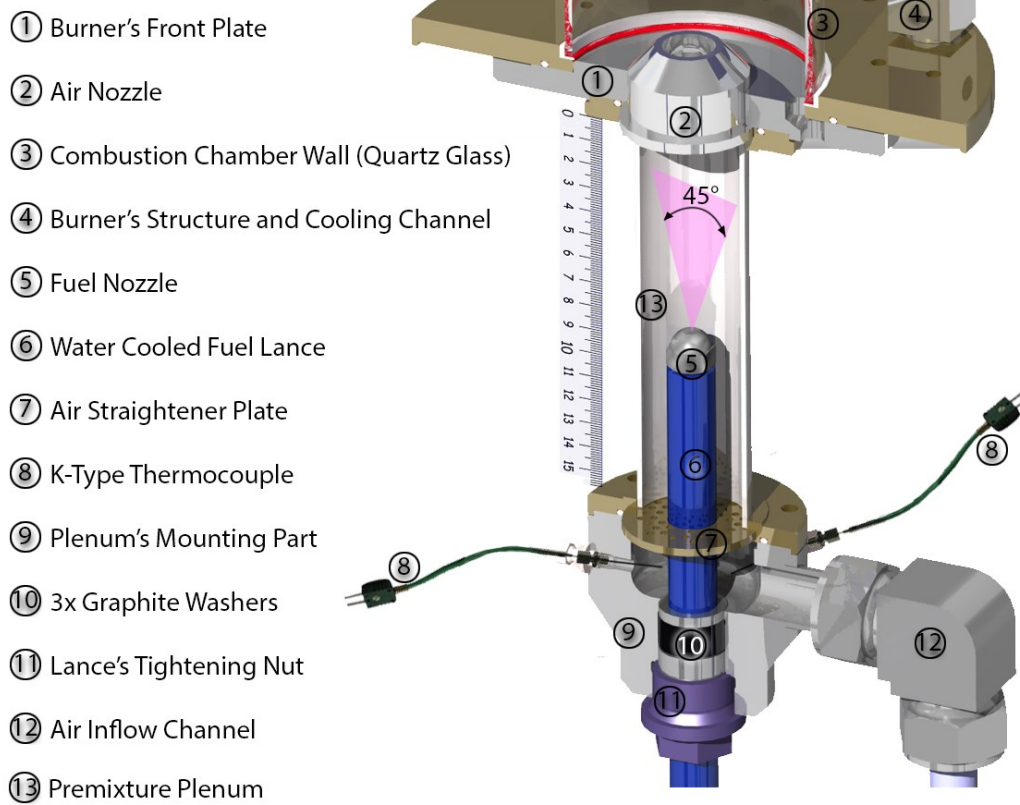


Figure 3.3 Cross-section of burner's premixture plenum

3.4 Fuel Lance

The water-cooled fuel lance (see Figure 3.2) was configured with two inlets and an outlet on its lower end. The length of the lance measured 280 mm. Due to different fuel nozzles used in this work, a series of fuel nozzle adapters were constructed as a thread connecting-piece between the lance and nozzles. The lance itself had a 9/16-24 UNEF female thread.

For an easy (un)tightening of the lance and the plenum mounting part, three graphite washers (10 in Figure 3.3) were used to air seal the parts (compression gland). Varying the distance of the fuel nozzle from the air nozzle exit was expected to have an influence on the evaporation of the spray drops.

Fuel Lance Depth Variation

To further investigate this phenomenon, the lance depth was varied throughout the experiments. The lengths of the plenum and the fuel lance measured 160 and 280 mm,

respectively. This allowed for a full utilization of the available space between both ends of the plenum (see Figure 3.4).

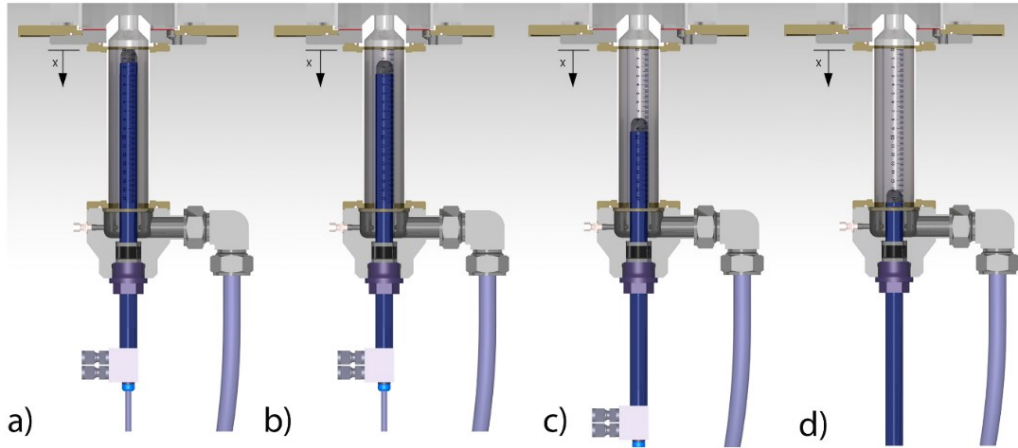


Figure 3.4 Demonstration of fuel lance depth variation, a) 0 cm, b) 1 cm, c) 8 cm, and d) 16 cm

3.5 Air Nozzles

Overall, two air nozzles with exit diameters of $\varnothing 25.2$ and $\varnothing 12.5$ mm were constructed to serve as the connecting piece between the plenum and the combustion chamber. This way, the air mass flow could be varied by keeping the air exit velocity constant. For the majority of the experiments, the larger air nozzle was used as it matched with the exit diameter of the Capstone C30 MGT burner.

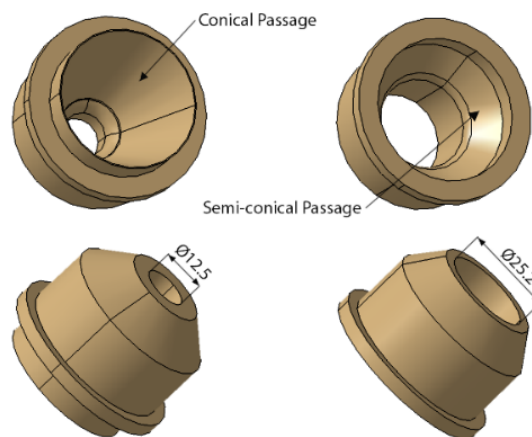


Figure 3.5 Overview of air nozzles; left) conical , right) semi-conical

The cone length of the air nozzle shown in Figure 3.5 (left) measured 18 mm with an angle of 20° , whereas the semi-conical air nozzle measured 30 mm and 45° in length and angle, respectively.

3.6 Fuel Nozzles

The major objective of the current study was to examine the atomization behavior of a set of fuel nozzles, which varied in spray cone shape, flow capacity, spray angle, and were produced by different manufacturers. Table 3.1 shows a list of the examined fuel nozzles. The flow capacity of 1.033 g/s was specifically chosen as it approximately equates to a third of nominal thermal power of C30 micro gas turbine (see section 3.1). Figure 3.6 exhibits an overview of fuel nozzles of diverse manufacturers: Steinen, Danfoss, and DIVA. Fuel nozzles of Steinen and Danfoss were directly mounted to the fuel lance, since they both had 9/16-24 UNEF male thread. However, a lance adapter had to be constructed to fit DIVA's thread of 1/8 BSPT to 9/16-24 UNEF. Steinen and Danfoss were equipped with a brass sintered filter, whereas DIVA was not delivered with a filter. Listed labels in given Table 3.1 will be used throughout the chapter 5 Data Evaluation and Results. An overview of the used pressure atomizer in given in Figure 3.6.

Nozzle	1	2	3	4	5	6
Spray angle ($^\circ$)	45	45	80	60	30	45
Spray cone shape	Hollow	Solid	Hollow	Hollow	Solid	Hollow
Capacity (GPH)	1	1	0.713	0.35	1	1
Capacity (g/s)	1.033**	1.033**	0.667***	0.361*	1.033*	1.033*
Material	Brass	Brass	Stainless Steel	Stainless Steel	Stainless Steel	Stainless Steel
Manufacturer	Danfoss	Danfoss	DIVA	Steinen	Steinen	Steinen
Lable	Dan45°H	Dan45°S	DIVA	St60°H	St30°S	St45°H

Table 3.1 Summary of the fuel nozzle examined within the scope of this work - * at 10 bars - ** at 10 bars, kin. viscosity $\nu = 3.4 \text{ mm}^2/\text{s}$, density $\rho = 840 \text{ kg/m}^3$ - *** at 3 bars



Figure 3.6 Examined fuel nozzles; a) Danfoss oil nozzle [2014, Danfoss], b) Steinen oil nozzle [2016, Steinen], c) DIVA

3.7 Experimental Infrastructure

Air Mass Flow Controller

A *Brooks model 5853S Flow Controller* was used as a mass flow measurement and control device. The manufacturer claims an accuracy of 0.7 % of the measured value. As a validation, a highly precise Coriolis (Siemens) flow rate meter was deployed to validate MFC's reading and controlling. A remarkable feature of the Brooks MFC lied in its relatively quick flow rate control.

A WMR 4008 device was used to connect the air MFC with the controlling computer. Due to the unavailability of an air MFC for the needed range of 1400 liters per minute (l/min), a CO₂ rated MFC with a range of 1200 l/min was utilized instead for the experiments. According to the user manual of Brooks, a factor was integrated into the control software to correct the measured value.

Fuel Mass Flow Controller

For accurately measuring the fuel flow and correspondingly regulating it, a *Bronkhorst CORI-FLOW* liquid flow controller was used. As described by Gaspard-Gustave Coriolis in 1835, moving objects deflect from a straight path when they are viewed from a rotating frame of reference [CORI-FLOW-Data-Sheet]. Once a fluid flows in a vibrating pipe, Coriolis forces cause a change in frequency, phase or amplitude alteration proportionally to the mass flow rate inside the pipe (see Figure 3.7) [CORI-FLOW-Data-Sheet]. This is then detected by pickup sensors and forwarded to the computer by a RS-232 interface (see Figure 3.8)

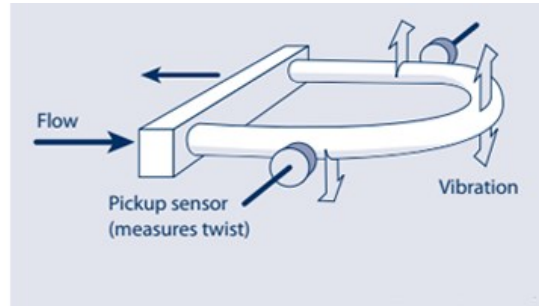


Figure 3.7 Schematics of Coriolis flow sensor [CORI-FLOW-Data-Sheet]

For this work, a mini CORI-FLOW™ type M14 with maximum flow rate of 1.388 g/s (see Figure 3.8) was used to accurately measure and control the oil flow. Fluid density and temperature were additionally obtained from the CORI-FLOW™. Two pressure measurement points were set prior to and after the fuel controller. This was particularly useful for regulating the fuel pressure prior to the fuel nozzles and after the piston accumulator.

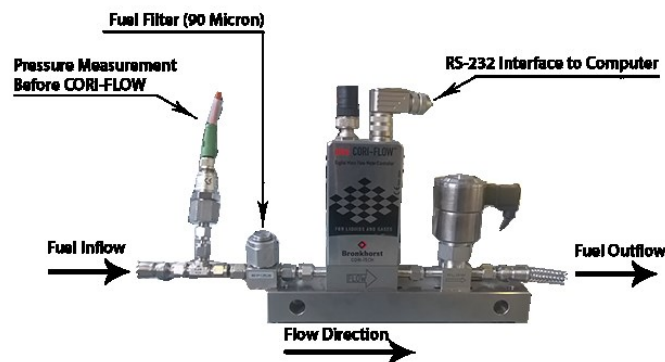


Figure 3.8 Overview mini CORI-FLOW™ along with its components

Temperature Measurement

K-type thermocouples with an accuracy of $\pm 2.2\text{ }^{\circ}\text{C}$ or $\pm 0.75\%$ (whichever is greater) were used for temperature measurements of the air and the fuel. By using an ICP CON Thermocouple 8-Channel Analog Input Module, readings were sent to the computer for documentation and monitoring.

Fuel Pressure Measurement

As mentioned before, in order to monitor the behavior of the fuel nozzle in a variety of operating points, i.e. different flow rates, two pressure transducers manufactured by *Gems* were

installed on the test rig. The pressure transducer's full scale accuracy was 0.25 % and showed a long term stability of less than 0.2 %.

Software

The fuel as well as air flow rates, pressure and temperature readings were monitored, regulated and subsequently documented in a LabVIEW interface software. Within the scope of this work, an in-house existing virtual instrument (VI) Figure 3.9 was developed to suit the current work's setup.

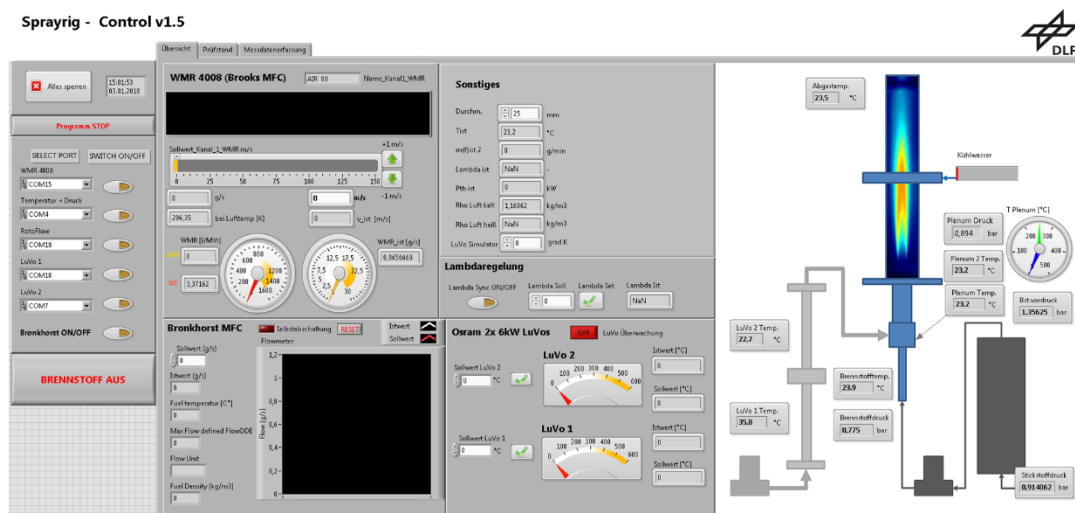


Figure 3.9 Screenshot of the developed VI used for controlling the MFCs and monitoring pressures and temperatures

4 MEASUREMENT TOOLS

4.1 OH* Chemiluminescence

The use of diagnostic methods for monitoring and analyzing flames enables a better understanding of the combustion mechanisms. During chemical reactions, flames naturally emit ultraviolet and visible radiation called chemiluminescence. This phenomenon is caused by short lived electronically excited intermediate species that will be discussed in this chapter. By observing a flame with a spectrometer, a wide spectrum of electromagnetic radiation can be seen that is coupled to the flame's combustion parameters such as, temperature, pressure, air equivalence ratio, and degree of turbulence [2009, Geddis].

The flame diagnostic procedure is primarily based on emission bands that cover the ultraviolet-blue wavelength range (250 – 500 nm), which comprise emission intensities of the hydroxyl radical (OH*) (308 nm), the methylidyne radical (CH*) (430 nm), the diatomic carbon radical (C₂*) (513 nm) and the broadband emitting carbon dioxide radical (CO₂*) (300 – 600 nm) [2017, Ding *et al.*]. Thereby, flame images can be used as a signature of a particular combustion state [2007, Ballester *et al.*].

Two main reactions create chemiluminescence [2010, Ballester *et al.*]:

- (1) The formation of an excited radical (R) from two parent species (A and B)



- (2) Spontaneous loss of its excess energy to reach its ground state by the emission of one photon



The M in Eq. (4.1) is merely a reacting partner and remains neutral; its main job is to act as a collision partner with R*. The deactivation reaction of R* is principally caused by its collisional quenching with M, where a transition from a higher to ground state occurs. Its energy difference is absorbed or emitted as electromagnetic radiation [2014, Stamatoglou]. Equation (4.2) describes this energy as Planck constant h (J s) multiplied by the frequency of the emitted

emission ν , which is defined as speed of light c (m/s) divided by the wavelength λ (m) [2014, Stamatoglou].

The electromagnetic radiation wavelength depends on the molecule R (referred to as: OH, CH, C₂, CO₂) and its particular transition [2010, Ballester *et al.*]. Table 4.1 details the generally accepted formation reactions of OH* and CH*.

Radical	Reaction	Wavelength (nm)
OH*	R1: CH + O ₂ → CO + OH*	282.9, 308.9
CH*	R2: C ₂ H + O ₂ → CO ₂ + CH*	430
	R3: C ₂ H + O → CO + CH*	

Table 4.1 Formation reactions of the excited hydroxyl radical (OH*) and the methylidyne radical (CH*) and their characteristic wavelengths [2010, Ballester *et al.*]

The present work concentrates on analyzing OH* chemiluminescent radiation, as it is the most interesting radical for flame diagnostics. Ultraviolet radiation is emitted after formation of OH* as described in reaction R1. Influencing combustion parameters such as temperature, pressure, and air equivalence ratio affect the radiation emission levels of a flame, therefore, it becomes a useful diagnostic tool for the flame properties. The length and the other structural properties of the flame as well as its heat release zones can be extracted from the emission intensity of the chemiluminescent light.

In order to capture the spontaneously emitted photons of OH*, two detectors were placed on top of each other. Two identical 105 mm UV lenses (NIKKOR, f/4.5) plus UV interference filters ($\lambda = 312 \pm 20$ nm) were installed on both image intensifiers in order to achieve a high image resolution and filtering for OH* radiation. For both cameras (Roper ICCD), a 2.18 pixel / mm resolution was realized, which is sufficient for OH*-CL measurements. The OH*-CL emissions were detected with a gate time of 350 μ s. The data were recorded in batch of 200 registers per operating point. The gain of both image intensifiers was set to 200 (from a range of 0 – 255).

As shown in Figure 4.1 a), the covered area per camera is identical for both of the cameras. A 20×230 mm² overlapping area was realized to determine a match of the intensity scales of both cameras. Later post processing of OH*-CL images showed that due to the cameras' different

life cycles, different intensities were observed in the same spot in the overlapped area. This anomaly was corrected by using a technique that will be discussed in the chapter Data Evaluation and Results, section 5.3.1.

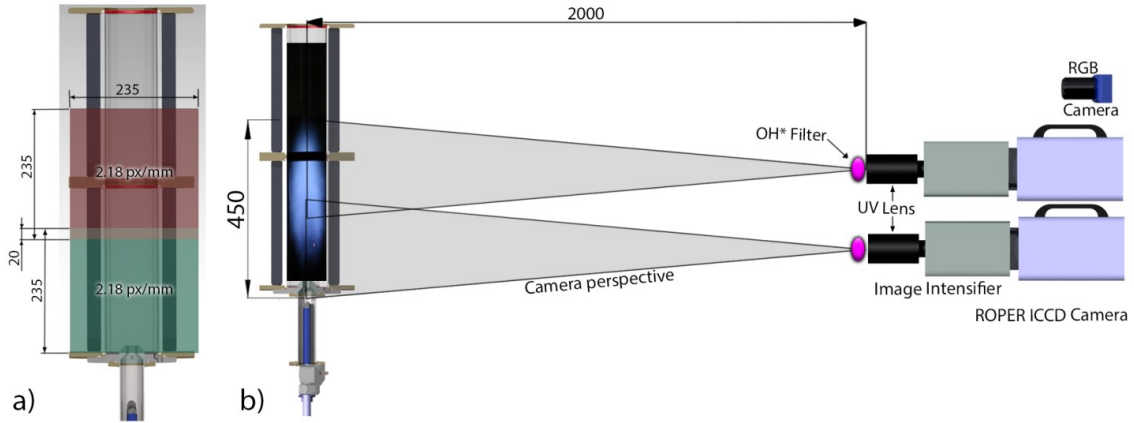


Figure 4.1 a) View areas of the Roper ICCD cameras on the burners cross section; b) sketch of the OH*- chemiluminescence imaging setup

4.2 Conventional RGB Camera

To further investigate the flame structural properties and its heat release zones, a conventional RGB camera was used as an additional visualizing diagnostic method to capture, for instance, the soot within the flame. Similar to OH*-CL imagery taken by the intensified CCD cameras, a Canon 70D was used to capture the CH* and broadband CO₂* light emitted in the flame reaction zone. CH* chemiluminescence can also be used to measure the heat release in the flame [2010, Guyot *et al.*].

For capturing not an instantaneous shape of the flame in fast speed, a shutter speed of 1/80 was chosen to average the flame structure as was done with OH*-CL post-processing recording. The aperture setting was set to a high f-stop number (f/5.6) to enlarge the images' depth of focus. This allowed for achieving a uniform sharpness throughout the flame length. Additionally, 3200 ISO was chosen as camera's sensitivity to the incoming light. As a result, an acceptable image noise level and brightness was achieved.

4.3 Mie Scattering

Generally, deviation of electromagnetic radiation from a straight trajectory by one or more paths is known as scattering. When a light photon traveling along the path of its wave passes through an irregularity, the light photon is scattered. This irregularity can be any object that is of different density. In the present work, the medium in which light photons travel through is air and irregularities are the fuel drops.

Two type of scattering can be distinguished: elastic and inelastic scattering. Light photon scattered by an irregularity that results in no (or very little) loss of photons radiation energy is known as elastic scattering. Inelastic scattering, however, involves some change to the photon's energy.

Scattering is dependent on the wavelength and is determined by the ratio of circumference of the spherical particle to the incident light wavelength. Rayleigh scattering is known for particle diameters that are much less than the light wavelength, whereas Mie scattering is known for larger or similar particle diameters than the light wavelength. Since the photon's radiation energy, frequency, and wavelength are not substantially changed through both Mie and Rayleigh scattering, they are both considered to be elastic scattering [2008, Albregtsen].

The scattering particle has a non-dimensional size parameter and is usually expressed as x , see Equation (4.3). Based on the value of x , three domains can be defined:

- $x \ll 1$: Rayleigh scattering
- $x \approx 1$: Mie scattering
- $x \gg 1$: geometric scattering (particles much larger than the incident light wavelength)

where:

$$\begin{aligned} R &= \text{radius of spherical particle, (m)} \\ \lambda &= \text{light wavelength, (m)} \end{aligned} \quad x = \frac{2\pi R}{\lambda} \quad (4.3)$$

The dependency of the Mie scattering intensity on the scattering angle is demonstrated in Figure 4.2 as a graph as well as a figurative description. Once an incoming light passes through a transparent particle, the particle causes the light to scatter in different direction in different intensities. Particles of similar size or larger than the incoming light wavelength scatter light photons more intensively in forward direction relative to backward direction.

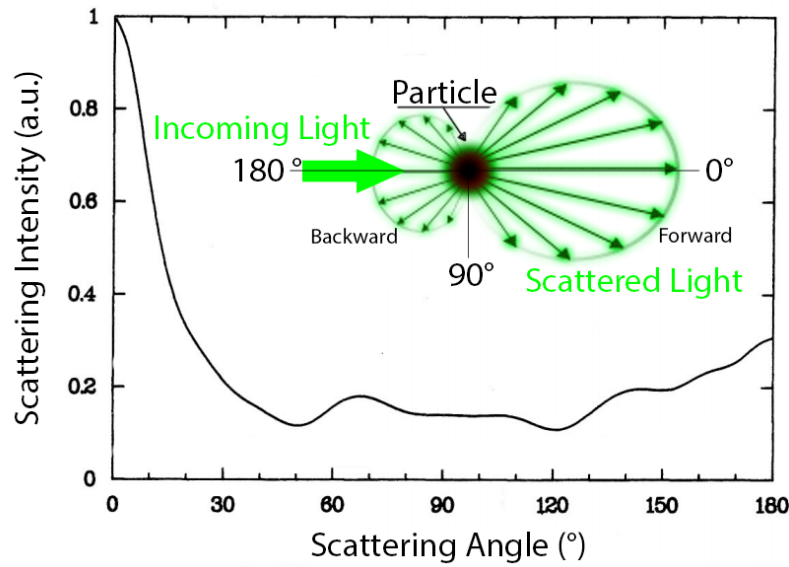


Figure 4.2 Mie scattering intensity (a.u.) as a function of scattering angle [1993, Singham *et al.*]: Mie scattering intensity highest at 0° scattering angle and decays by increasing scattering angle

In regard to studying the performance of the fuel nozzles and their effect on the flame behavior, experiments were conducted using Mie scattering to capture the distribution of fuel drops of various sizes close to the air nozzle on the burner head. Understanding the mechanisms involved in fuel drop evaporation when varying the fuel lance depth from the burner head can greatly help identifying the best performing pressure atomizer.

In the current work, while maintaining a stable flame, the effect of the air equivalence ratio ($\lambda = 1.5 - 2.2$) on the fuel drops exiting the Danfoss 45 ° hollow with the Ø 25.2 cm air nozzle at 100 m/s air velocity and 460°C air preheat temperature was examined. The covered fuel mass flows lied between 0.79 –1 .05 g/s. In addition, the fuel lance depth was set at 0 and 8 cm below the air nozzle to study the effect of longer residence time of the fuel drops in the burner on the drop evaporation.

The experimental setup of the Mie scattering measurement is depicted in Figure 4.3. An internally doubled Nd:YAG continuous wave laser type CPS532 with 4.5 mW power and 532 nm wavelength was used as light source to incite the Mie scattering of the fuel drops. The laser beam was expanded into a vertical sheet by means of a plano concave spherical lens with $f = -50$ mm set in series with a plano convex cylindrical lens with $f = 400$ mm. The sheet

passed centered over the air nozzle and measured 33 mm in width and 300 μm in thickness. A scattering angle of 33° was realized to detect greater Mie scattering intensities.

Detected signals were recorded by an ICCD camera type Roper Scientific PI-MAX operated at three different gate times: 350, 3500, 350000 μs for each operating condition to find an optimum point, where sufficient scattered light and a short exposure time were achievable. 300 instantaneous images (512×512 pixels resolution) were captured while the intensifier's gain was set at 200 (of a scale of 0 – 255). As depicted in Figure 4.3, perpendicular to the burner's axis, a 180 mm Nikkor ED lens was used on the ICCD camera along with a 532 nm bandpass filter to detect only scattered light photons emitted by the laser. The camera was installed 2 m apart from the burner.

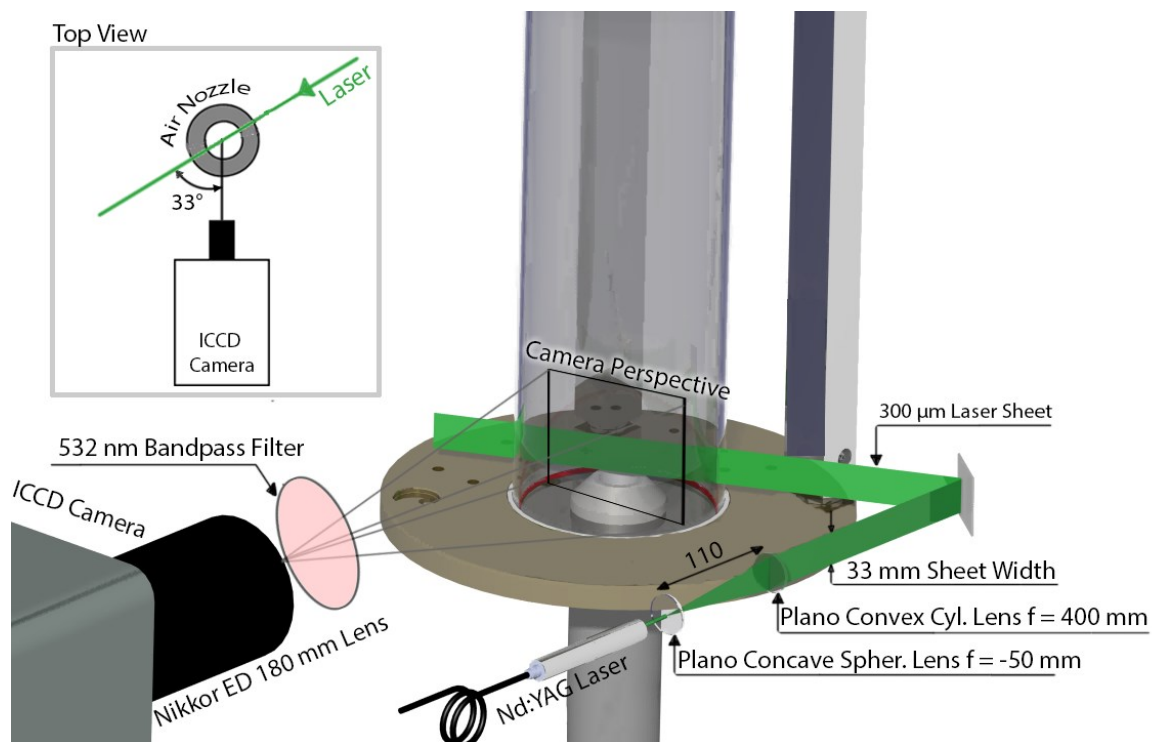


Figure 4.3 Setup of the Mie scattering experiment

5 DATA EVALUATION AND RESULTS

Experimental results of several fuel nozzles that could be operated at high preheat temperature of 460 °C and at the same time allowed operation of a stable flame are to be discussed in this chapter. A few hundreds of operating points were examined using the OH*-chemiluminescence technique; these were evaluated and assessed to find the best matching fuel nozzle for an application in the Capstone C30 micro gas turbine. Air velocity, preheat temperature, fuel lance depth, and different thermal power ranges were varied to investigate the local heat release zones, flame stability, and flame structures.

The flame structure, especially its:

- Flame height (FH)
- Axial position of maximum intensity (APMI)
- Flame lift-off height (LOH)

was evaluated from the data obtained from each individual measurement. The steps of the data evaluation will be thoroughly described to give a better insight on how the presented graphs and images were acquired (see section 5.2.1 Data Evaluation).

5.1 Operation Limits

Originally, more than 250 operating points were planned to cover every parameter variation (air velocity, air preheat temperature, fuel lance depth, thermal power, and different pressure atomizers). A total number of 231 operating points were realizable. The remaining conditions could mainly not be reached due to extreme thermoacoustic pulsation. A detailed description of this occurred phenomenon is given in this section.

The investigated variation ranges of combustion parameters are listed in Table 5.1. The listed thermal power loads correspond to air equivalence ratios $\lambda = 1 - 2.5$ (adiabatic

temperature: 1640 – 2438 K) for all six pressure atomizers. For simplification purposes, the six nozzles listed in Table 3.1 will be named in their shortened labels.

Variation Parameter	Range	Unit
Thermal power	8 – 50	kW
Air equivalence ratio	1 – 2.5	-
Adiabatic flame temperature	1640 – 2438	K
Air velocity	80 – 120	m/s
Air preheat temperature	460 – 530	°C
Air nozzle variation	2 (see section 3.5)	nozzles
Fuel nozzle variation	6 (see section 3.6)	nozzles
Fuel lance depth	0 – 16	cm

Table 5.1 Overview of burner and combustion parameters

In addition to thermoacoustic pulsation, lean blow out (LBO) constrained the operation range of each nozzle. Exploring the lean blow out limits of the nozzles allows for determining the operability limit of the atomizers, with the least amount of fuel flow. Especially for fuel nozzle Dan45°S the exact LBO limits were acquired at different fuel lance depths and jet velocities. For all other nozzles this detailed investigation was not conducted, due to time constraints. Table 5.2 lists an overview of maximum applied λ covering different jet velocities and lance depths., these values do not represent LBO limits but indicate stable flame operation.

Nozzle	Maximum Applied λ at Different Air Velocities					Lance Depth cm
	v=80 m/s	v=90 m/s	v=100 m/s	v=110 m/s	v=120 m/s	
Dan45°H	2.1	1.7	2.0	2.1	2.2	8
Dan45°S	2.1	2.1	2.5	2.3	2.3	0,1,2,3,4,6,8,16
DIVA	1.6	1.7	2.0	2.1	2.3	8
St60°H	1.6	n.o.	1.7	n.o.	1.8	0,1,2,3,4,6,8,16
St30°S	1.4	n.o.	1.4	n.o.	2.0	8
St45°H	1.9	n.o.	2.0	2.1	2.2	8
n.o. : not operated (due to thermoacoustic pulsation)						

Table 5.2 List of maximum applied λ for all nozzles at various air velocities;
maximum applied λ for the nozzle Dan45°S corresponds with its LBO

In addition, the lance depth variation for each of the nozzle listed in the upper table gives an overview on the operated lance positions during the experiment. The given lance positions for both Dan45°S and St60°H nozzles were chosen arbitrarily and do not represent any specific air velocity.

As shown in Figure 5.1, the maximum applied λ of different nozzles is graphed over the air velocities 80 – 120 m/s. In this graph, the LBO of Dan45°S (red dots) is distinguishable from other nozzles' maximum applied λ as it lies well above other nozzles' operating points. St30°S (cyan) showed extreme thermoacoustic pulsation in higher equivalence ratios ($\lambda > 1.5$ at $v_{\text{air}} = 80 - 100$ m/s and $\lambda > 2.0$ at $v_{\text{air}} = 110 - 120$ m/s), which was presumably due to the nozzle's spray solid cone pattern and its narrow angle that led to lower atomization quality. The operability limit of this nozzle was constrained not due to LBO but mainly because of thermoacoustic pulsation causing at very narrow λ operating range. Overall, the curves show a slight increase in the λ values as the air velocity increases from 80 – 120 m/s.

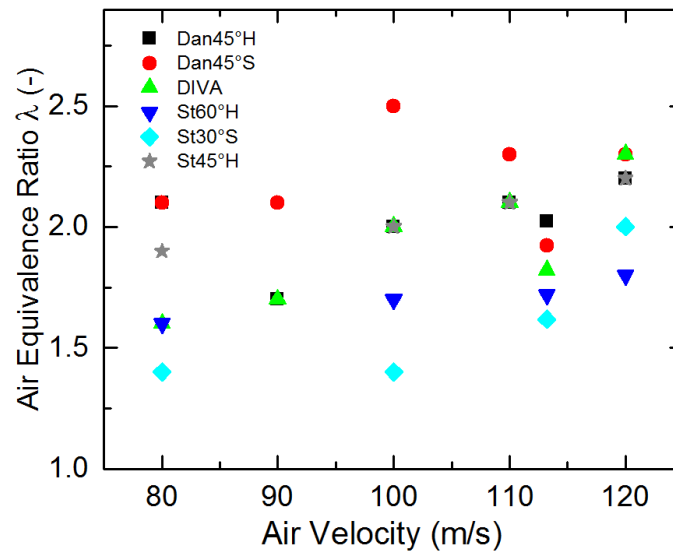


Figure 5.1 Maximum applied air equivalence ratio λ of the nozzles as a function of the air velocity at various lance depth positions

5.2 Overall Flame Structure Visualization

In this section a comparison of some of the inspected flames will be drawn and discussed. Images taken with the conventional red-green-blue (RGB) are shown in Figure 5.2 for a series of operating points with the Dan45°S fuel nozzle at a constant $T_{\text{pre}} = 460^\circ\text{C}$ and variation of

the lance depth of 0 – 2 cm and air velocities = 80, 90, 110, and 120 m/s. As shown in Figure 5.2, flame brightness and shape depend highly of the corresponding operating conditions.

In some cases, the effect of the lance depth on the flame shape, the heat release distribution, and visible soot formation can be seen. For flames with $\lambda = 1.4$, $v_{\text{air}} = 80$ and 90 m/s, and lance depth of 0 cm, the orange to white emission hints a strong local soot production, which is limited to the lower part of the flame; in the upper part, only CH^* light emission is visible, which indicates that the soot is most probably burnt within the combustor. A change in the lance depth of 2 cm for $\lambda = 1.4$ at $v_{\text{air}} = 90$ m/s, changes the liquid fuel distribution and suppresses the soot formation significantly.

The formation of locally high soot concentration is assumed to be mainly due to most of the spray hitting the air nozzle wall that results into lower atomization performance. This behavior of the flame is coupled directly to poor mixing of fuel drops with air that in return produces soot particles.

In order to evaluate air velocity effects during the λ sweeps, different thermal powers must be taken into consideration (i.e. $\lambda = 1.7$ at 80 m/s corresponds with $P_{\text{thermal}} = 31$ kW and $\lambda = 1.7$ at 120 m/s corresponds with $P_{\text{thermal}} = 47$ kW), resulting in different flame brightness levels. In addition, at air equivalence ratios $\lambda > 1.6$, the flame base started distancing itself from the burner head, which hints a delay in combustion due to the reduced fuel amount at a constant air mass flow ($v_{\text{air}} = \text{const.}$).

An extreme lift-off height is detectable with the flame at lance depth 0 cm, $v_{\text{air}} = 80$ and 90 m/s, and $\lambda = 1.9$ and 2.0, respectively, which the effect explains reduced fuel with air mixture that caused the flame to stabilize with a delay (increased lift-off height). A distinctive feature of these flames was their shooting-star alike propulsion of fuel droplets that burn while exiting the combustion chamber. This is presumably due to poor atomization of the nozzle, producing relatively large fuel droplets that before they have the chance to evaporate, crack and produce small carbon particles seen as shooting stars.[2002, Danfoss]. Spray of larger droplet was due a decrease in the nozzle pressure drop (see section 5.4).

Fuel Nozzle: Danfoss 1.00 45°S

T_{pre} : 460 °C

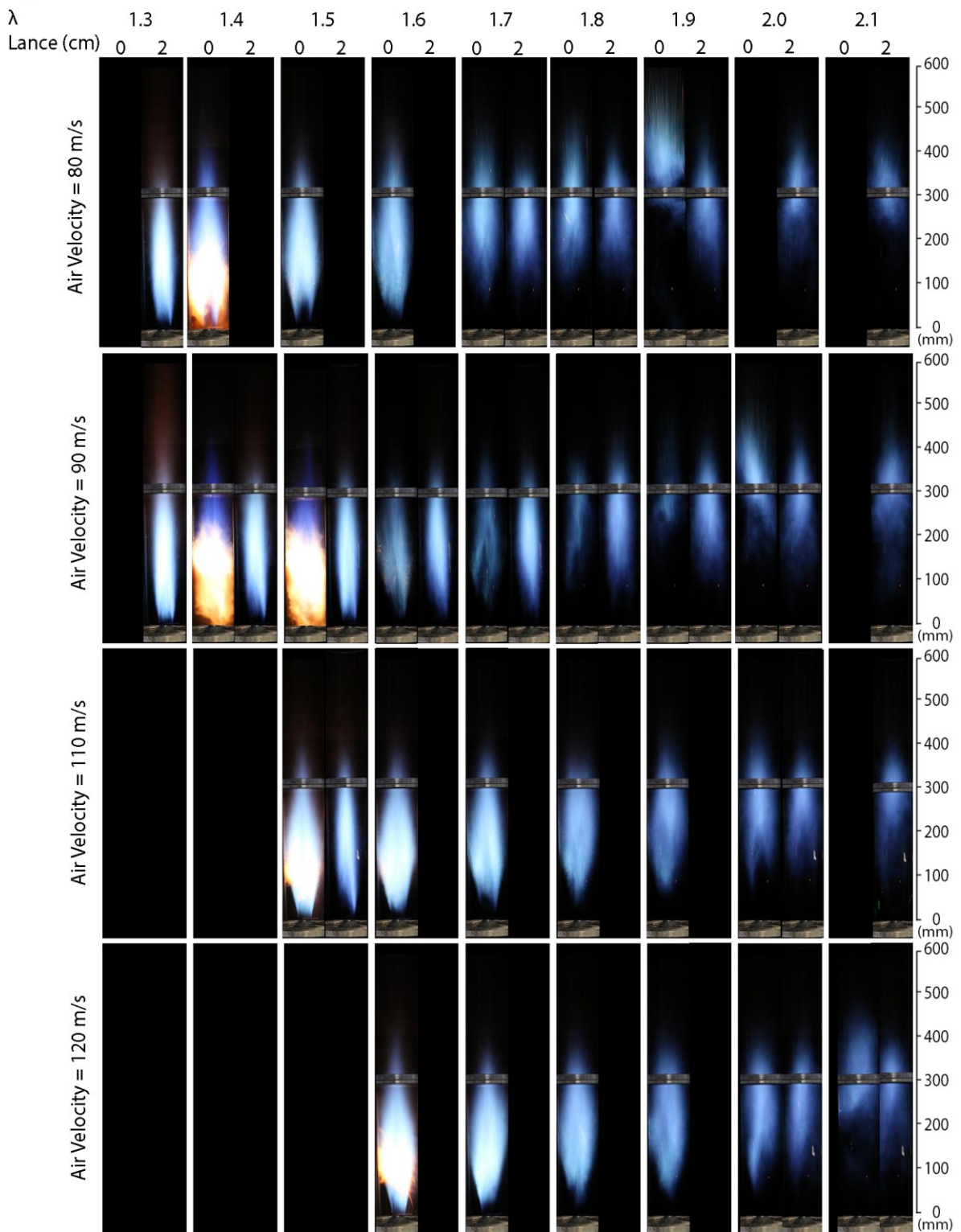


Figure 5.2 Overall view of the Dan45°S flames at $T_{pre} = 460^\circ\text{C}$, different velocities, air equivalence ratios λ , and fuel lance depths

5.3 OH*-Chemiluminescence Measurements

5.3.1 Data Evaluation

The data evaluation of the OH*-chemiluminescence required a series of steps that will be discussed in this section.

The raw data obtain from the ICCD cameras (.spe) were firstly converted into a readable format (.im7) for the post-processing software (Davis 8.3.1). Intensities of OH*-CL images are measured in counts that base on an arbitrary unit and depend on the amount of OH*-CL emission captured by the camera chips.

Figure 5.3 shows a series of steps taken to enhance the raw data to a flame structure image. In section a) of the figure, five instantaneous images are depicted that are not yet processed by dark and white field images. A dark field image was taken while the intensifier operated with the same gain as the OH*-CL measurements, here 200 (from a range of 0 – 255). The dark field image is an average of a series of images taken while the camera cap was on and represents the background noise level of the camera.

A white field image is an averaged and subsequently on its maximum count normalized image taken while the intensifier was homogenously illuminated at the same intensifier gain; it represents the spatial sensitivity distribution of the camera.

Each instantaneous OH*-CL image is then subtracted by the dark field image to remove any background noise per pixel. Additionally, the instantaneous OH*-CL images were divided by the white field image. This corrected the inhomogeneous sensitivity distribution of the intensifier chip (see Figure 5.3 b). The corrected instantaneous images were then averaged (see Figure 5.3 c).

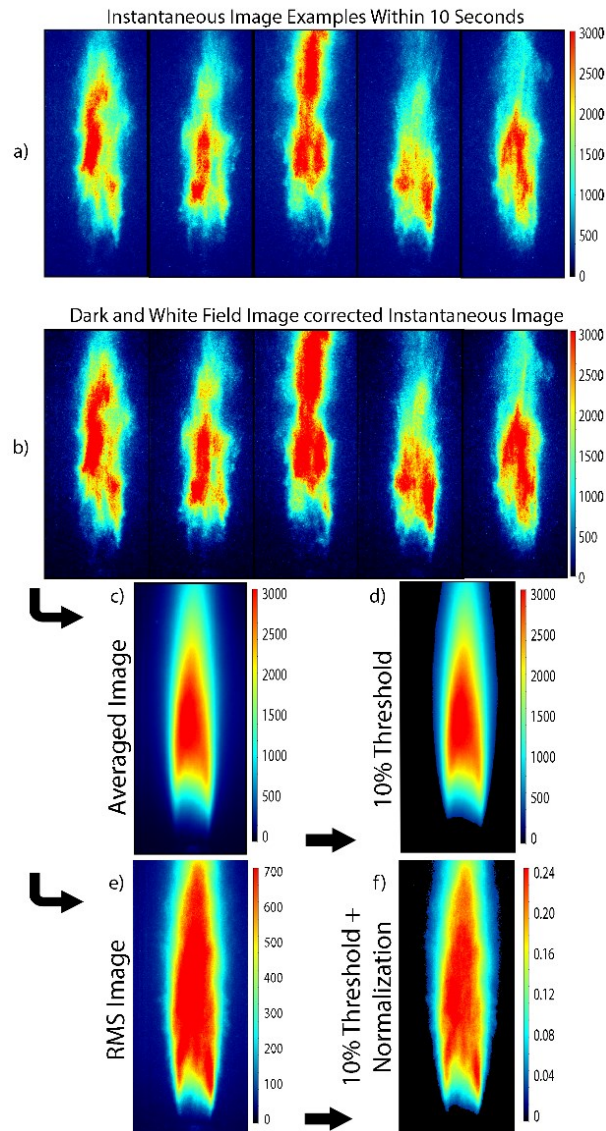


Figure 5.3 Camera characteristics correction and statistical processing of OH* emissions of the upstream part of the flame: a) 5 instantaneous images captured within 1 second, b) dark and white field corrected images, c) averaged image, d) threshold version of the average image, e) RMS image, f) threshold version of the RMS image

In order to remove excess background noise from the experiment as well as the reflections due to the cylindrical quartz glass wall, 10 % of the maximum count of the average was set to zero (threshold correction, see Figure 5.3 d). The averaged image allowed for estimating the heat release distribution within the combustion chamber without turbulent fluctuation.

As a supplementary information about flame stability, i.e. local intensity fluctuation, the root mean square (RMS) of the OH*-CL images was calculated (see Figure 5.3 e). RMS images highlight the flame zones, where most of the intensity fluctuations take place. Therefore, these images can especially help identifying stable flames with lowest fluctuations. Likewise, a threshold correction was conducted by setting the intensity counts below 10 % of the maximum count to zero, due to combustion chamber wall reflection (see Figure 5.3 f). Here, the RMS images were normalized on the maximum count of its averaged image.

As in section 4.1 OH* Chemiluminescence described, two ICCD cameras were deployed to capture as much area of the combustion chamber as possible. This led to few processing issues that needed to be solved. Firstly, background excess levels were not equally intense. It means, the lower camera background threshold was handled using a scale of 10 % of the images maximum intensity count. However, the upper camera's background needed to be trimmed by 12.5 % of the maximum intensity count of the lower image.

Secondly, a correction factor needed to be calculated that could equalize the intensity levels of both cameras. 10 operating points were chosen to detect the intensity correction factor. As shown in Figure 5.4 b), a contour plot was derived from an averaged image (Figure 5.4 a) of the lower camera at a specific intensity e.g. 1000 counts. To match the corresponding contour of the upper camera exactly, a divider was iteratively chosen. The magnification in Figure 5.4 b) depicts four images of the upper camera in different colors during the iteration, placed on top of the lower contour plot (the blue colored contour of the upper image corresponds best with the contour plot of the lower camera in yellow). This process was repeated with at least 9 other operating points to find additional individual dividers. Later, all dividers of this small subset were averaged to enable an automated data evaluation routine for all of the OH*-CL measurements. This process had to be repeated for the RMS images, and as well for the operating points with a deviating thermal power load (\varnothing 12.5 mm air nozzle and St60°H fuel nozzle). Table 5.1 lists the calculated dividers for all of the operating points and different images.

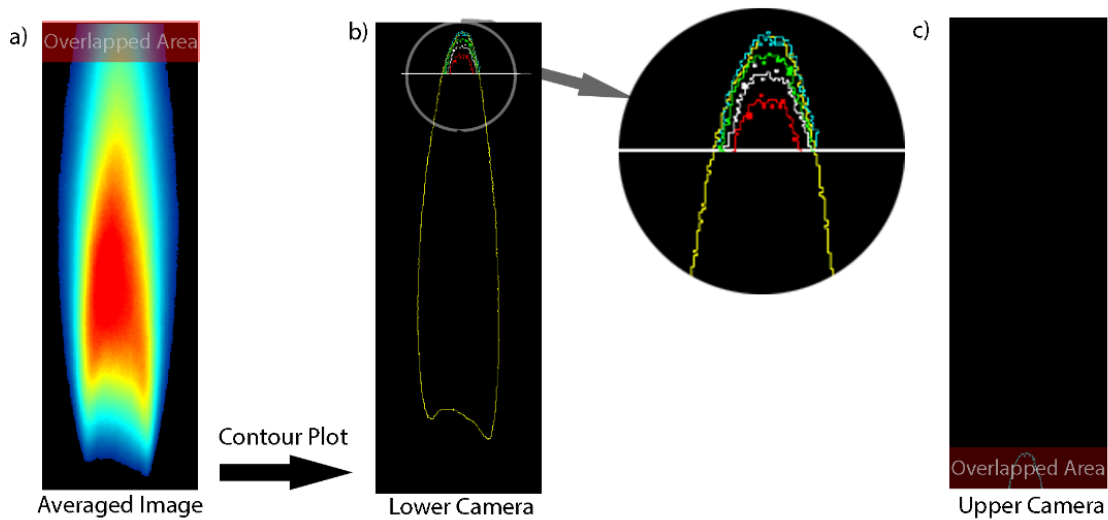


Figure 5.4 Iterative procedure of finding an intensity correction factor for the upper camera; a) overlapping area of one of the 10 selected averaged images, b) contour plot of the averaged image with magnification of its overlapping area, c) contour plot of the upper image

The detection of threshold removal rate is extremely critical for the overall accuracy of the flame structural properties analysis. Table 5.3 lists the statistically obtained correction factors for each image configuration and nozzles. For the averaged images of operating points where the St60°H was deployed a different correction factor was determined. Here, the background threshold of the averaged images could not be set constantly as no fixed rate corresponded with all of the operating points. Therefore, each individual averaged image had to be processed manually for adequately removing their background noise. Since St60°H nozzle's flow capacity was a third of other fuel nozzles tested in this work, relatively lower heat was released that in return decreased emission of OH*-CL signals. Manually processing of each image did not contribute to the accuracy of the data evaluation but was necessary for the mentioned nozzle.

Camera	Correction Factor	Threshold Correction
Lower camera (Avg. image)*	-	10 %
Lower camera (RMS image)*	-	10 %
Lower camera (St60°H)	-	manually detected
Upper camera (Avg. image)*	1.81	12.5 %
Upper camera (RMS image)*	1.61	12.5 %
Upper camera (Avg. St60°H)	1.69	manually detected
* all nozzles except for St60°H		

Table 5.3 Overview of the divider factors and threshold correction of each camera and image

Flame structural properties such as flame height, lift-off height, and axial position of maximum intensity were determined using the OH*-CL averaged images. As demonstrated in Figure 5.5, horizontal pixel counts of an OH*-CL image were accumulated and accordingly graphed over height above burner (HAB). The depicted flame is chosen randomly and merely represents the procedure on how flame structural properties were determined. At exactly 225 mm HAB, a break point can be seen; this height marks the point where both upper and lower images were merged. The inconsistency at this height is due to a not-fully accurate correction factor that was chosen to equalize the intensity scale of both of the images. At around 280 to 310 mm HAB, a break area is highlighted. This area represents the acquisition blockage of OH* emission signals caused by the combustion chamber connecting flanges. The drawback of this area is especially recognizable when a flame ended right where the flange was situated. Therefore, the exact position of the flame ending point could not be determined.

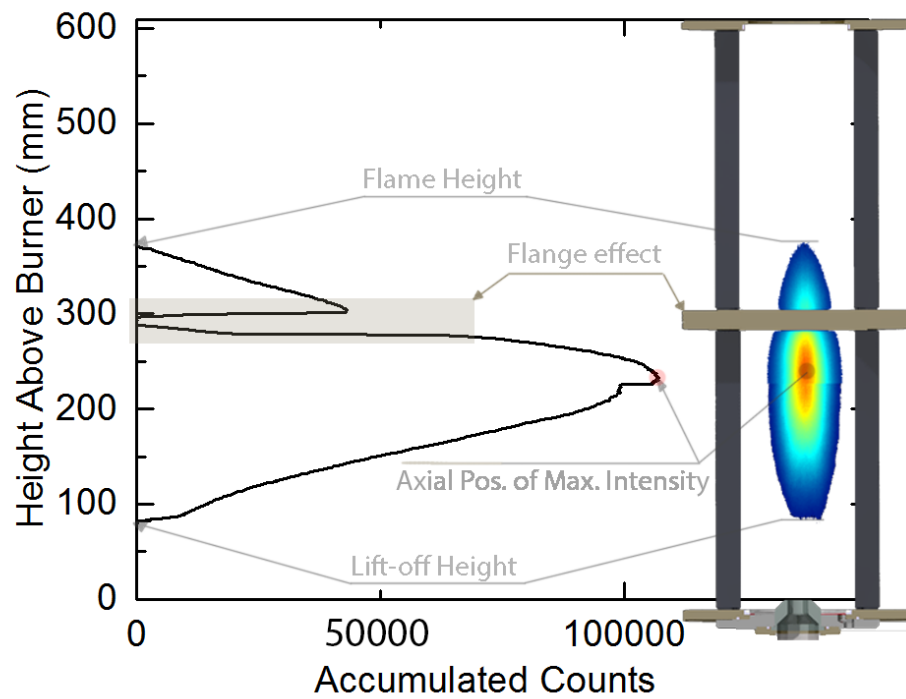


Figure 5.5 Flame structural properties extraction method used for determination of flame height, axial position of maximum intensity, and lift-off height

5.3.2 Air Equivalence Ratio Variation

As demonstrated in Figure 5.6, averaged OH*-CL images of two series of flame temperature variations with the Dan45°S fuel nozzle are aligned horizontally. The image sets represent two different lance depths, whereas the air velocity and the preheat temperature were kept constant at 100 m/s and 460°C, respectively.

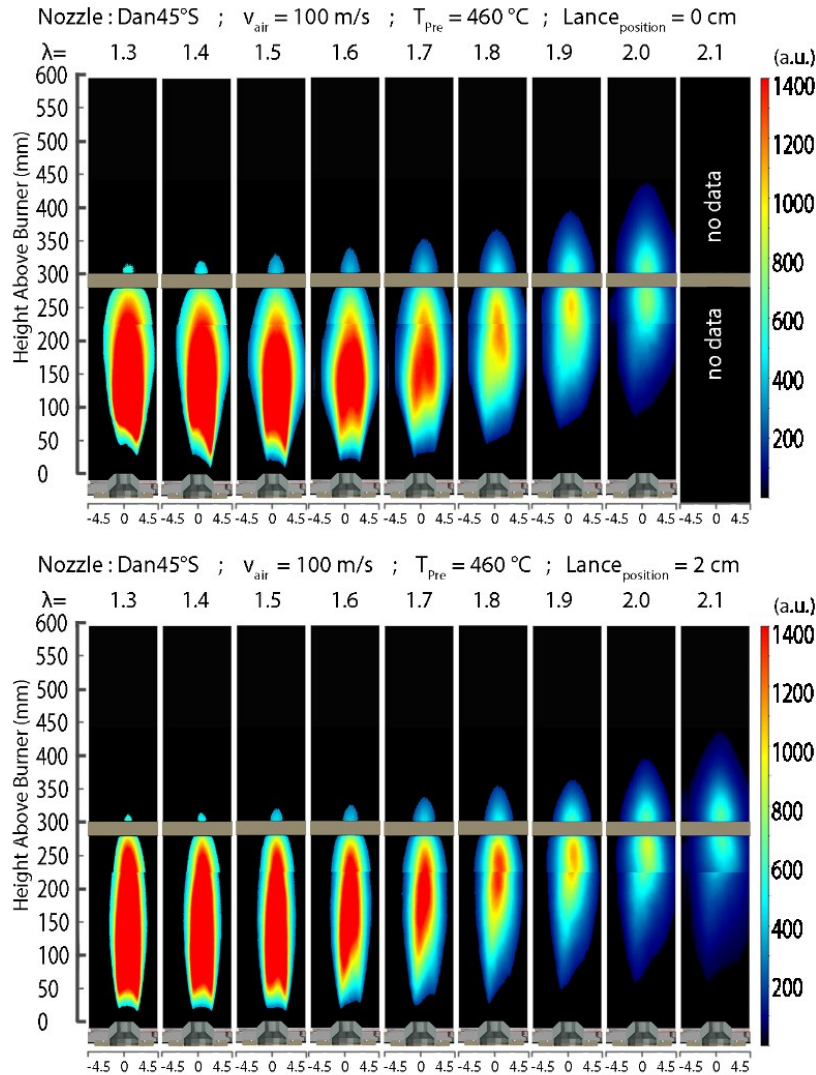


Figure 5.6 Influence of an air equivalence ratio sweep on flame heat release intensity by means of averaged OH*-CL images of Dan45°S at constant $v_{\text{air}}=100$ m/s, $T_{\text{pre}}= 460^\circ\text{C}$, Lance 0 cm (upper images), 2 cm (lower images), max count scale 1400

The intensity scales of the single images correspond to a common maximum. At low air equivalence ratios, an increase in OH*-CL can be observed: the more fuel was burnt, the higher

the intensity levels. This implies a higher heat release within the flame zone. Moreover, the images show that by increasing the fuel rate, the flame base moves toward the burner head.

By moving the fuel lance upstream (away from the air nozzle) there is more time and space for the spray to evaporate and build a better combustible premixture with fewer large drops. Flame of both depths 0 and 2 cm at $\lambda = 1.3$ to 1.7 shown in Figure 5.6 differ mostly not in flame height nor in lift-off height but width in horizontal direction. This distinctive difference of the flames is assumed to be due to different fuel distribution.

Both lance positions at 0 and 2 cm along with their resulting and nominal spray angles are depicted in Figure 5.7. In this context, the resulting and nominal spray angles are given by red and blue triangles, respectively. The wider flame at 0 cm lance position arises due to a wider spray angle exiting the air nozzle without colliding with its wall. At fuel lance position of 2 cm, the resulting angle without nozzle blockage is narrower, hence causing a narrower flame. This argumentation neglects the secondary atomization from the nozzle rim, however, it is expected that these droplets mostly follow the air flow direction with a very low radial velocity component.

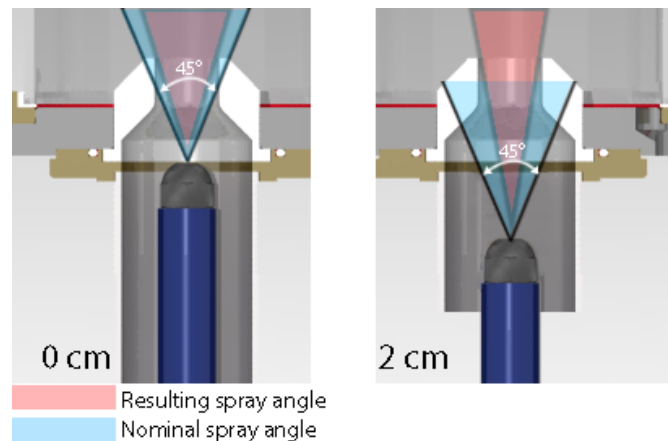


Figure 5.7 Assumed explanation of the wider flame of Dan45°S at lance depth 0 cm, operated at $v_{\text{air}}=100$ m/s and $T_{\text{pre}} = 460^\circ\text{C}$

Increasing the air equivalence ratio, e.g. $\lambda = 1.7 - 2.1$, the flames shifted downstream; simultaneously, the flames symmetrical shape was distorted. The reason for this phenomenon could lie in the fact that the combustion chamber was cooled externally by several air blowers. The heat dissipation caused by the cooling could trigger a quenching on the right side of the combustion chamber. A more probable reason for the flame to form an asymmetric shape at

higher λ could be due to non-uniform spray distribution of the nozzle. Due to lower pressure drop needed at lower fuel mass flow, it is assumed that the atomizer spray to a side and that causes the asymmetry of the flame.

For a better understanding of the length and the lift-off height of each flame, Figure 5.8 depicts graphs showing these parameters as a function of the air equivalence ratio for lance depths of 0 and 2 cm. The lift-off heights of both of the lance positions follow an identical trend, but with a slight offset. For the lance position of 0 cm, part of the liquid fuel was carried outward by shear forces of air and built a secondary atomization. It is assumed that by increasing the lance depth, a better mixing and evaporation of fuel was taking place and thus the flame base moved toward the burner head. This notion can be verified by observing Figure 5.8 (left).

A noticeable feature in Figure 5.8 (right) is the relatively flat and identical flame height course, around 280 to 350 mm, of both depths 0 and 2 cm. This means that regardless of air equivalence ratio, the same flame length is achieved. Since LOH varied by changing the equivalence ratio and FH course is almost flat, a shift of the flame upward is realized by increasing λ .

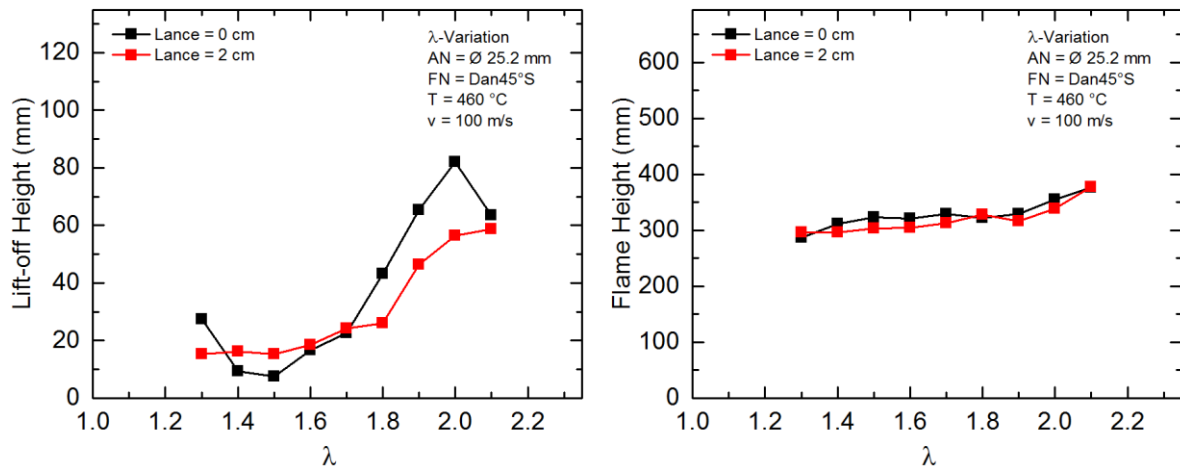


Figure 5.8 Graphs of lift-off height (left) and flame height (right) of Dan45°S at $v_{\text{air}}=100$ m/s and $T_{\text{pre}} = 460^\circ\text{C}$

The flame lift-off height offers significant information on the stabilization zone. Acquiring knowledge on flame fluctuation allows for better understanding of the mixing, atomization performance, and stability of a flame. Figure 5.10 demonstrates the flame fluctuations of the Dan45°S using RMS OH*-CL images at constant $v_{\text{air}}=100$ m/s, $T_{\text{pre}}= 460^\circ\text{C}$. For comparison purposes, the lance positions 0 cm (upper images) and 2 cm (lower images) are aligned vertically to study their influence on flames' fluctuations. For example, blue areas in the image

while operating at $\lambda = 1.3$ imply less signal appearance throughout 200 captured instantaneous OH*-CL images of the flame, hence less flame fluctuation was captured. The fluctuation zones vary as the fuel mass flow was reduced. At 0 cm lance depth, the flame with $\lambda = 1.5$ and 1.6 showed the least fluctuation in the entire flame zone when compared to the rest of operating points. These operating points were particularly interesting because the fuel flow rate, $\dot{m}_{\text{fuel}} = 1.05$ and 0.98 g/s for $\lambda = 1.5$ and 1.6, respectively, corresponded with the nominal fuel flow rate of the Dan45°S nozzle designed at a 10 bars pressure drop.

Flames obtained while operating at 2 cm lance position show lower fluctuation at lower air equivalence ratios, e.g. $\lambda = 1.3 - 1.5$, throughout the entire flames; that accounts for finer spray. This is due to more intense heat release that was observed by looking at Figure 5.6, which helped to evaporate the drops. By moving to more lean conditions, an increase in fluctuation was spotted. In the coming section, the effect of the nozzle pressure drop will be further discussed, however, it is worth noting that leaner operating points lead to lower fuel flow rate, which in return cause a fall in pressure drop and thus worse atomization and more flame fluctuation.

Figure 5.9 shows two graphs that depict flame height (left) and flame lift-off height (right) of all of the nozzles at different fuel lance positions and air equivalence ratio. As seen in the left graph, all nozzles show a relatively constant flame height of around 200 – 350 mm. The nozzle St60°H (blue hollowed points) at 16 mm lance depth was operated only during the operation of the smaller air nozzle with the exit diameter of Ø 12.5 mm. Although this flame height of this nozzle remains relatively constant at around 200 – 250 mm, its flame lift-off height rapidly increases from 40 mm at $\lambda = 1.0$ to 120 mm at $\lambda = 1.7$. This indicates improved droplet evaporation due to better spray quality that leads to a delayed flame stabilization.

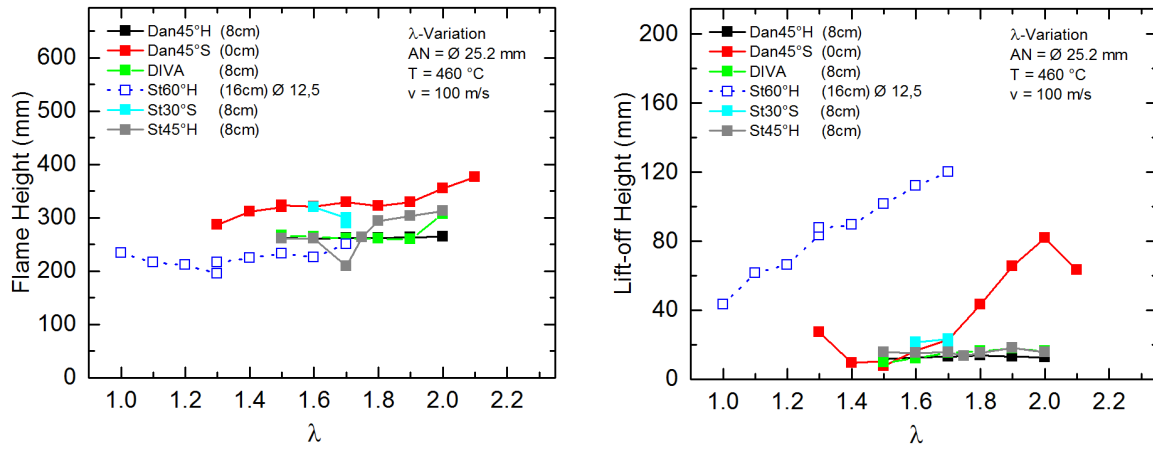


Figure 5.9 Graphs of flame height (left) and lift-off height (right) of all of the nozzles at $v_{\text{air}}=100$ m/s and $T_{\text{pre}} = 460^\circ\text{C}$

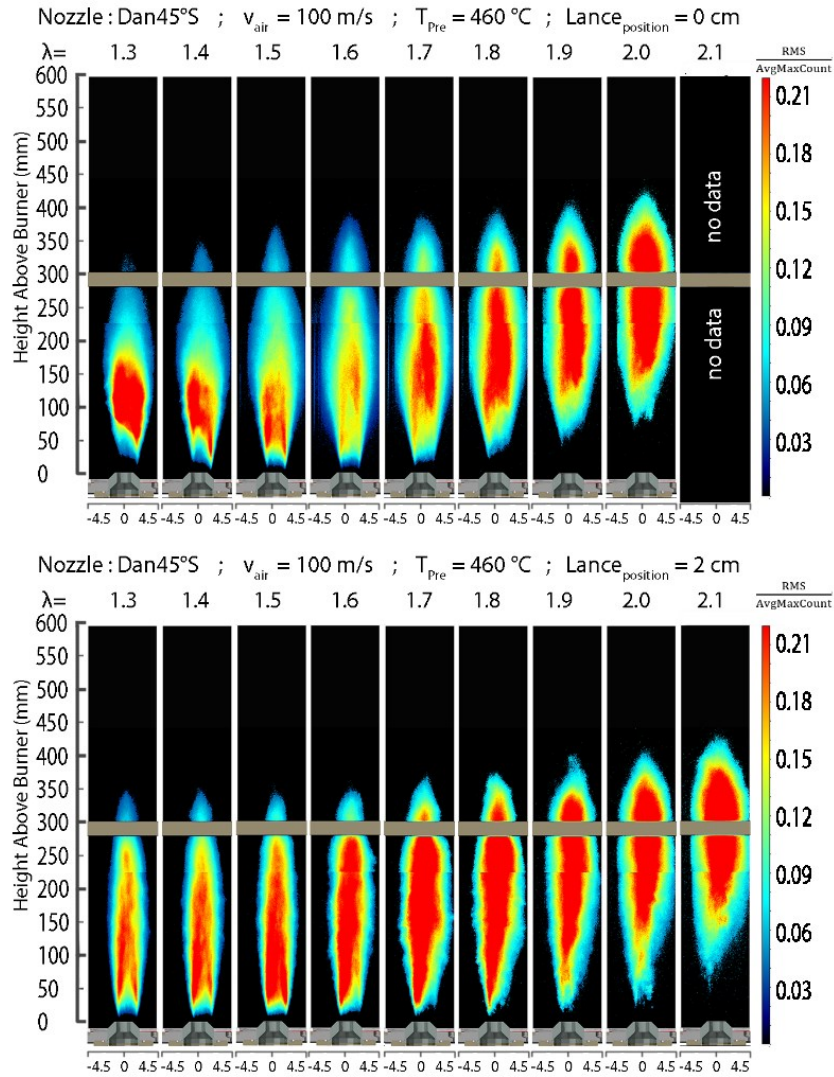


Figure 5.10 RMS OH*-CL images showing flame fluctuations of Dan45°S at constant $v_{\text{air}}=100$ m/s, $T_{\text{pre}}= 460^\circ\text{C}$, lance 0 cm (upper images), 2 cm (lower images)

5.3.3 Preheat Temperature Variation

In order to identify the influence of the air preheat temperature on the flame structural properties, an air preheat temperature sweep was run at constant λ . Figure 5.11 depicts graphs of flame height (left) and lift-off height (right) of the inspected nozzles at higher temperatures than the nominal temperature of 460°C . The operating points were run at constant air velocity $v_{\text{air}} = 100$ m/s and fuel lance position 8 cm below air nozzle. A range of temperatures of

$T_{\text{pre}} = 460 - 530^{\circ}\text{C}$ was chosen to determine the operability of the nozzle in high temperature conditions.

Observing the right graph in Figure 5.11, a rather steady flame lift-off height can be detected that accounts for very little to no influence of preheat temperatures. As the preheat temperature increases, it was expected that LOH as well as FH decrease due to a better stability of the flame and through faster reaction between fuel and air. However, unlike expected, the lift-off height of the DIVA at 460°C did not undergo much of difference (15 – 16 mm). The other nozzles follow the same pattern of behavior, except for Dan45°S. During operation of that nozzle, its lance depth was set to 4 cm below the air nozzle; that exerted an effect on both evaporation and mixing of the spray drops. In this case, LOH decreased by 60 % as the preheat temperature is increased from 460 to 530°C . Generally, it is expected to enhance the evaporation of drops by an increased preheat temperature.

A noticeable feature of Figure 5.11 (left) lies in relatively flat trend of flame heights of the investigated nozzles. observing such flat FH courses indicate that flame lengths of the nozzles remain the same regardless of nozzle type. By having different flame LOH and constant FH, a mere displacement of flame was realized by increasing preheat temperature. St30°S nozzle showed the highest LOH and FH, which was also expected: as a result of producing a solid cone spray pattern at a relatively narrow angle of 30° , larger drop sizes are created (see section 1.6.2 for more information). During testing of the nozzle, extreme thermoacoustics were encountered that hindered operating of fuel rich points. High frequency fluctuations (whistling) were encountered as a new phenomenon during the experiments while operating the St30°S.

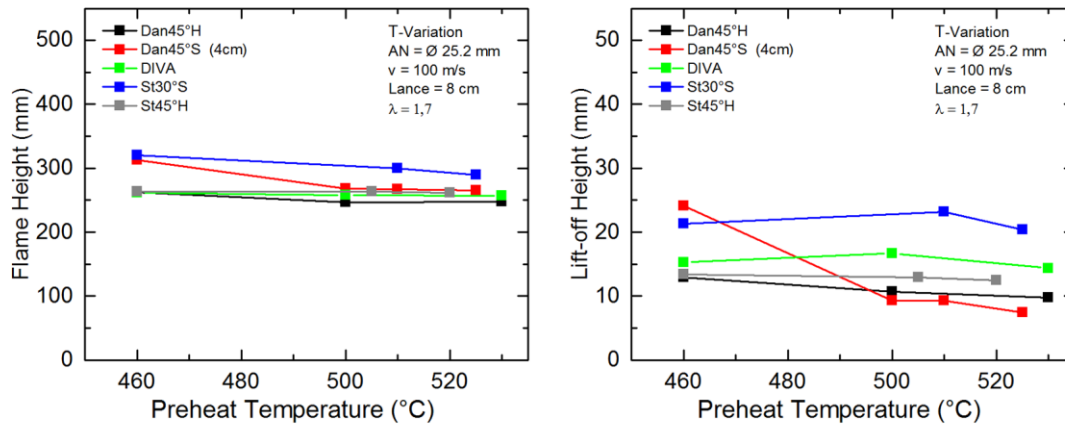


Figure 5.11 Effect of preheat temperature on flame height (left) and lift - off height (right) of various fuel nozzles measured at constant $v_{\text{air}} = 100$ m/s, 8 cm lance depth and $\lambda = 1.7$

As a secondary objective of the preheat temperature variation, it was validated that all tested nozzles could withstand the thermal load applied on their casing and can maintain normal operation.

5.3.4 Air Velocity Variation

Effects of an air velocity variation on the flame structure were examined taking OH*-CL averaged images of a series of flames. Figure 5.12 offers a graphical representation of the flame structure both as OH*-CL as well as RGB images (bottom images). The shown images originate from a series of operating points during the tests with Dan45°S nozzle at constant $T_{\text{pre}} = 460^\circ\text{C}$, lance depth of 0 cm, and air equivalence ratio of $\lambda = 1.7$.

Increasing the air velocity leads to a higher air mass flow that in case of constant air equivalence ratio leads to a higher thermal power. This leads to acceleration of the reaction between the fuel with the air that causes flame stabilization close to the burner head. The improved droplet evaporation tends to move its base toward burner head, hence decreasing the lift-off height in the upper left graph in Figure 5.12 upper right. For some air equivalence ratios, the tendency of decreasing LOH by the increasing air velocity is more noticeable. For example, flame data captured while operating at $\lambda = 1.8$ showed an intense shift in LOH from 98 mm at $v_{\text{air}} = 80$ m/s to about 40 mm when operating at $v_{\text{air}} = 120$ m/s. The reason of this phenomenon can be explained by taking thermal effect into consideration. The hotter the environment (higher

temperature), the faster the air/fuel reaction due to better fuel evaporation. The flame lift-off height graph in Figure 5.12 also includes flames with lower fuel mass flows, i.e. higher λ , that showed higher LOH than the flames in operating points with $\lambda < 1.6$.

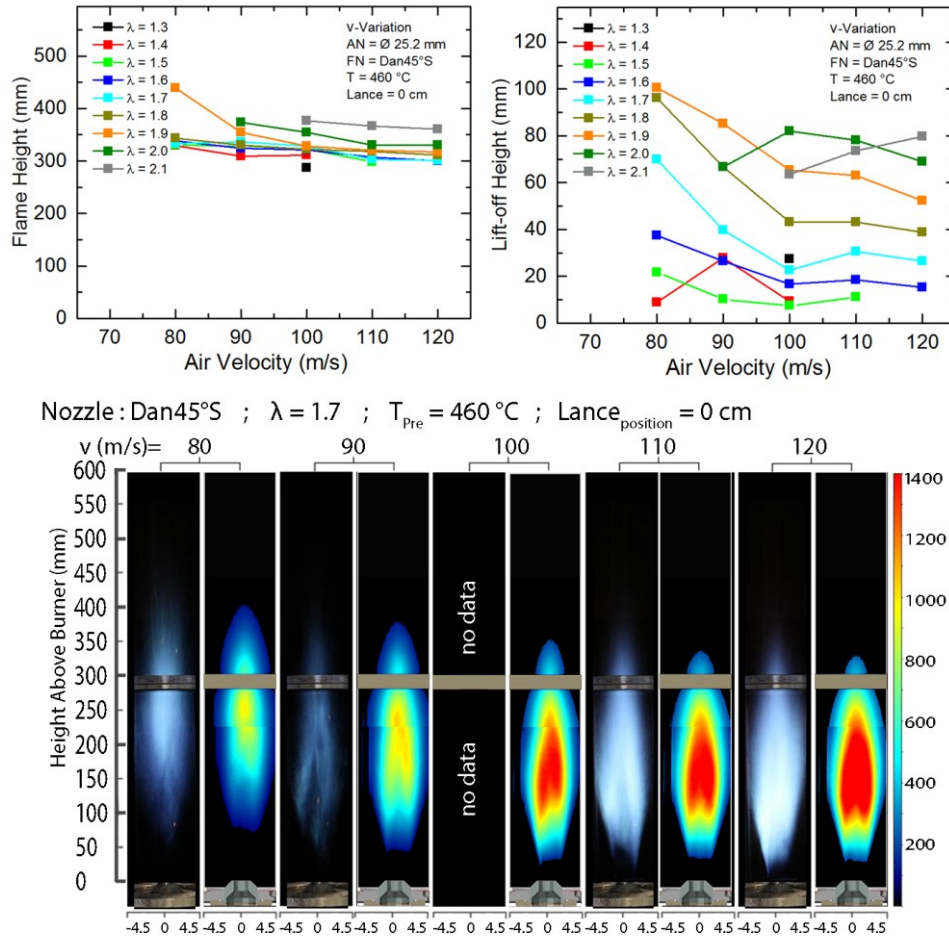


Figure 5.12 Effect of the air velocity (upper graphs) as a function of air equivalence ratio on flame height (left graph) and flame lift-off height (right graph) for Dan45°S at 0 cm lance depth and $T_{pre} = 460^\circ\text{C}$; OH*-CL averaged images (lower images) along with RGB photos of flames at $v_{air} = 80 - 120$ m/s, $\lambda = 1.7$ $T_{pre} = 460^\circ\text{C}$, and lance depth of 0 cm

Measured data show that the flames of the Dan45°S with air equivalence ratios greater than 1.6 tend to show higher LOH deviation throughout the velocity range of $v_{air} = 80 - 120$ m/s. The reason behind this is most probably that the nozzle leaves the area of good to acceptable atomization due to its pressure drop falling below the nominal value of 10 bars.

The upper left graph in Figure 5.12 highlights flame height trends for a variety of air equivalence ratios and air velocities obtained from Dan45°S. Yet again, the flame height curves

show a steady trend for all λ points at around 300 to 400 mm according to their corresponding air equivalence ratio. Taking the flames of $\lambda = 1.7$ as an example, the corresponding FH curve deviates from 320 to 300 mm at the air velocity range of 80 to 120 m/s, respectively. The curves vary relative to each other, but an individual λ trend remains fairly constant. Flames of lower air equivalence ratios tended to be more compact than the flames of higher λ . This can be explained by a higher temperature generated in lower λ points that helps atomized drops to be vaporized and react faster with air. At $\lambda = 1.9$ and $v_{\text{air}} = 80$ m/s, an unusual deviation of the flame height was detected. Its cause could lie in the OH*-CL image evaluation error margin. At lower air velocities and higher air equivalence ratios, a relatively lower heat release generates lower OH*-CL emission signals.

OH*-CL averaged images and RGB photos in the lower part of Figure 5.12 demonstrate the air velocity effect on the flames' heat release zones as well as flame geometry when operating Dan45°S at various velocities with constant $T_{\text{pre}} = 460^\circ\text{C}$, $\lambda = 1.7$, and a lance depth of 0 cm. The gradual increase of the heat release in the flame zone is easily noticeable as the air velocity increases from 80 – 120 m/s. The flame length and the lift-off height are visually comparable, noting that RGB photos represent CH*-CL emissions that are visible to naked eye. As mentioned in section 4.1, measuring the OH*-CL emissions of a flame is the established method for identifying flame characteristic properties. For visualization purposes, RGB photos can still be helpful to detect general properties of a flame, i.e. flame shape. It is worth mentioning that the ratio of OH*/CH* is not constant at different air equivalence ratios and therefore, no direct comparison of these two emissions is possible.

For comparing the Dan45°S with a another atomizer, similar graphs to Figure 5.12 were generated in Figure 5.13 that show flame height (left) and lift-off height (right) of the relatively better performing atomizer (DIVA) at $\lambda = 1.3 - 2.3$, for $v_{\text{air}} = 80 - 120$ m/s, with constant $T_{\text{pre}} = 460^\circ\text{C}$, and 8 cm lance depth. Comparing these graphs with their corresponding pair in Figure 5.12, the noticeable change of LOH courses can easily be spotted. The relatively flat LOH curves in Figure 5.13 is to a great portion owed to the lance position at 8 cm below the air nozzle. The total lift-off height deviation did not exceed 10 mm, which accounts for a relatively stable flame base at $\lambda = 1.3 - 2.3$ when varying the air velocity.

The flame height graph of DIVA is rather interesting: while showing lift-off heights at an almost constant course of about 12 to 21 mm, flame heights increased as λ increased. At

constant λ operation, however, flame height remained unchanged. For example, flame heights of DIVA operated with $\lambda = 1.8$ at air velocity of 100 to 110 m/s change from 260 to 261 mm, respectively, whereas flames with $\lambda = 2.1$ at air velocity of 110 to 120 m/s change from 326 to 324 mm, respectively. The cause lied in the decreased heat release due to lower fuel burn rate that deteriorated evaporation of fuel drops in the reaction zone; this in exchange caused the flame to be stretched downstream of air flow.

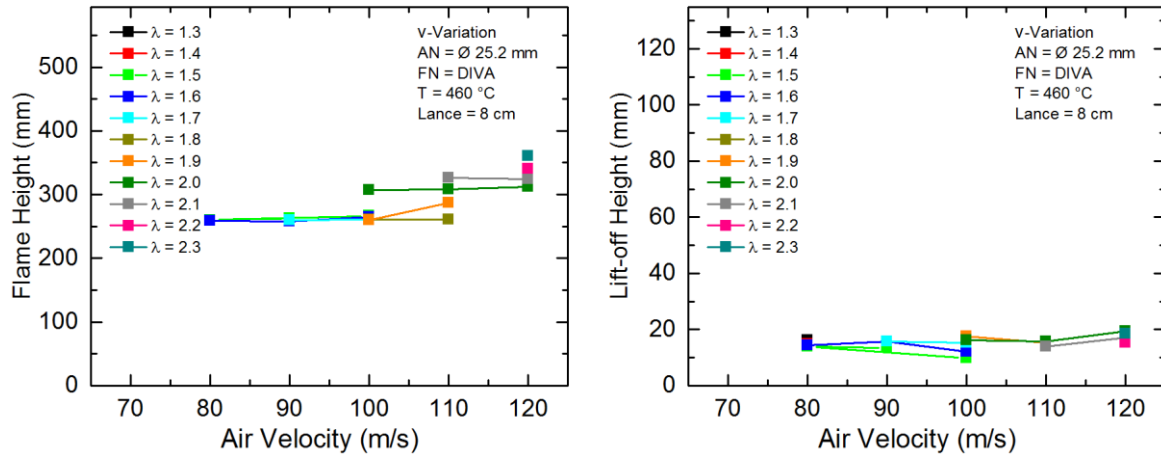


Figure 5.13 Representation of flame height (left) and lift-off height (right) of DIVA as a function of air equivalence ratio $\lambda = 1.3 - 2.3$ and air velocity $v_{\text{air}} = 80 - 120$ m/s at constant $T_{\text{pre}} = 460^\circ\text{C}$ and 8 cm lance depth

5.3.5 Fuel Lance Depth Variation

Figure 5.14 demonstrates the effect of a lance depth variation using the horizontally accumulated intensity counts of OH*-CL average images (upper left) over the height above the burner while operating Dan45°S at constant $v_{\text{air}} = 100$ m/s, $T_{\text{pre}} = 460^\circ\text{C}$, and $\lambda = 1.5$. For analyzing other visual aspects of the respective flames at different lance positions, corresponding OH*-CL averaged images are presented in the bottom part of Figure 5.14.

In the lift-off height graph in Figure 5.14 (right), the relatively constant distance between burner head and flame base is noticeable. The sole exception is the flame with 1 cm lance depth; however, the deviation is smaller than the error margin of the OH*-CL image data evaluation. Such a flat course of LOH indicates the fact that by moving the fuel lance farther away from the air nozzle, the flame base remained at about 10 mm. A relatively high thermal power of about 45 kW at $\lambda = 1.5$ and $v_{\text{air}} = 100$ m/s caused an overall rapid stabilization of the flame.

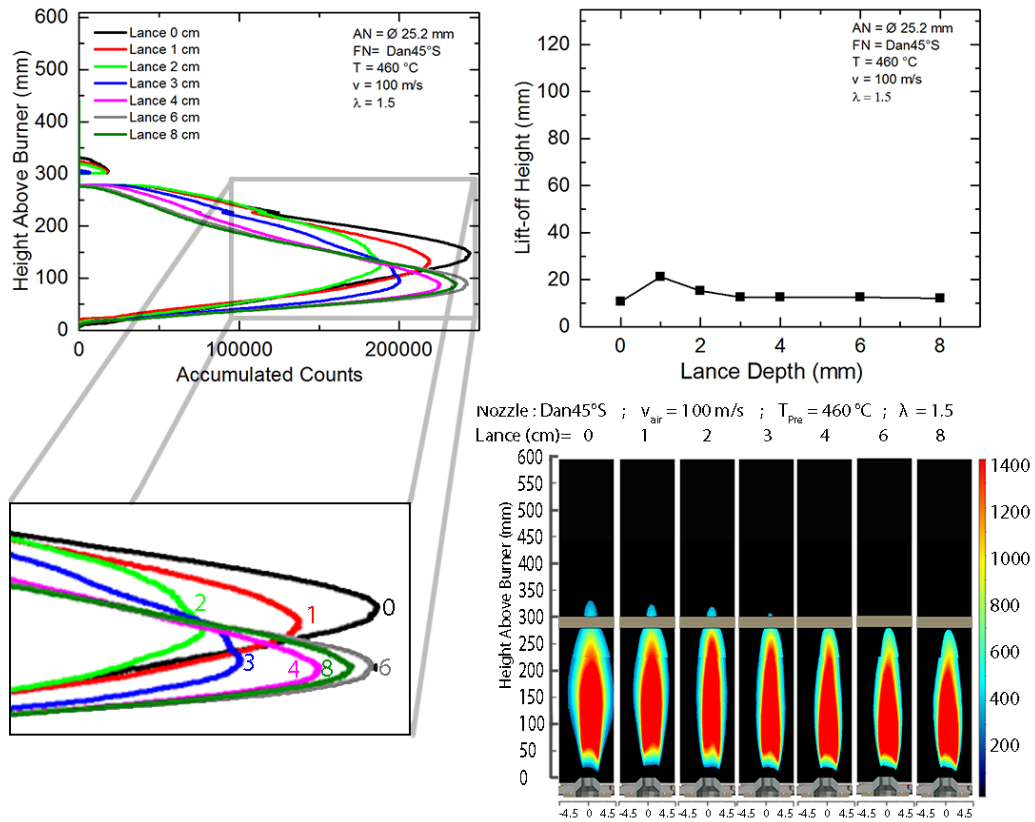


Figure 5.14 Graph demonstrating the effect of a fuel lance depth variation on the flame lift-off height (upper right) and overall intensity of flames over the height above the burner (upper left); OH*-CL averaged images (lower right) at various lance depth positions of Dan45°S at constant $v_{\text{air}} = 100 \text{ m/s}$, $T_{\text{pre}} = 460^\circ\text{C}$, and $\lambda = 1.5$

The upper left graph in Figure 5.14 allows for observing several flame features at one glance. Information about the influence of the lance depth variation is represented by different curves: the axial position of maximum intensity as curves' peaks, the flame height as the beginning of the curves, and the lift-off height as the difference between beginning of the curve and the end of it. Since LOH and FH graphs of the corresponding flames did not convey any significant dependence, this representation was chosen to visualize the shift of the axial position of maximum intensity. For lance depths of 0 and 6 cm the curves show the same peak intensity, however, the peak location is offset by 60 mm. This indicates that the droplets have more time to evaporate prior to the combustion chamber, thus flame reaction can start earlier with a 6 cm lance position.

A magnification of the axial position of maximum intensity makes detection of individual point shifting toward burner head easier. The corresponding peaks are labeled with the lance depths in cm. A trend can be observed that possibly denotes the beginning of the peaks' shifting pattern. The highest peak at 0 cm moved to the left side of the graph, which led to widening of the intensity distribution axially. This move was followed by the flame at 1 and 2 cm lance depth, note the widening of intensity distribution further more downstream of the flame, until the lance position at 3 cm reversed the direction and. Better fuel drop evaporation and entering the zone where droplets collided with air nozzle wall as a result of the lance variation are assumed to be the cause of the axial position of maximum intensity shifting upstream the flame.

The OH*-CL averaged images shown in the bottom section of Figure 5.14 visualize the lance depth effect on flame heights. As described in Figure 5.7, it is assumed that the greater effective opening width available for the spray angle at 0 cm lance depth causes wider flames compared to narrower flames of deeper lance depths.

5.4 Nozzle Pressure Drop

Pressure atomizers, as the name indicates, depend highly on the fuel pressure for generating finer or coarser sprays (see section 1.6 for more information). The pressure drop varies as the nozzle orifice area or the fuel mass flow change. The pressure drop is a good indicator, on how much energy is need for a nozzle to generate a fine spray at a certain flow rate. Table 5.4 shows an overview on the pressure atomizer nominal pressure drop in bar and their flow capacity in g/s.

Figure 5.15 (left) reveals the pressure differential measured at different air equivalence ratios of all investigated nozzles with constant $T_{pre} = 460^{\circ}\text{C}$ and $v_{air} = 100 \text{ m/s}$. In this figure, two main points can be instantly observed. First, the pressure drop of all the nozzles decreases towards fuel lean operating points. Second, the trend of St60°H fuel nozzle, which is designed for a third of the flow capacity of the other nozzles (see Table 5.4). This resulted into a deterioration of the spray quality. As a consequence, for the Dan45°S nozzle operated at a lance depth of 0 cm an increased flame lift-off height of $> 40 \text{ mm}$ can be spotted in Figure 5.15 (right), because this lance position favors the direct influence of the spray quality on combustion by minimizing the length of pre-evaporation in the mixing duct. St60°H also shows increased LOH due to lower pressure drops when operating at $\lambda > 1.4$ that caused the lift-off height to exceed 80 mm, although the nozzle was at the maximum lance depth of 16 cm

(maximum pre-vaporization time). Other nozzles such as DIVA, St45°H and Dan45°H showed relatively steady courses of the lift-off height, due to pressure drop being in 8 to 12 bars range, which covers the nominal pressure drop. An exception to the rest of the nozzles is the DIVA atomizer. The nominal pressure drop the nozzle is 3 bars at nominal flow capacity of 0.73 g/s. This Nevertheless, the lift-off height of this nozzle did not differ from the other nozzles, while operating with 1.11 – 0.81 g/s flow rate at 12 – 8.5 bars pressure drop, respectively.

Fuel Nozzle	Nominal Pressure Drop (bar)	Nominal Flow Capacity (g/s)
Dan45°S	10	1.033
Dan45°H	10	1.033
DIVA	3	0.73
St60°H	10	0.3626
St30°S	10	1.0361
St45°H	10	1.0361

Table 5.4 List of investigated nozzles with their nominal pressure drop and the corresponding flow capacity

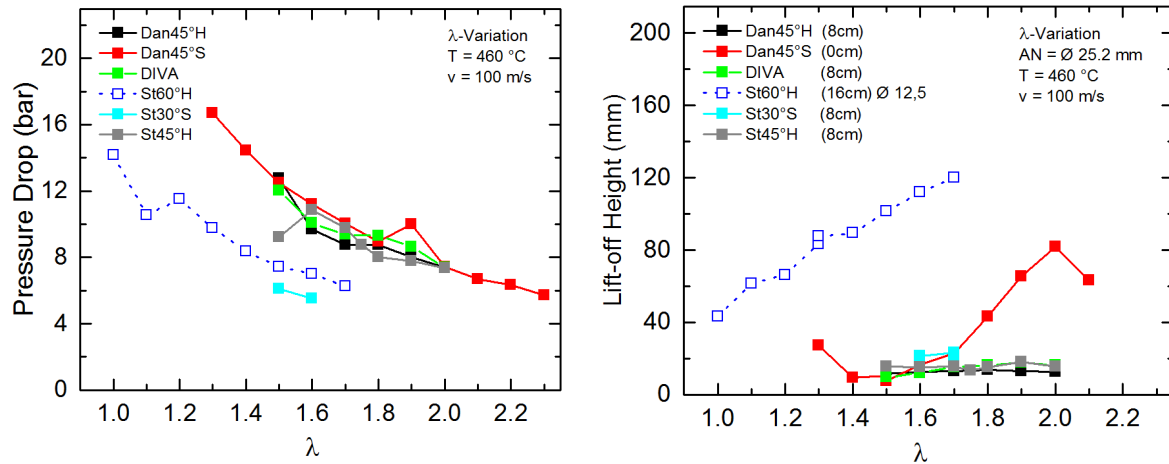


Figure 5.15 Air equivalence ratio variation of all the examined nozzles' pressure drop (left) and flame lift-off height (right) at constant $T_{\text{pre}} = 460\text{ °C}$ and $v_{\text{air}} = 100\text{ m/s}$

5.5 Mie Scattering Measurements

As described in section 4.3, scattering angle is coupled with the Mie intensity captured by the observer, in this case the ICCD camera. As the Mie angle decreases, a more intense Mie scattering can be captured. Therefore, a scattering angle of 33° was realized to detect greater Mie scattering intensity as well as to prevent laser reflection from being captured by the ICCD camera.

Mie Data Evaluation

The Mie scattering measurements were evaluated in Davis 8.3.1. Similar to the OH*-CL evaluation, the Mie images were subtracted by the dark field image to remove the background noise from the Mie images. The Mie images were divided by an averaged and subsequently on its maximum count normalized white field image. By dividing these images, the sensitivity disparity of the intensifier chip was corrected. All corrected 300 instantaneous images were averaged and normalized to detect droplet distributions above the burner head.

Variation of Air Equivalence Ratio

In the present study, Dan45°H was chosen as one of the relatively well performing pressure atomizers to visualize its spray behavior using Mie scattering. Through an air equivalence ratio sweep, fuel mass flows of 1.045, 0.865, and 0.8 g/s were achieved that corresponded to $\lambda = 1.5$, 1.8, and 2.2, respectively. In addition, air preheat temperature, air nozzle exit velocity, and lance depth were set constant at 460°C , 100 m/s, and 1 cm, respectively. The lance depth position was set at 1 cm to allow for a visualization of the droplets exiting the nozzle without the effects of evaporation inside the plenum.

Figure 5.16 depicts the evaluated Mie scattering averaged images of Dan45°H for the variation of the above mentioned parameters. The Mie scattering intensity increased as larger droplets and a denser distribution of the droplets were detected. For example, by decreasing λ , a higher fuel flow is realized that in return leads to increased Mie scattering intensity. The three operating points demonstrated in Figure 5.16 show a decrease in Mie scattering intensity as air equivalence ratio increases (left to right images). A relatively darker zone can be detected on the right side of the images that accounts for more fuel drops exiting in that zone. Drops colliding with the air nozzle wall form large chunks of drops and exit along with the air. This led to detection of more Mie scattering intensities on the right side of the images. Normally, it is expected that the same behavior should occur on the left side of each image, except for the

measurement with $\lambda = 1.5$, the rest show no sign of increased intensities on the left side. This is assumed to be mainly due absorption of laser light by the fuel droplets. However, fuel nozzle's asymmetric spray behavior should not be put out of question. By observing OH*-CL flame images in section 5.3.2, asymmetric flames can be detected while operating Dan45°S nozzle at lower λ operating points. It is assumed that by lowering the fuel flow rate, spray behavior of the nozzles changes, e.g. asymmetric spraying.

The continuous line on the left side of each image is mainly because of captured laser light reflection on combustion chamber wall and does not represent fuel drop Mie scattering.

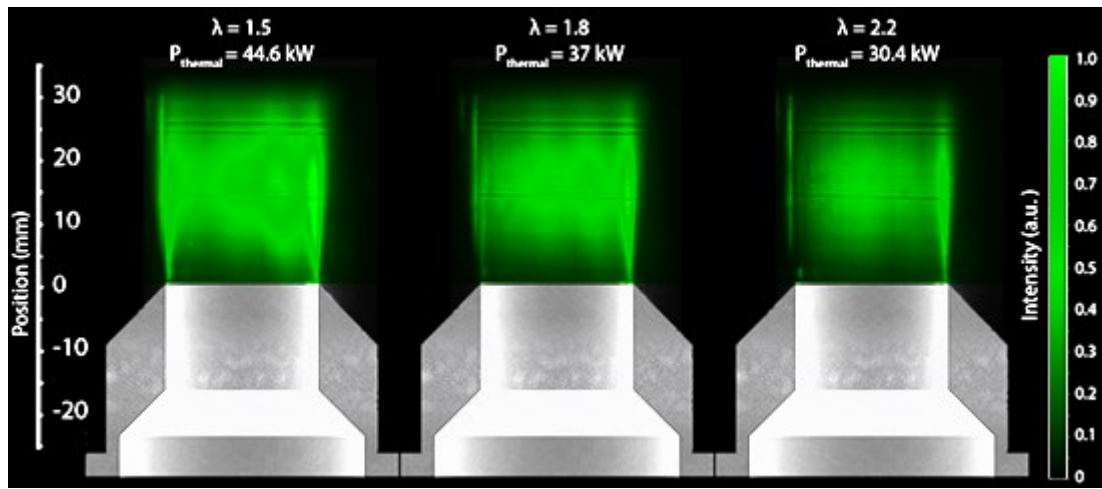


Figure 5.16 Normalized Mie scattering averaged images of Dan45°H placed on the air nozzle for variation of air equivalence ratio λ and constant $T_{pre} = 460^\circ\text{C}$, $v_{air} = 100 \text{ m/s}$, and 1 cm lance depth

Variation of fuel lance depth

A demonstration of the fuel lance depth effect on the fuel evaporation is shown in Figure 5.17. Normalized Mie scattering images of two operating points measured while operating Dan45°H are depicted for a variation of the lance depth 1 cm (left) and 8 cm (right) at constant $T_{pre} = 460^\circ\text{C}$, $v_{air} = 100 \text{ m/s}$, and $\lambda = 1.8$. In the right image, much more of fuel drops seems to be evaporated as a decreased Mie scattering intensity was captured. In contrast, the left image shows an increased Mie scattering intensity when fuel lance was positioned at 1 cm; this is due to decreased evaporation of the droplets exiting the nozzle.

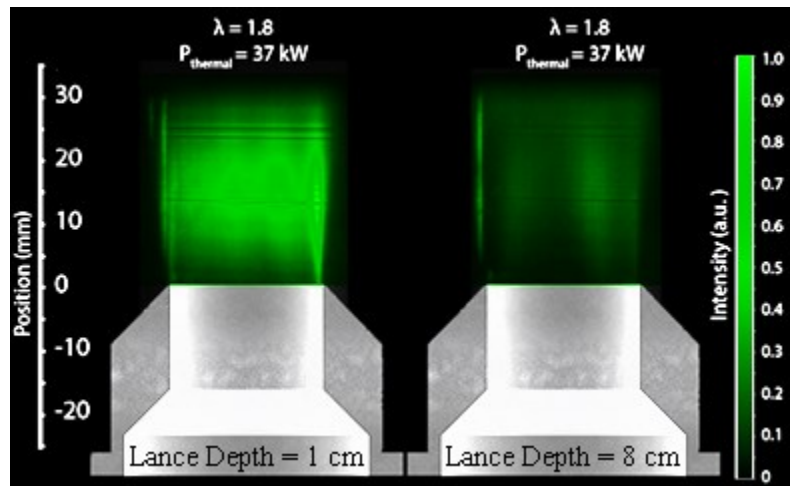


Figure 5.17 Normalized Mie scattering averaged images of Dan45°H placed on the air nozzle for variation of lance depth 1 cm (left) and 8 cm (right) at constant $T_{\text{pre}} = 460^{\circ}\text{C}$, $v_{\text{air}} = 100 \text{ m/s}$, and $\lambda = 1.8$

6 ERROR ASSESSMENT

Errors are divided into direct, largely quantifiable measurement errors (e.g. mass flows, temperatures) and interpretation inaccuracies caused by inadequate measurement techniques. For instance, a precise insight of the resulting spray inside the combustion chamber or even the spray on the injector would have been advantageous, but the use of the required measurement techniques (e.g. PDI) was beyond the scope of this work.

It is to be stated that OH*-CL images provided in this study imply merely a qualitative description of the flames, i.e. detected zones with high heat releases. The flame per se is not revealed.

The accuracy of the OH*-CL images is a question of several systematic errors, which occur while recording and during evaluation of detected hydroxyl radicals chemiluminescence emission by the ICCD camera: factors such as CCD intensifiers' life cycle, intense chemiluminescence emission reflection of the combustor cylindrical glass wall, background noise, reduced intensities during operation at higher air equivalence ratios, and target image accuracy.

While several of these errors can be corrected, others remain inaccessible (e.g. reflection on the combustion chamber wall). In the following, significant inaccuracies in the evaluation are discussed, which are important for the method developed within the scope of this work.

With the background threshold of 10% of maximum count of all averaged OH*-CL images, inaccuracies are imbedded into the results. The 10% rate was chosen as a value that corresponded with many operating points but not with all. For the sake of consistent evaluation of all of the data, this value was kept constant. For operating points, when St60°H was deployed, manual background trimming was performed as no constant threshold could be found for all the images.

Reading of the lowest point of OH*-CL images as lift-off height is a point of discussion too. Some images did not show a straight horizontal base but an anchor-shaped base that does not

necessarily relate to the lowest flame position. Therefore, OH*-CL results in this study need to be interpreted with detailed knowledge of the evaluation procedure.

In addition, given the fact, that Mie scattering images cover merely one atomizer and a limited number of operating points, the results should therefore not be used for numerical simulation validation.

In this section, several measurement errors are named and analyzed: air and fuel mass flow measurement and air preheating temperature.

During the experiments, the fuel mass flow controller suffered from flow fluctuations caused by over-pressurized piston accumulator. This led to continuous wobbling of fuel flow that resulted into inaccurate air equivalence ratio. In cases where this inconsistency of mass flow was detected, measurements were repeated, however, the slight undetectable mass flow deviations could lead to minimized inaccuracy of the thermal power stated in each OH*-CL measurement.

Specifically, the air mass flow controller showed an averaged deviation of 0.37 %, e.g. at the constant air velocity of 100 m/s. A further factor that influenced the air mass flow was the preheat temperature that was regulated by the electric preheater. Since the air mass flow was regulated using the air velocity exiting air nozzle, the preheat temperature (or the air density) had a direct influence on the air mass flow. During a single operating point, where air and fuel mass flows were set constant, the preheater regulator showed a deviation of 8 °C that represents 1.7 % temperature deviation at 460°C. This temperature deviation meant an additional inaccuracy in the air mass flow of about 1%. This shows that preheat temperature deviation had greater effect on the accuracy of the air mass flow than the deviation of the air mass flow controller itself.

It should be mentioned that the temperature readings were registered at the bottom of the mixing plenum and any temperature loss along the plenum up until the air nozzle exit was omitted. Although the plenum was insulated, there must have been a temperature loss along the 16 cm-long plenum.

The thermal power was regulated by the variation of the air equivalence ratio (fuel mass flow). By taking the accuracy of the fuel mass controller into account, the deviation of the thermal power can be attained. The fuel mass flow controller showed an averaged deviation of about

0.39% at stationary operating points. This also represents the accuracy of the measured thermal power.

Both the air and the fuel mass flow accuracies mentioned above contribute to additional discrepancies in the air equivalence ratio stated at each OH*-CL and Mie scattering measurements. Therefore, the evaluated data within the scope of this work must be interpreted with caution.

7 SUMMARY, CONCLUSIONS, AND RECOMMENDATION

7.1 Summary

Recent progress of battery electric vehicles has attracted the attention of major automotive manufacturers to develop methods that can extend the vehicles' range. This has led to the creation of an effective vehicle concept, which integrates a combustion engine into a battery electric vehicle, designated as range extended battery vehicle. In this regard, micro gas turbine (MGT) engines offer a great suitability as a range extending unit mainly due to their specific power density, improved emission levels, and fuel flexibility.

For the range extender application, the MGTs need to go through a series of modifications in regard to their weight, operation reliability, and combustion efficiency, and low emission levels at various part loads. Extensive development is needed in the core of the MGTs' combustor to meet these requirements. Among other factors, the atomization of the fuel is a key to achieving these requirements.

The current study focused on finding off-the-shelf commercial fuel pressure atomizers that were intended to be integrated into a micro gas turbine for a range extender application. Established experimental data showed that combustion stability and soot formation were depending on the atomization performance of the individual fuel nozzles. In this regard, a set of design parameters was chosen to identify the influencing factors on atomization and flame behavior.

An important objective of the current work's experiments was to examine the functionality of the pressure nozzles in high preheat temperatures of above 460 °C, where coking is a major cause for blockage of the internal fuel ducts. These issues had posed a challenge for the precious work.

OH*chemiluminescence measurements were made to study structural properties of the flame. In addition, Mie scattering measurement were done with one of the best performing atomizers

for further studying fuel drop distribution and vaporization at various air equivalence ratio and different fuel lance depths.

7.2 Conclusions

No fuel nozzle coking was observed during the experiments despite operating above MGT's actual air preheat temperatures of 460 °C. This was presumably due to larger fuel nozzle orifice exit with greater flow number used for this work compared to [2017, Schäfer] work, where the injectors had $1/4$ of the flow capacity of the currently investigated injectors.

The obtained data from OH*-CL and Mie scattering images allowed a good understanding of the parameter interaction as well as their collective effect on the flame. By increasing the fuel lance depth at constant air equivalence ratio and air preheat temperature, lower flame lift-off height was observed that signalizes an improved fuel droplet vaporization within the premixture plenum.

The air preheat temperature did not show any significant influence on the flame shape nor the lift-off height. It is assumed that the temperature increase was not sufficient enough to make any effective impact on the flame. An air velocity sweep affected the flame lift-off height but not the flame length. An increased air velocity at constant thermal power caused a reduction of the distance between the flame base and the burner head.

Measurements of the fuel nozzles' pressure drop allowed a better understanding of the injector behavior. An increased flame lift-off height was observed while operating the nozzles at higher air equivalence ratios. It is assumed that by lowering the fuel flow rate and thus needing a lower pressure drop, spray quality of the nozzles degrade that leads to increased flame lift-off heights.

Mie scattering images offered a visualization of the fuel droplet distribution above the air nozzle exit. A variation of the air equivalence ratio showed different fuel drop distributions as fuel flows varied from 0.8 – 1.045 g/s. Due to increased amount of atomized fuel, higher intensities were detected at $\lambda = 1.5$, whereas a more uniform and less intense Mie scattering was detected at $\lambda = 2.2$. In addition, the detected Mie scattering intensities showed an obvious increase of the fuel droplet vaporization while comparing lance depths at 1 and 8 cm.

Among all the tested pressure atomizers of three different manufacturers, two hollow and solid spray cone, and three spray angles of 30°, 45°, and 60°, DIVA and Dan45°H outperformed the

rest of the nozzles. Frequent thermoacoustic pulsation was observed while operating St30°S that presumably accounts for its narrow spray angle of 30° and its solid spray cone.

7.3 Recommendation

Testing the pressure atomizers in a wide range of operating points revealed the influence of the design parameters on the atomization behavior and thus structural properties of the flame. It was identified that by varying the fuel flow rate of the injectors, the flame base shifted up- and downstream. It is recommended that during the operation of the MGT below the maximum load, one or two of the fuel nozzles discontinue operation. This way, the nozzles can operate at the nominal pressure drop during most of the part loads. For instance, should the MGT operate in a part load of 50 – 70 %, one of the nozzles should be deactivated so the rest of the available nozzle preserve their nominal flow rate, where they guarantee an adequate atomization at their nominal pressure drop. This strategy can be adopted at lower thermal loads (e.g. 20 – 40 %), deploying only one nozzle.

A more accurate characterization of the individual pressure atomizers requires tests at the nominal combustion chamber pressure of 3.5 bars. This can contribute to a final validation of the present study's results on finding the best performing pressure atomizer for the range extender micro gas turbine combustor. The current study found the examined pressure atomizers with a hollow spray cone outperformed the nozzle with solid spray cone. Therefore, it is recommended that pressure atomizers of larger spray angles with hollow cone should be used to achieve shorter flames.

8 REFERENCES

- ALBREGTSEN, F. 2008. *Reflection, Refraction, Diffraction, and Scattering*.
- ASHGRIZ, N. 2011. *Handbook of Atomization and Sprays Theory and Applications*. New York: Springer,.
- BACHALO, W. D. 1980. Method for Measuring the Size and Velocity of Spheres by Dual-Beam Light Scatter Interferometry. *Appl. Opt*, 19, 363–370.
- BALLESTER, J., GARCIA, T. & ARMINGOL 2010. Diagnostic Techniques for the Monitoring and Control of Practical Flames. *Progress in Energy and Combustion Science*.
- BALLESTER, J. & HERNÁNDEZ, R. 2007. Flame Imaging as a Diagnostic Tool for Industrial Combustion.
- C30-DATASHEET 2010. C30 Natural Gas Data Sheet.
- CORI-FLOW-DATA-SHEET, M. Technical Data Sheet: Mini Cori-Flow.
- DANFOSS 2002. Facts Worth Knowing About Oil Nozzles.
- DANFOSS 2014. Technical Data Sheet: Oil Nozzle Type Od Vb.Ce.K2.02.
- DELAVAN-NOZZLES 2000. A Total Look at Oil Burner Nozzles - Data Sheet.

- DING, Y., DUROX, D., DARABIHA, N. & SCHULLER, T. 2017. Possibility of Applying Flame Chemiluminescence and Ionization Current to the Combustion Status Monitoring. *26th ICDERS*.
- EPA-REPORT 1999. Technical Report Data: Nitrogen Oxides (Nox), Why and How They Are Controlled. North Carolina: U.S. Environmental Protection Agency.
- FANSLER, T. D. & PARRISH, S. E. 2015. Spray Measurement Technology: A Review, *Meas. Sci. Technol.* 26, 1-35.
- FRIEDRICH, H., WIDENHORN, A. & HENKE, M. 2012. Studie Zu Range Extender Konzepten Für Den Einsatz in Einem Batterieelektrischen Fahrzeug – Rexel. Institut für Verbrennungstechnik, Stuttgart.
- GEDDIS, P. J. 2009. *Evaluation of Chemiluminescence as a Measurement Option for Industrial Flame Monitoring and Process Control*. University of Toronto.
- GOUNDER, J. D., ZIZIN, A., LAMMEL, O. & AIGNER, M. 2016. Spray Characteristics Measured in a New Flox® Based Low Emission Combustor for Liquid Fuels Using Laser and Optical Diagnostics. *ASME Turbo Expo 2016: Turbomachinery Technical Conference and Exposition*.
- GUYOT, D., GUETHE, F., SCHUERMANS, B., GUYOT, D., GUETHE, F. & SCHUERMANS, B. 2010. CH^*/OH^* Chemiluminescence Response of an Atmospheric Premixed Flame under Varying Operating Conditions. *ASME Turbo Expo 2010: Power for Land, Sea and Air*.
- HAMILTON, S. 1999. Micro Turbine Generator (Distributed Generation) Project.
- HAMILTON, S. 2003. *The Handbook of Microturbine Generators*, Tulsa, Okla., Pennwell Corp.
- JOOS, F. 2006. *Technische Verbrennung: Verbrennungstechnik, Verbrennungsmodellierung, Emissionen ; Mit 65 Tabellen*, Berlin u.a., Springer.
- KINIGADNER, A. & KIRCHNE, E. 2014. Electric Driving without Range Anxiety. Schaeffler Kolloquium.
- KIRCHNER, E. 2007. *Leistungsübertragung in Fahrzeuggetrieben*, Berlin, Springer.
- LARMINIE, J. & LOWRY, J. 2012. *Electric Vehicle Technology Explained*, Southern Gate, Chichester, West Sussex, PO19 8SQ, United Kingdom, John Wiley & Sons, Ltd., Publication.

- LAW, C. K. 2006. *Combustion Physics*, New York, Cambridge University Press.
- LEFEBVRE, A. H. & BALLAL, D. R. 2010. Gas Turbine Combustion : Alternative Fuels and Emissions. 3rd ed. Boca Raton: Taylor & Francis,.
- LEFEBVRE, A. H. & MCDONELL, V. G. 2017. Atomization and Sprays. Second edition. ed. Boca Raton: CRC Press,.
- LU, D., OUYANG, M., LU, L. & LI, J. 2010. Theoretical Performance of a New Kind of Range Extended Electric Vehicle. *World Electric Vehicle Journal*, 4.
- MEIER, W. 2015. Wissenschaftliche Und Technologische Ergebnisse, Statusbericht 2007 - 2015.
- MOCK, P. 2010. *Entwicklung Eines Szenariomodells Zur Simulation Der Zukünftigen Marktanteile Und Co2-Emissionen Von Kraftfahrzeugen* Deutsches Zentrum für Luft- und Raumfahrt, Institut für Fahrzeugkonzepte.
- NASR, G. G., YULE, A. J. & BENDIG, L. 2002. *Industrial Sprays and Atomization : Design, Analysis and Applications*, London ; New York, Springer.
- PHILLIPS, J. N. & SIMAS, P. 2004. Gas Turbine Fuel Nozzle Refurbishment.
- ROEDIGER, T., LAMMEL, O., AIGNER, M., BECK, C. & KREBS, W. 2012. Part-Load Operation of a Piloted Flox® Combustion System. *ASME Turbo Expo 2012*.
- SCHÄFER, D. 2017. *Untersuchung Der Einflüsse Verschiedener Zerstäuber Auf Die Leistung Eines 2-Düsen-Füssig-Flox®-Brenners*.
- SCHICK, R. J. 2008. Spray Technology Reference Guide: Understanding Drop Size. Wheaton, IL, USA: Spraying Systems Co. .
- SINGHAM, S. B. & BOHREN, C. F. 1993. Scattering of Unpolarized and Polarized Light by Particle Aggregates of Different Size and Fractal Dimension.
- STAMATOGLOU, P. 2014. *Spectral Analysis of Flame Emission for Optimization of Combustion Devices on Marine Vessels*. Lund University.
- STEINEN 2016. Steinen Nozzle Catalog Oil Burner 2016
- WÜNNING, J. G. Flameless Combustion and Its Applications.

ZANGER, J., MONZ, T. & AIGNER, M. 2015. Experimental Investigation of the Combustion Characteristics of a Double-Staged Flox®-Based Combustor on an Atmospheric and a Micro Gas Turbine Test Rig. *ASME Turbo Expo 2015: Turbine Technical Conference and Exposition*.

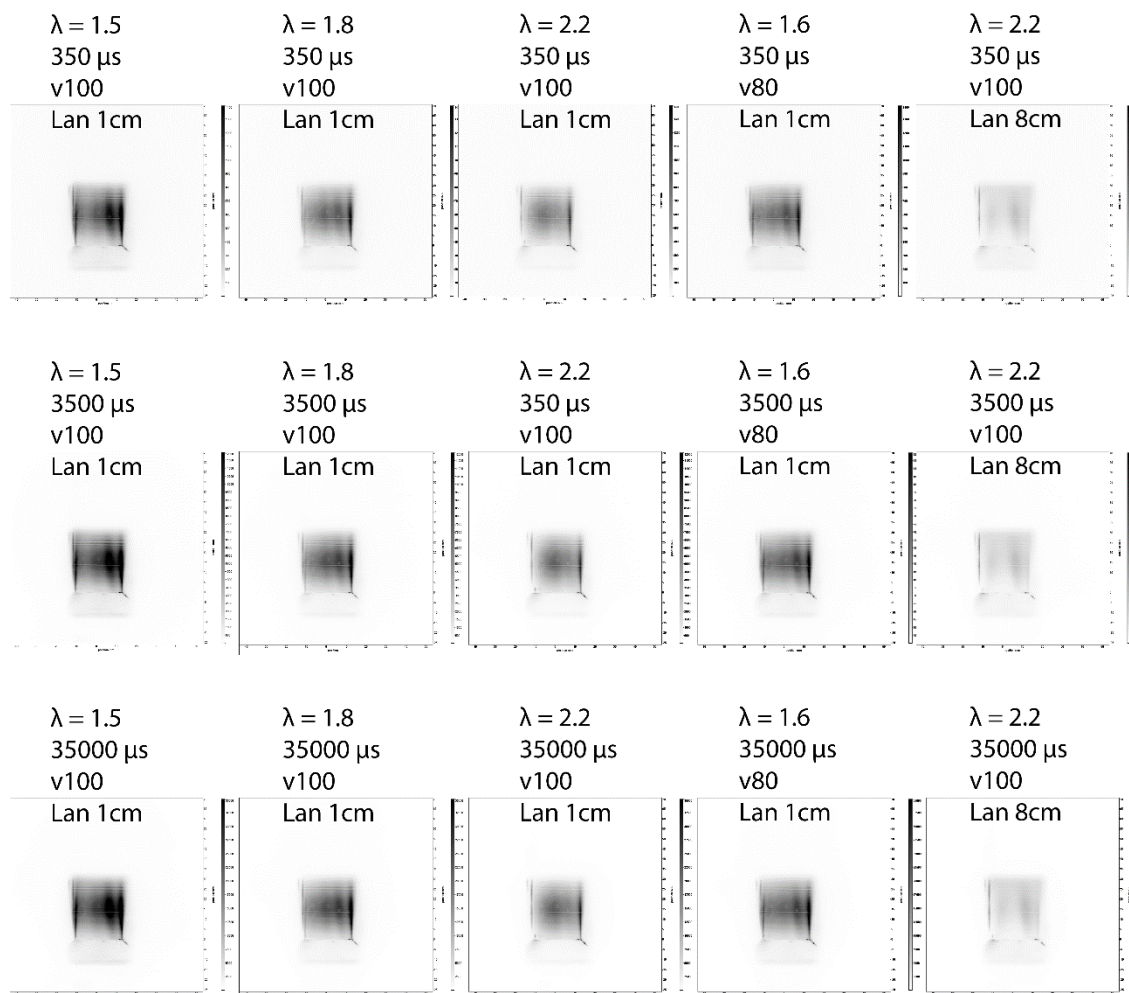
ZIZIN, A., LAMMEL, O., SEVERIN, M., AX, H. & AIGNER, M. 2015. Development of a Jet-Stabilized Low-Emission Combustor for Liquid Fuels. *ASME 2015 Turbo Expo - Power for Land, Sea and Air*.

9 APPENDICES

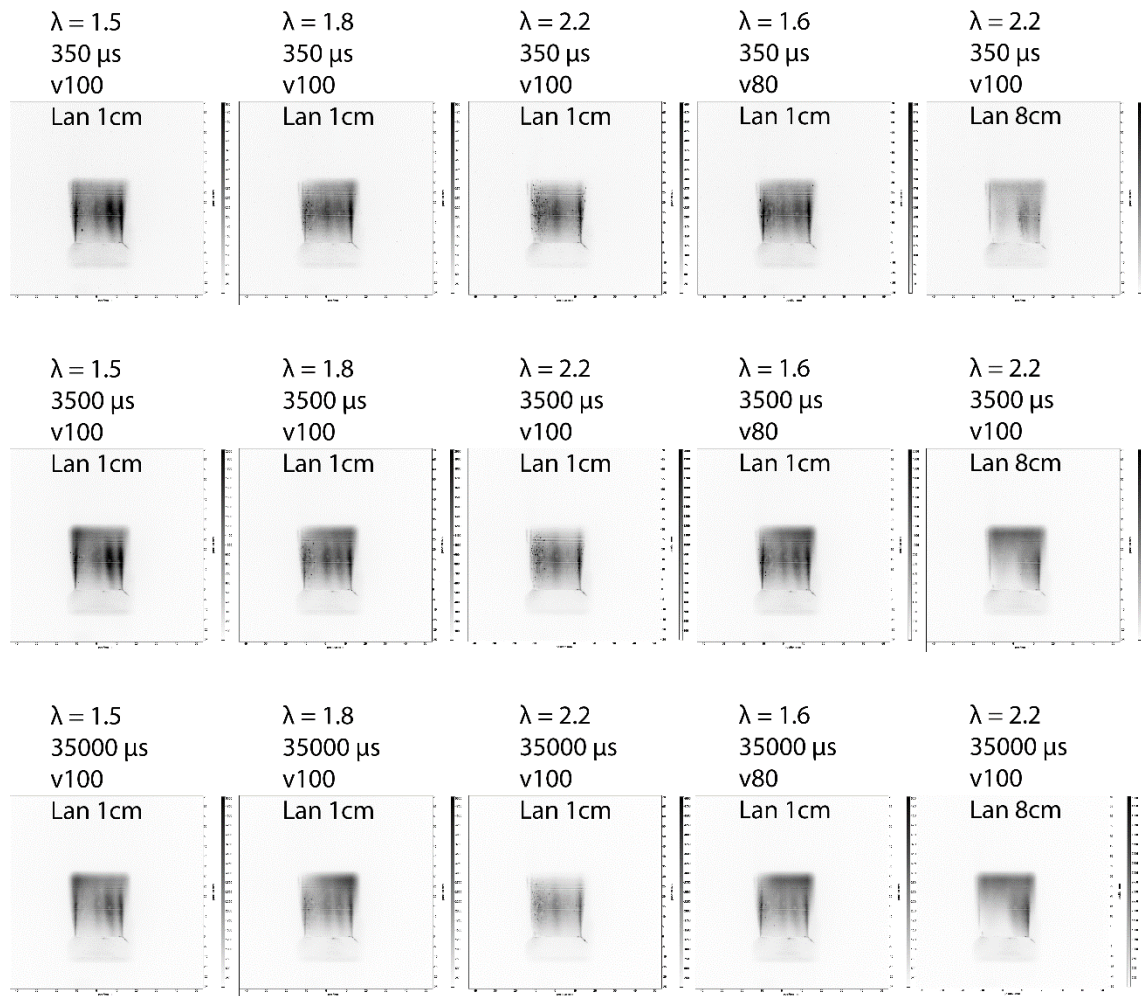
Appendix 1 Mie Scattering	79
Appendix 2 Averaged OH*-CL Images	81
Appendix 3 RMS OH*-CL Images.....	94
Appendix 4 Graphs: Flame Structural Properties	103

APPENDIX 1 MIE SCATTERING

Averaged Mie Scattering images at 350, 3 500, 35 000 μs gate time



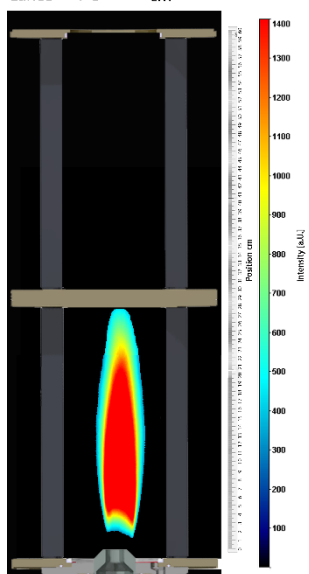
RMS Mie Scattering images at 350, 3 500, 35 000 μs gate time



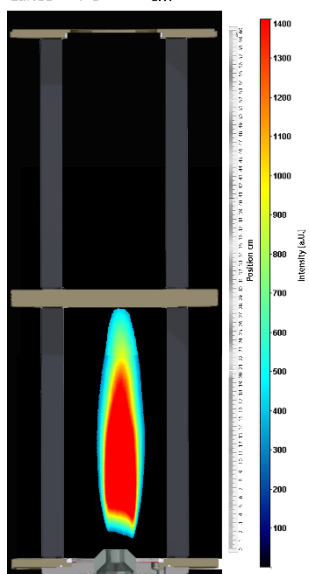
APPENDIX 2 AVERAGED OH*-CL IMAGES

DIVA

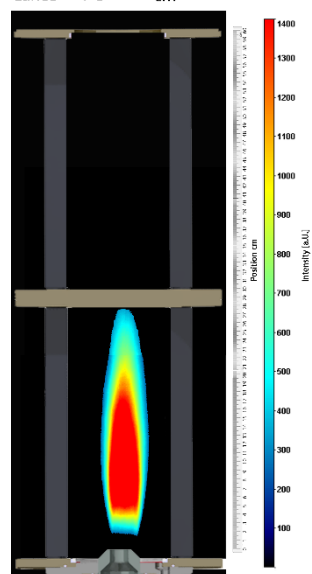
A. nozzle : Ø25.2 Semi-conical
 F. nozzle : DIVA
 v : 100 m/s
 T : 465 °C
 λ : 1.5
 P_{TH} : 45 kW
 LOH : 10 mm
 COM : 76 mm
 FL : 267 mm
 Lance : 8 cm



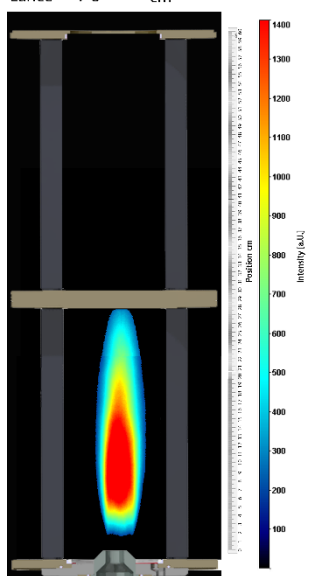
A. nozzle : Ø25.2 Semi-conical
 F. nozzle : DIVA
 v : 100 m/s
 T : 465 °C
 λ : 1.6
 P_{TH} : 42 kW
 LOH : 12 mm
 COM : 89 mm
 FL : 265 mm
 Lance : 8 cm



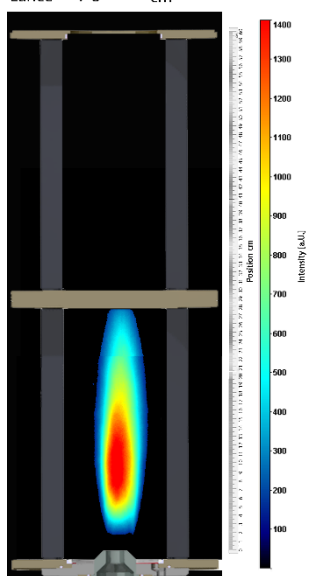
A. nozzle : Ø25.2 Semi-conical
 F. nozzle : DIVA
 v : 100 m/s
 T : 465 °C
 λ : 1.7
 P_{TH} : 40 kW
 LOH : 15 mm
 COM : 88 mm
 FL : 261 mm
 Lance : 8 cm



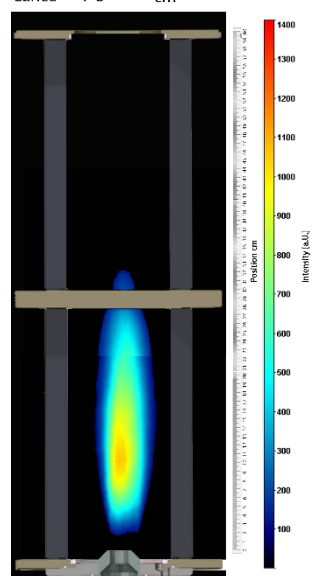
A. nozzle : Ø25.2 Semi-conical
 F. nozzle : DIVA
 v : 100 m/s
 T : 465 °C
 λ : 1.8
 P_{TH} : 38 kW
 LOH : 16 mm
 COM : 89 mm
 FL : 261 mm
 Lance : 8 cm



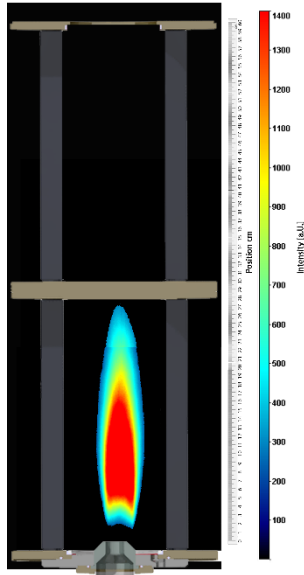
A. nozzle : Ø25.2 Semi-conical
 F. nozzle : DIVA
 v : 100 m/s
 T : 465 °C
 λ : 1.9
 P_{TH} : 36 kW
 LOH : 18 mm
 COM : 103 mm
 FL : 259 mm
 Lance : 8 cm



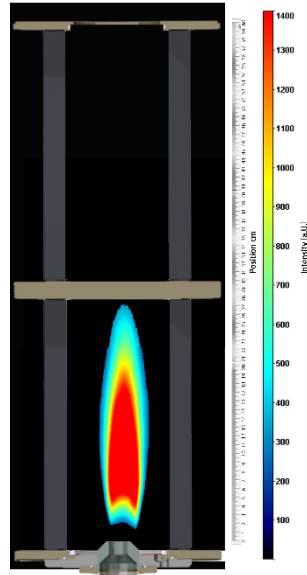
A. nozzle : Ø25.2 Semi-conical
 F. nozzle : DIVA
 v : 100 m/s
 T : 465 °C
 λ : 2
 P_{TH} : 34 kW
 LOH : 16 mm
 COM : 117 mm
 FL : 307 mm
 Lance : 8 cm



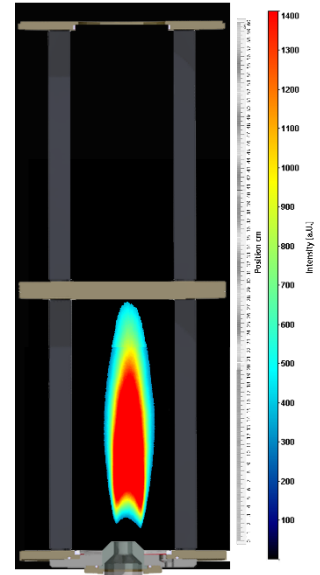
A. nozzle : Ø25.2 Semi-conical
 F. nozzle : DIVA
 v : 80 m/s
 T : 465 °C
 λ : 1.6
 P_{TH} : 34 kW
 LOH : 14 mm
 COM : 85 mm
 FL : 258 mm
 Lance : 8 cm



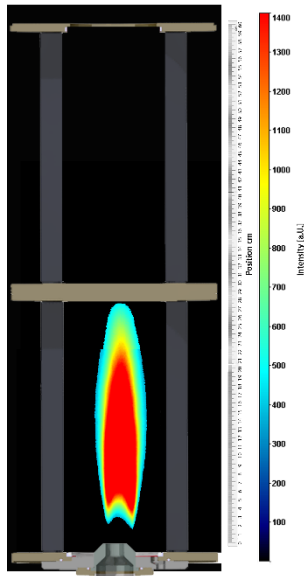
A. nozzle : Ø25.2 Semi-conical
 F. nozzle : DIVA
 v : 80 m/s
 T : 465 °C
 λ : 1.5
 P_{TH} : 36 kW
 LOH : 14 mm
 COM : 90 mm
 FL : 260 mm
 Lance : 8 cm



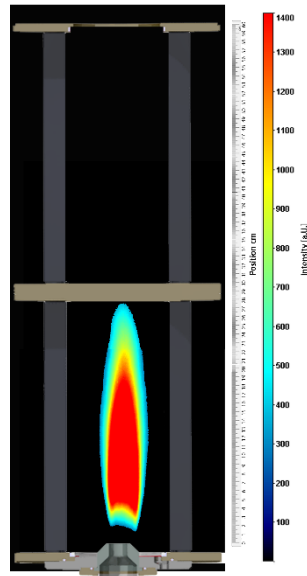
A. nozzle : Ø25.2 Semi-conical
 F. nozzle : DIVA
 v : 80 m/s
 T : 465 °C
 λ : 1.4
 P_{TH} : 39 kW
 LOH : 15 mm
 COM : 104 mm
 FL : 260 mm
 Lance : 8 cm



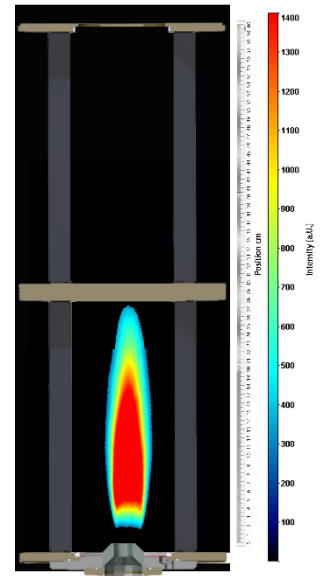
A. nozzle : Ø25.2 Semi-conical
 F. nozzle : DIVA
 v : 80 m/s
 T : 465 °C
 λ : 1.3
 P_{TH} : 42 kW
 LOH : 16 mm
 COM : 113 mm
 FL : 260 mm
 Lance : 8 cm



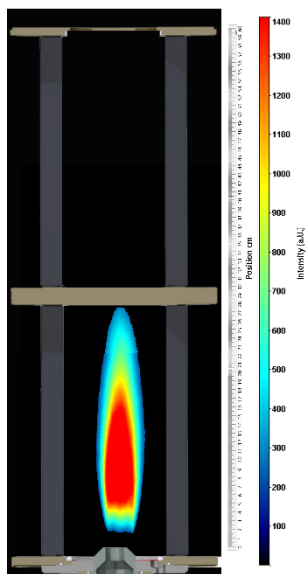
A. nozzle : Ø25.2 Semi-conical
 F. nozzle : DIVA
 v : 90 m/s
 T : 465 °C
 λ : 1.5
 P_{TH} : 41 kW
 LOH : 13 mm
 COM : 90 mm
 FL : 263 mm
 Lance : 8 cm



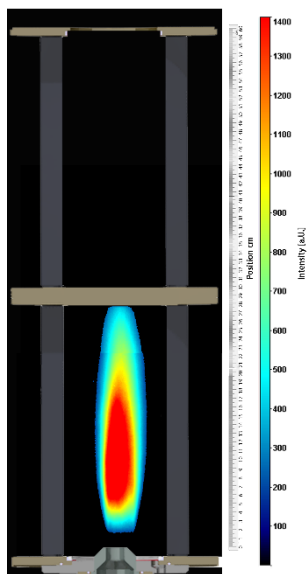
A. nozzle : Ø25.2 Semi-conical
 F. nozzle : DIVA
 v : 90 m/s
 T : 465 °C
 λ : 1.6
 P_{TH} : 38 kW
 LOH : 16 mm
 COM : 96 mm
 FL : 258 mm
 Lance : 8 cm



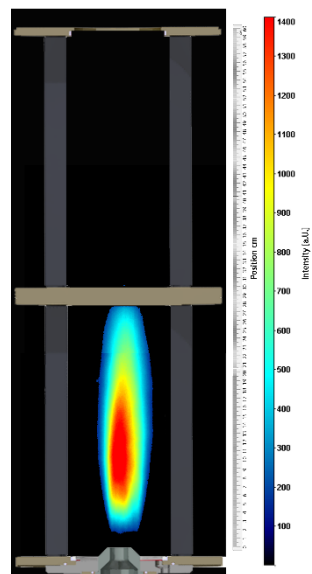
A. nozzle : Ø25.2 Semi-conical
 F. nozzle : DIVA
 v : 90 m/s
 T : 465 °C
 λ : 1.7
 P_{TH} : 36 kW
 LOH : 16 mm
 COM : 91 mm
 FL : 260 mm
 Lance : 8 cm



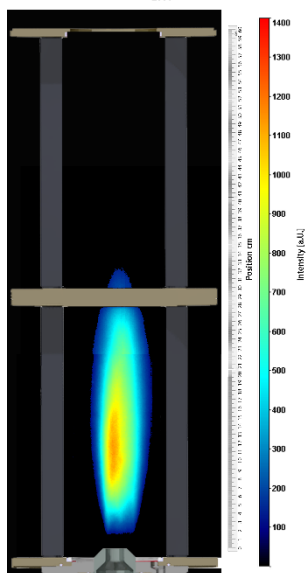
A. nozzle : Ø25.2 Semi-conical
 F. nozzle : DIVA
 v : 110 m/s
 T : 465 °C
 λ : 1.8
 P_{TH} : 41 kW
 LOH : 16 mm
 COM : 97 mm
 FL : 261 mm
 Lance : 8 cm



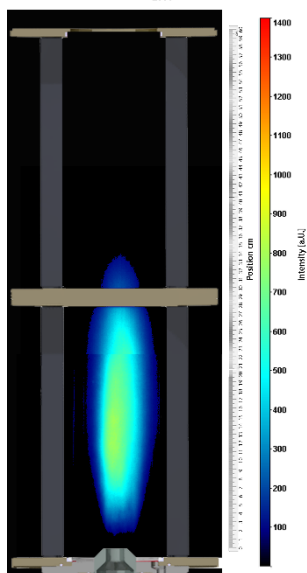
A. nozzle : Ø25.2 Semi-conical
 F. nozzle : DIVA
 v : 110 m/s
 T : 465 °C
 λ : 1.9
 P_{TH} : 39 kW
 LOH : 15 mm
 COM : 105 mm
 FL : 287 mm
 Lance : 8 cm



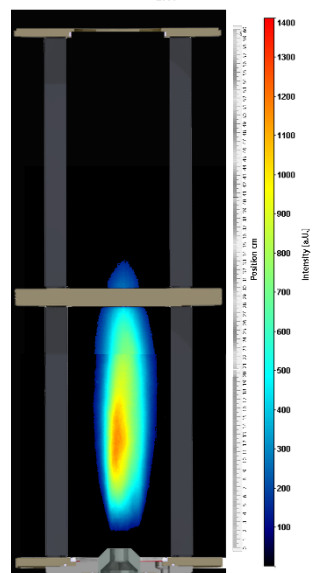
A. nozzle : Ø25.2 Semi-conical
 F. nozzle : DIVA
 v : 110 m/s
 T : 465 °C
 λ : 2
 P_{TH} : 37 kW
 LOH : 16 mm
 COM : 123 mm
 FL : 308 mm
 Lance : 8 cm



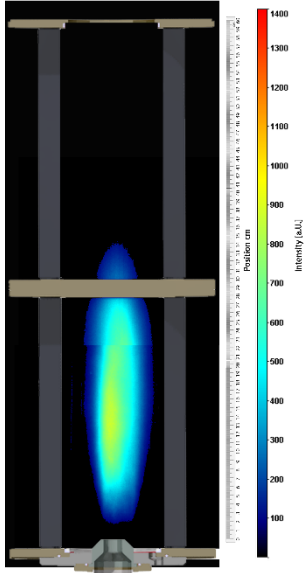
A. nozzle : Ø25.2 Semi-conical
 F. nozzle : DIVA
 v : 110 m/s
 T : 465 °C
 λ : 2.1
 P_{TH} : 35 kW
 LOH : 14 mm
 COM : 150 mm
 FL : 326 mm
 Lance : 8 cm



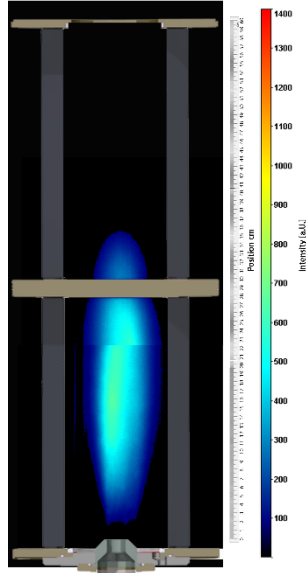
A. nozzle : Ø25.2 Semi-conical
 F. nozzle : DIVA
 v : 120 m/s
 T : 465 °C
 λ : 2
 P_{TH} : 40 kW
 LOH : 19 mm
 COM : 130 mm
 FL : 313 mm
 Lance : 8 cm



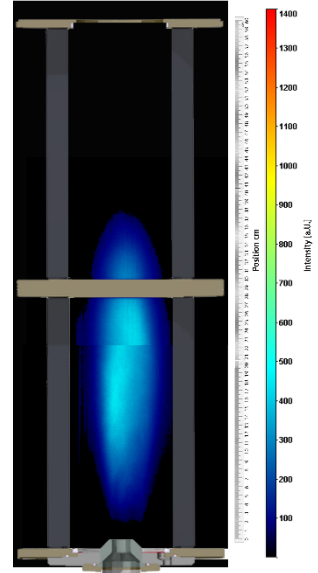
A. nozzle : Ø25.2 Semi-conical
 F. nozzle : DIVA
 v : 120 m/s
 T : 465 °C
 λ : 2.1
 P_{TH} : 38 kW
 LOH : 17 mm
 COM : 151 mm
 FL : 325 mm
 Lance : 8 cm



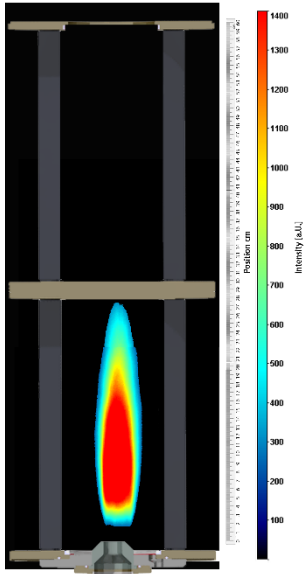
A. nozzle : Ø25.2 Semi-conical
 F. nozzle : DIVA
 v : 120 m/s
 T : 465 °C
 λ : 2.2
 P_{TH} : 37 kW
 LOH : 15 mm
 COM : 163 mm
 FL : 341 mm
 Lance : 8 cm



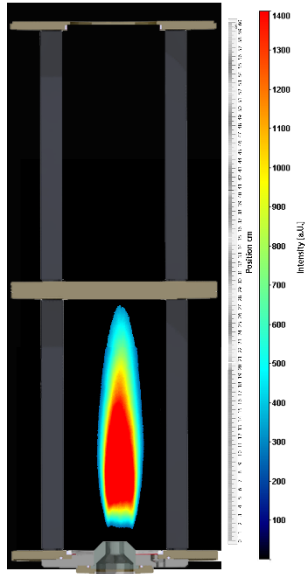
A. nozzle : Ø25.2 Semi-conical
 F. nozzle : DIVA
 v : 120 m/s
 T : 465 °C
 λ : 2.3
 P_{TH} : 35 kW
 LOH : 19 mm
 COM : 189 mm
 FL : 360 mm
 Lance : 8 cm



A. nozzle : Ø25.2 Semi-conical
 F. nozzle : DIVA
 v : 100 m/s
 T : 500 °C
 λ : 1.7
 P_{TH} : 38 kW
 LOH : 17 mm
 COM : 89 mm
 FL : 258 mm
 Lance : 8 cm

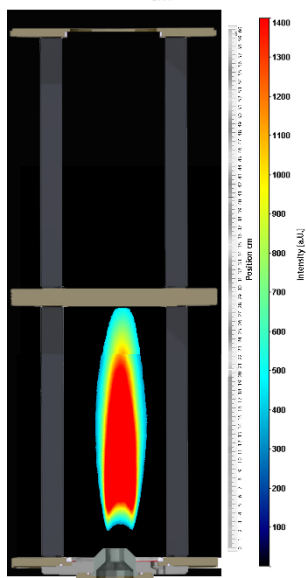


A. nozzle : Ø25.2 Semi-conical
 F. nozzle : DIVA
 v : 100 m/s
 T : 530 °C
 λ : 1.7
 P_{TH} : 36 kW
 LOH : 14 mm
 COM : 79 mm
 FL : 257 mm
 Lance : 8 cm

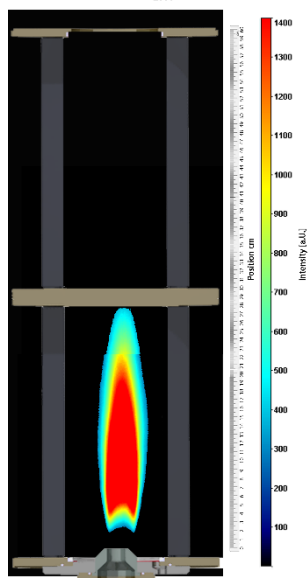


St45°H

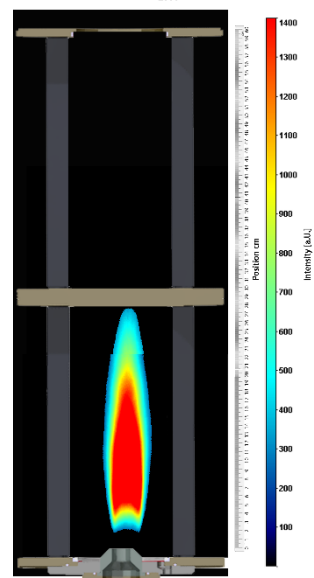
A. nozzle : Ø25.2 Semi-conical
 F. nozzle : Steinen 1.00 45°H
 v : 80 m/s
 T : 465 °C
 λ : 1.3
 P_{TH} : 41.663 kW
 LOH : 20 mm
 COM : 107 mm
 FL : 257 mm
 Lance : 8 cm



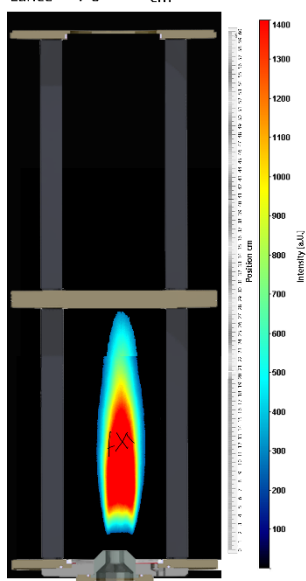
A. nozzle : Ø25.2 Semi-conical
 F. nozzle : Steinen 1.00 45°H
 v : 80 m/s
 T : 465 °C
 λ : 1.4
 P_{TH} : 38.317 kW
 LOH : 18 mm
 COM : 98 mm
 FL : 258 mm
 Lance : 8 cm



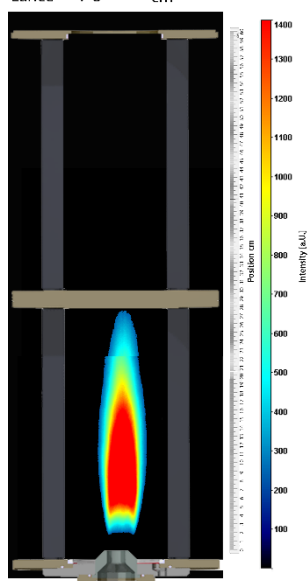
A. nozzle : Ø25.2 Semi-conical
 F. nozzle : Steinen 1.00 45°H
 v : 80 m/s
 T : 465 °C
 λ : 1.5
 P_{TH} : 36.04 kW
 LOH : 18 mm
 COM : 94 mm
 FL : 258 mm
 Lance : 8 cm



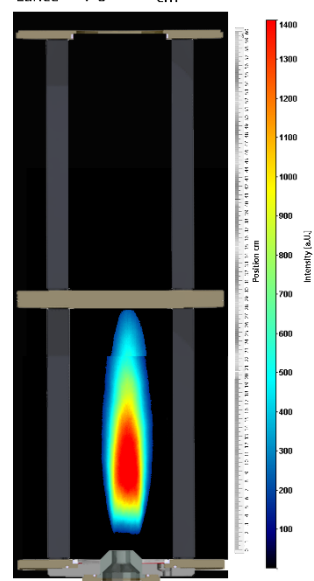
A. nozzle : Ø25.2 Semi-conical
 F. nozzle : Steinen 1.00 45°H
 v : 80 m/s
 T : 465 °C
 λ : 1.6
 P_{TH} : 33.81 kW
 LOH : 18 mm
 COM : 87 mm
 FL : 258 mm
 Lance : 8 cm



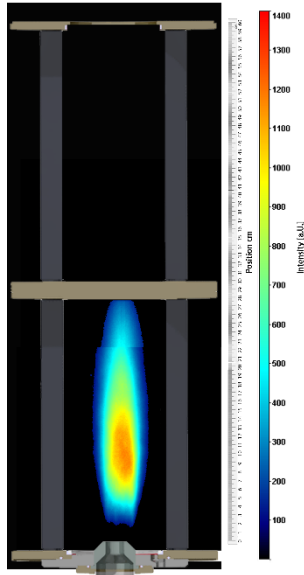
A. nozzle : Ø25.2 Semi-conical
 F. nozzle : Steinen 1.00 45°H
 v : 80 m/s
 T : 465 °C
 λ : 1.7
 P_{TH} : 31.859 kW
 LOH : 18 mm
 COM : 87 mm
 FL : 258 mm
 Lance : 8 cm



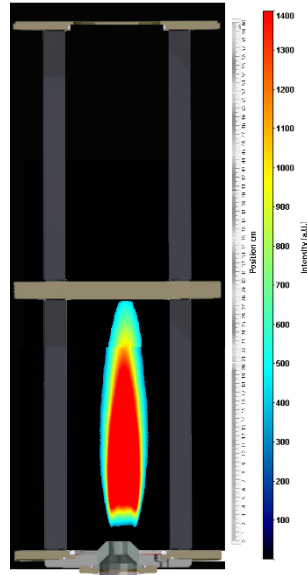
A. nozzle : Ø25.2 Semi-conical
 F. nozzle : Steinen 1.00 45°H
 v : 80 m/s
 T : 465 °C
 λ : 1.8
 P_{TH} : 29.27 kW
 LOH : 18 mm
 COM : 92 mm
 FL : 259 mm
 Lance : 8 cm



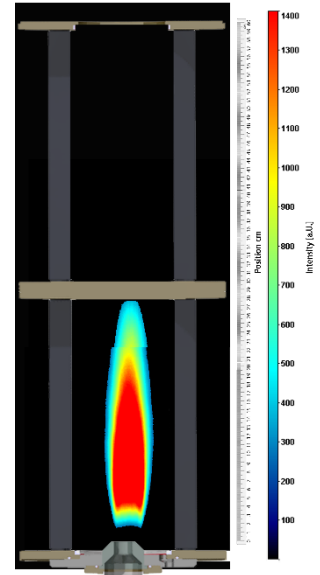
A. nozzle : Ø25.2 Semi-conical
 F. nozzle : Steinen 1.00 45°H
 v : 80 m/s
 T : 465 °C
 λ : 1.9
 P_{TH} : 28.421 kW
 LOH : 16 mm
 COM : 102 mm
 FL : 261 mm
 Lance : 8 cm



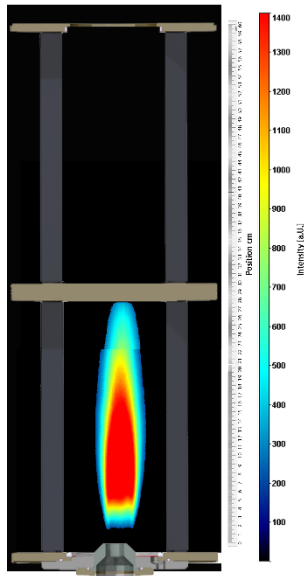
A. nozzle : Ø25.2 Semi-conical
 F. nozzle : Steinen 1.00 45°H
 v : 100 m/s
 T : 465 °C
 λ : 1.5
 P_{TH} : 41.791 kW
 LOH : 16 mm
 COM : 85 mm
 FL : 261 mm
 Lance : 8 cm



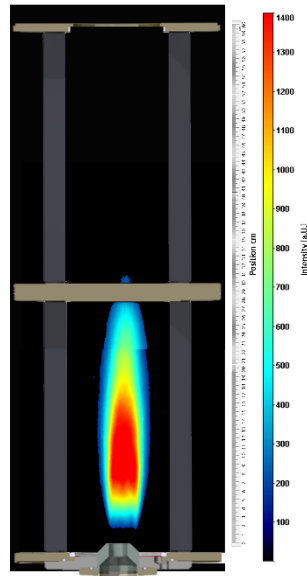
A. nozzle : Ø25.2 Semi-conical
 F. nozzle : Steinen 1.00 45°H
 v : 100 m/s
 T : 465 °C
 λ : 1.6
 P_{TH} : 42.586 kW
 LOH : 15 mm
 COM : 85 mm
 FL : 261 mm
 Lance : 8 cm



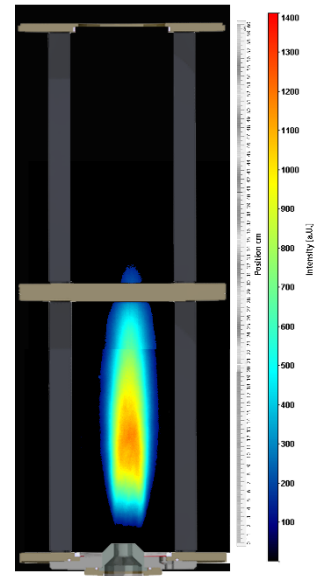
A. nozzle : Ø25.2 Semi-conical
 F. nozzle : Steinen 1.00 45°H
 v : 100 m/s
 T : 465 °C
 λ : 1.7
 P_{TH} : 40.08 kW
 LOH : 16 mm
 COM : 94 mm
 FL : 209 mm
 Lance : 8 cm



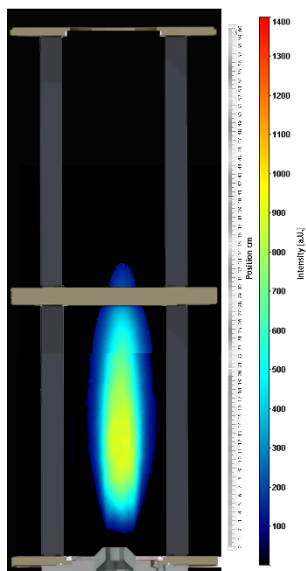
A. nozzle : Ø25.2 Semi-conical
 F. nozzle : Steinen 1.00 45°H
 v : 100 m/s
 T : 465 °C
 λ : 1.8
 P_{TH} : 37.343 kW
 LOH : 15 mm
 COM : 92 mm
 FL : 294 mm
 Lance : 8 cm



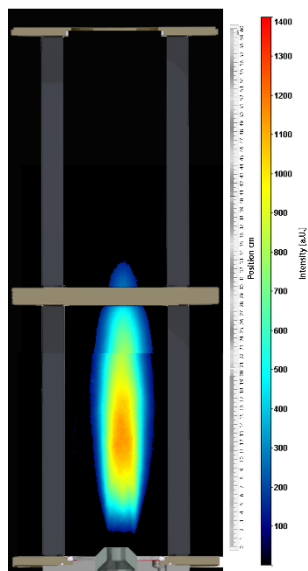
A. nozzle : Ø25.2 Semi-conical
 F. nozzle : Steinen 1.00 45°H
 v : 100 m/s
 T : 465 °C
 λ : 1.9
 P_{TH} : 35.86 kW
 LOH : 18 mm
 COM : 116 mm
 FL : 303 mm
 Lance : 8 cm



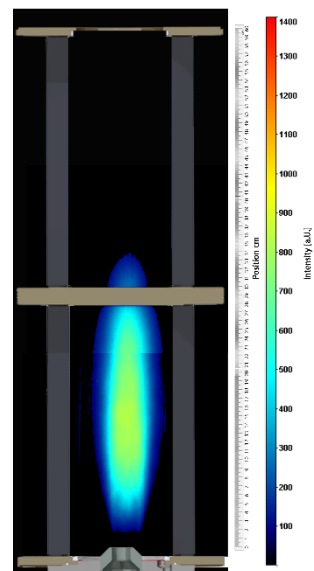
A. nozzle : Ø25.2 Semi-conical
 F. nozzle : Steinen 1.00 45°H
 v : 100 m/s
 T : 465 °C
 λ : 2
 P_{TH} : 34.0469 kW
 LOH : 16 mm
 COM : 123 mm
 FL : 313 mm
 Lance : 8 cm



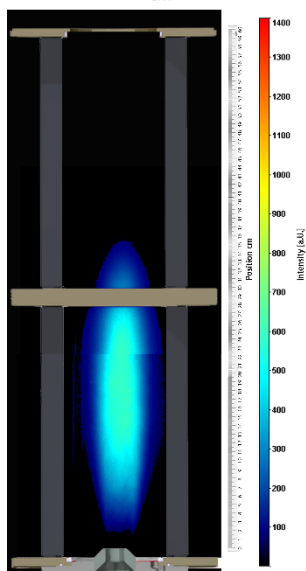
A. nozzle : Ø25.2 Semi-conical
 F. nozzle : Steinen 1.00 45°H
 v : 120 m/s
 T : 465 °C
 λ : 2
 P_{TH} : 40.44 kW
 LOH : 15 mm
 COM : 124 mm
 FL : 315 mm
 Lance : 8 cm



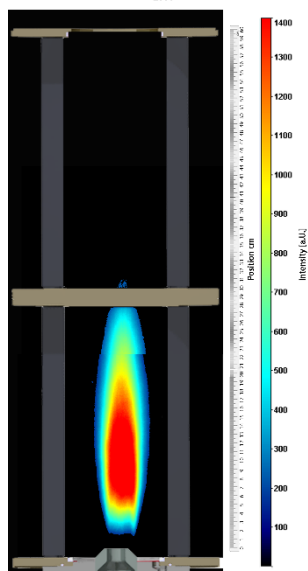
A. nozzle : Ø25.2 Semi-conical
 F. nozzle : Steinen 1.00 45°H
 v : 120 m/s
 T : 465 °C
 λ : 2.1
 P_{TH} : 38.473 kW
 LOH : 16 mm
 COM : 149 mm
 FL : 324 mm
 Lance : 8 cm



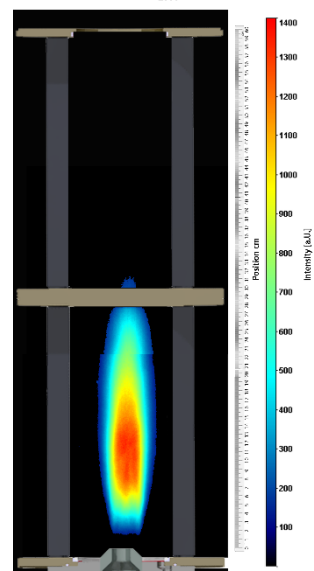
A. nozzle : Ø25.2 Semi-conical
 F. nozzle : Steinen 1.00 45°H
 v : 120 m/s
 T : 465 °C
 λ : 2.2
 P_{TH} : 36.704 kW
 LOH : 15 mm
 COM : 184 mm
 FL : 341 mm
 Lance : 8 cm



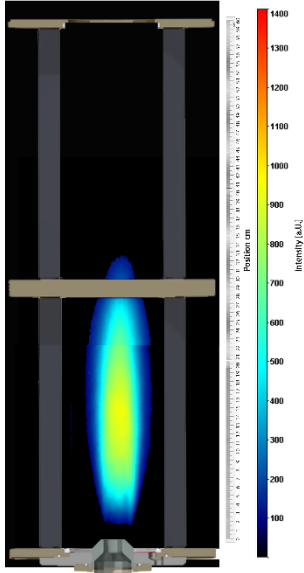
A. nozzle : Ø25.2 Semi-conical
 F. nozzle : Steinen 1.00 45°H
 v : 110 m/s
 T : 465 °C
 λ : 1.8
 P_{TH} : 41 kW
 LOH : 14 mm
 COM : 107 mm
 FL : 295 mm
 Lance : 8 cm



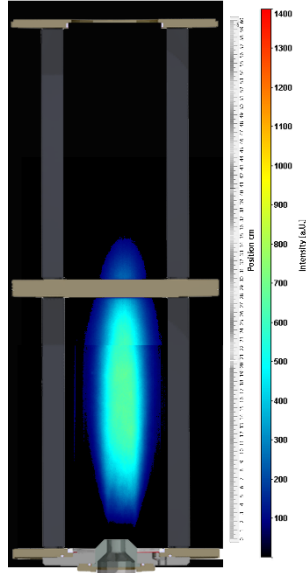
A. nozzle : Ø25.2 Semi-conical
 F. nozzle : Steinen 1.00 45°H
 v : 110 m/s
 T : 465 °C
 λ : 1.9
 P_{TH} : 39.0811 kW
 LOH : 15 mm
 COM : 122 mm
 FL : 300 mm
 Lance : 8 cm



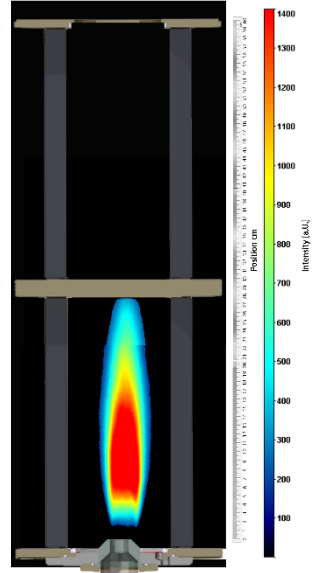
A. nozzle : Ø25.2 Semi-conical
 F. nozzle : Steinen 1.00 45°H
 v : 110 m/s
 T : 465 °C
 λ : 2
 P_{TH} : 37.025 kW
 LOH : 15 mm
 COM : 147 mm
 FL : 312 mm
 Lance : 8 cm



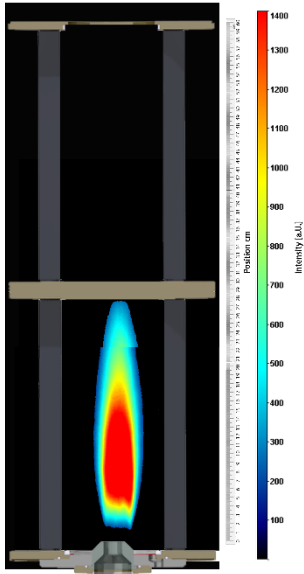
A. nozzle : Ø25.2 Semi-conical
 F. nozzle : Steinen 1.00 45°H
 v : 110 m/s
 T : 465 °C
 λ : 2.1
 P_{TH} : 35.359 kW
 LOH : 13 mm
 COM : 153 mm
 FL : 335 mm
 Lance : 8 cm



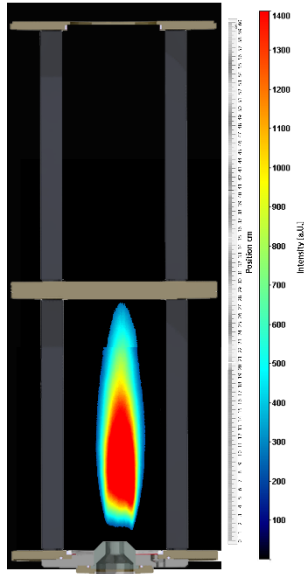
A. nozzle : Ø25.2 Semi-conical
 F. nozzle : Steinen 1.00 45°H
 v : 100 m/s
 T : 465 °C
 λ : 1.75
 P_{TH} : 38.317 kW
 LOH : 13 mm
 COM : 91 mm
 FL : 263 mm
 Lance : 8 cm



A. nozzle : Ø25.2 Semi-conical
 F. nozzle : Steinen 1.00 45°H
 v : 100 m/s
 T : 505 °C
 λ : 1.75
 P_{TH} : 36.517 kW
 LOH : 13 mm
 COM : 88 mm
 FL : 263 mm
 Lance : 8 cm

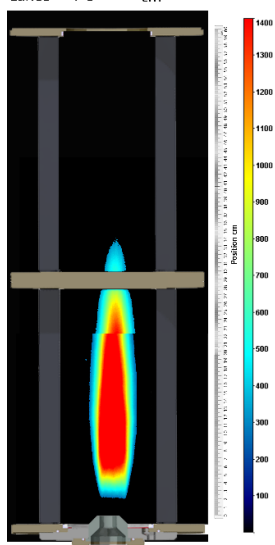


A. nozzle : Ø25.2 Semi-conical
 F. nozzle : Steinen 1.00 45°H
 v : 100 m/s
 T : 520 °C
 λ : 1.75
 P_{TH} : 35.967 kW
 LOH : 13 mm
 COM : 87 mm
 FL : 262 mm
 Lance : 8 cm

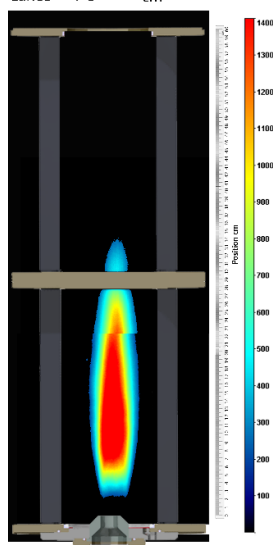


St30°S

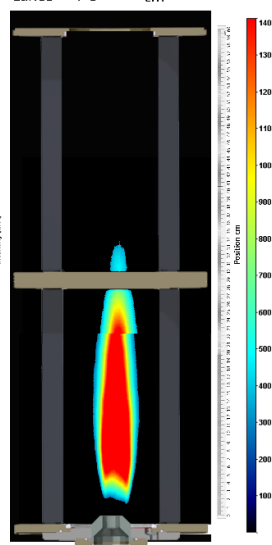
A. nozzle : Ø25.2 Semi-conical
 F. nozzle : Steinen 1.00 30°S
 v : 100 m/s
 T : 465 °C
 λ : 1.5
 P_{TH} : 44.607 kW
 LOH : 20 mm
 COM : 114 mm
 FL : 319 mm
 Lance : 8 cm



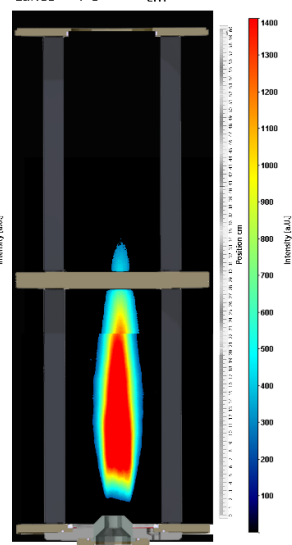
A. nozzle : Ø25.2 Semi-conical
 F. nozzle : Steinen 1.00 30°S
 v : 100 m/s
 T : 465 °C
 λ : 1.6
 P_{TH} : 41.752 kW
 LOH : 21 mm
 COM : 113 mm
 FL : 320 mm
 Lance : 8 cm



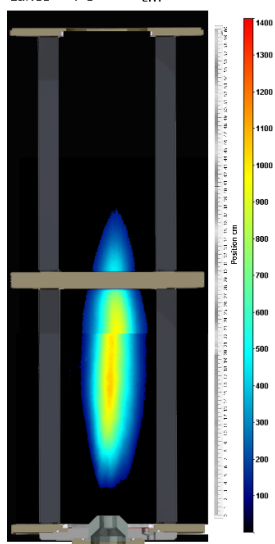
A. nozzle : Ø25.2 Semi-conical
 F. nozzle : Steinen 1.00 30°S
 v : 80 m/s
 T : 465 °C
 λ : 1.3
 P_{TH} : 40.95 kW
 LOH : 14 mm
 COM : 101 mm
 FL : 321 mm
 Lance : 8 cm



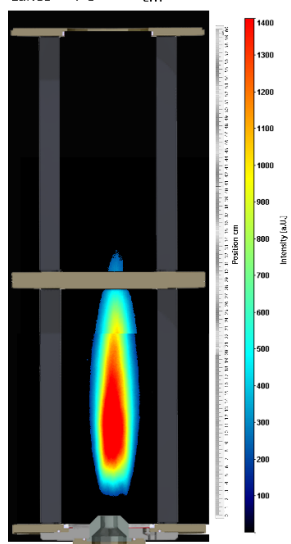
A. nozzle : Ø25.2 Semi-conical
 F. nozzle : Steinen 1.00 30°S
 v : 80 m/s
 T : 465 °C
 λ : 1.4
 P_{TH} : 38.452 kW
 LOH : 16 mm
 COM : 108 mm
 FL : 320 mm
 Lance : 8 cm



A. nozzle : Ø25.2 Semi-conical
 F. nozzle : Steinen 1.00 30°S
 v : 120 m/s
 T : 465 °C
 λ : 2
 P_{TH} : 40.716 kW
 LOH : 32 mm
 COM : 172 mm
 FL : 346 mm
 Lance : 8 cm

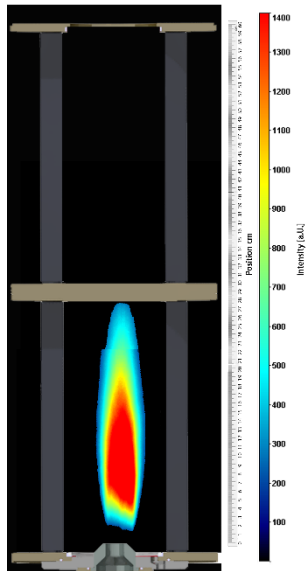


A. nozzle : Ø25.2 Semi-conical
 F. nozzle : Steinen 1.00 30°S
 v : 100 m/s
 T : 510 °C
 λ : 1.7
 P_{TH} : 37.426 kW
 LOH : 23 mm
 COM : 117 mm
 FL : 300 mm
 Lance : 8 cm

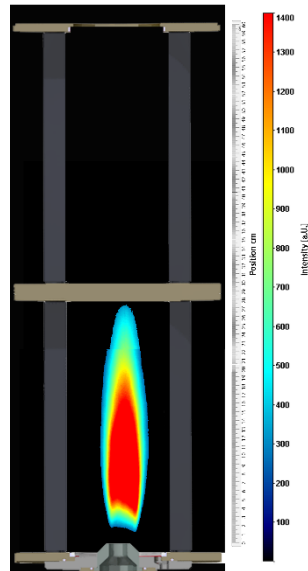


Dan45°H

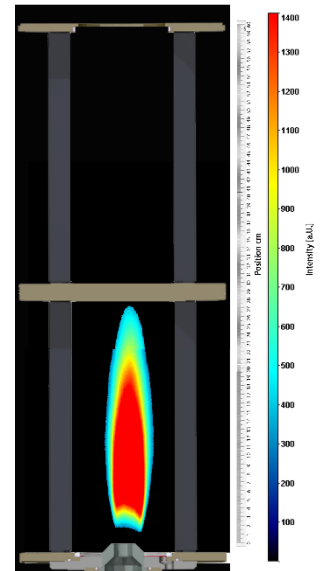
A. nozzle : Ø25.2 Semi-conical
 F. nozzle : Danfoss 1.00 45°H
 v : 100 m/s
 T : 465 °C
 λ : 1.8
 P_{TH} : 37.414 kW
 LOH : 14 mm
 COM : 83 mm
 FL : 263 mm
 Lance : 8 cm



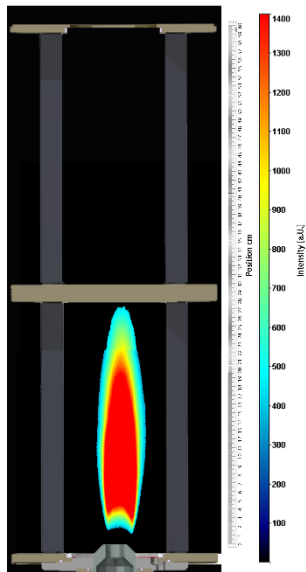
A. nozzle : Ø25.2 Semi-conical
 F. nozzle : Danfoss 1.00 45°H
 v : 100 m/s
 T : 465 °C
 λ : 1.7
 P_{TH} : 37.349 kW
 LOH : 13 mm
 COM : 81 mm
 FL : 262 mm
 Lance : 8 cm



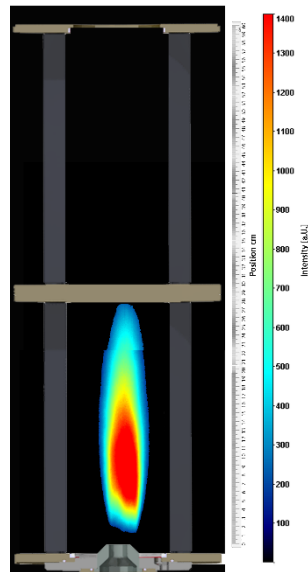
A. nozzle : Ø25.2 Semi-conical
 F. nozzle : Danfoss 1.00 45°H
 v : 100 m/s
 T : 465 °C
 λ : 1.6
 P_{TH} : 39.344 kW
 LOH : 13 mm
 COM : 82 mm
 FL : 261 mm
 Lance : 8 cm



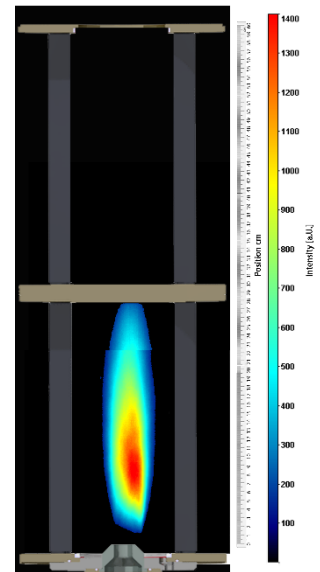
A. nozzle : Ø25.2 Semi-conical
 F. nozzle : Danfoss 1.00 45°H
 v : 100 m/s
 T : 465 °C
 λ : 1.5
 P_{TH} : 45.252 kW
 LOH : 12 mm
 COM : 93 mm
 FL : 263 mm
 Lance : 8 cm



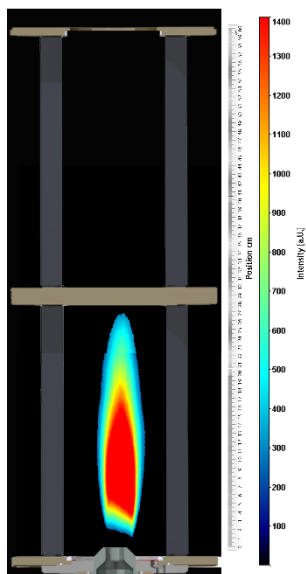
A. nozzle : Ø25.2 Semi-conical
 F. nozzle : Danfoss 1.00 45°H
 v : 100 m/s
 T : 465 °C
 λ : 1.9
 P_{TH} : 35.45 kW
 LOH : 13 mm
 COM : 87 mm
 FL : 263 mm
 Lance : 8 cm



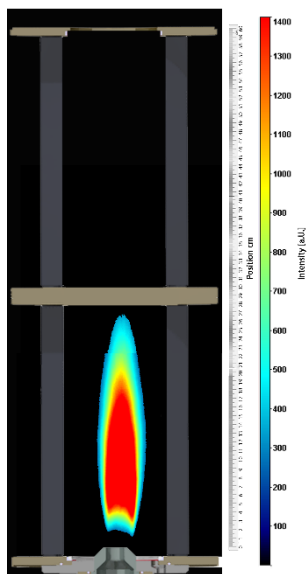
A. nozzle : Ø25.2 Semi-conical
 F. nozzle : Danfoss 1.00 45°H
 v : 100 m/s
 T : 465 °C
 λ : 2
 P_{TH} : 33.659 kW
 LOH : 13 mm
 COM : 92 mm
 FL : 264 mm
 Lance : 8 cm



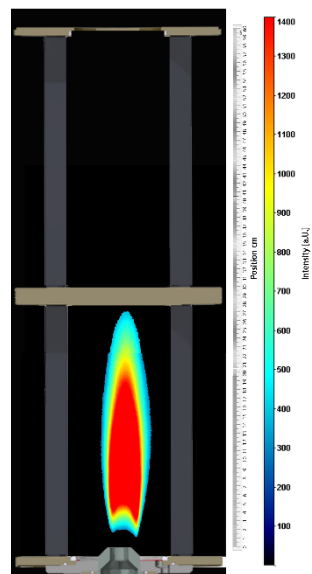
A. nozzle : Ø25.2 Semi-conical
 F. nozzle : Danfoss 1.00 45°H
 v : 90 m/s
 T : 465 °C
 λ : 1.7
 P_{TH} : 35.538 kW
 LOH : 12 mm
 COM : 84 mm
 FL : 258 mm
 Lance : 8 cm



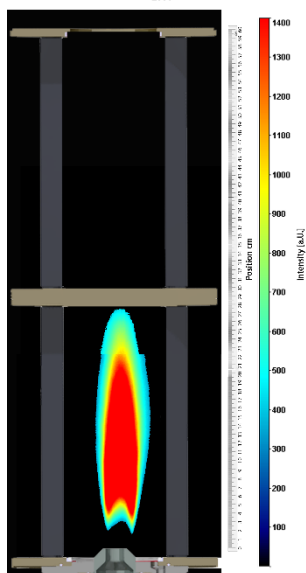
A. nozzle : Ø25.2 Semi-conical
 F. nozzle : Danfoss 1.00 45°H
 v : 90 m/s
 T : 465 °C
 λ : 1.6
 P_{TH} : 37.836 kW
 LOH : 12 mm
 COM : 82 mm
 FL : 256 mm
 Lance : 8 cm



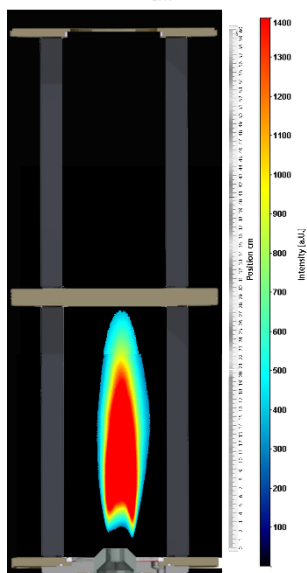
A. nozzle : Ø25.2 Semi-conical
 F. nozzle : Danfoss 1.00 45°H
 v : 90 m/s
 T : 465 °C
 λ : 1.5
 P_{TH} : 40.309 kW
 LOH : 11 mm
 COM : 90 mm
 FL : 261 mm
 Lance : 8 cm



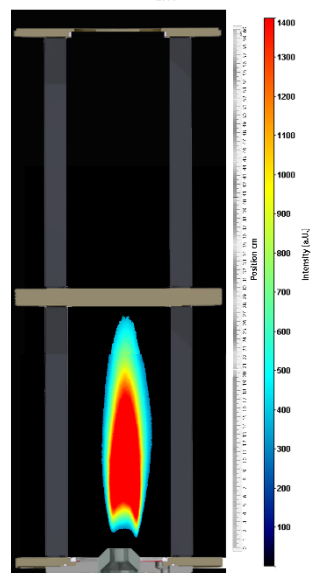
A. nozzle : Ø25.2 Semi-conical
 F. nozzle : Danfoss 1.00 45°H
 v : 80 m/s
 T : 465 °C
 λ : 1.3
 P_{TH} : 41.348 kW
 LOH : 16 mm
 COM : 104 mm
 FL : 259 mm
 Lance : 8 cm



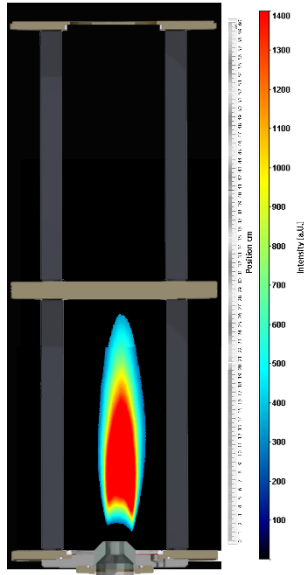
A. nozzle : Ø25.2 Semi-conical
 F. nozzle : Danfoss 1.00 45°H
 v : 80 m/s
 T : 465 °C
 λ : 1.4
 P_{TH} : 38.338 kW
 LOH : 12 mm
 COM : 97 mm
 FL : 262 mm
 Lance : 8 cm



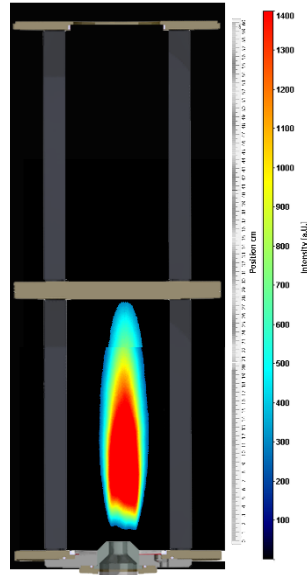
A. nozzle : Ø25.2 Semi-conical
 F. nozzle : Danfoss 1.00 45°H
 v : 80 m/s
 T : 465 °C
 λ : 1.5
 P_{TH} : 35.719 kW
 LOH : 12 mm
 COM : 88 mm
 FL : 254 mm
 Lance : 8 cm



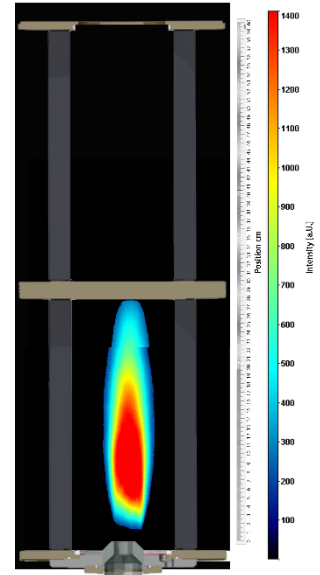
A. nozzle : Ø25.2 Semi-conical
 F. nozzle : Danfoss 1.00 45°H
 v : 80 m/s
 T : 465 °C
 λ : 1.6
 P_{TH} : 33.596 kW
 LOH : 11 mm
 COM : 89 mm
 FL : 251 mm
 Lance : 8 cm



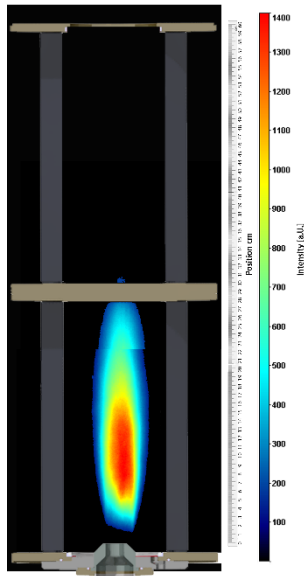
A. nozzle : Ø25.2 Semi-conical
 F. nozzle : Danfoss 1.00 45°H
 v : 110 m/s
 T : 465 °C
 λ : 1.8
 P_{TH} : 41.312 kW
 LOH : 13 mm
 COM : 81 mm
 FL : 263 mm
 Lance : 8 cm



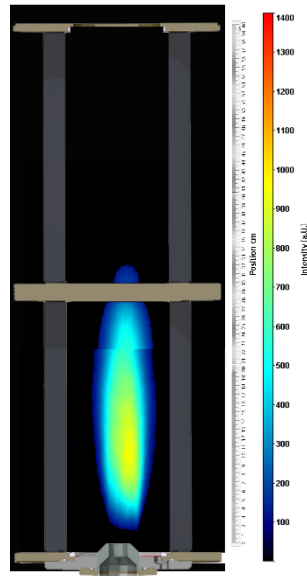
A. nozzle : Ø25.2 Semi-conical
 F. nozzle : Danfoss 1.00 45°H
 v : 110 m/s
 T : 465 °C
 λ : 1.9
 P_{TH} : 39 kW
 LOH : 13 mm
 COM : 88 mm
 FL : 264 mm
 Lance : 8 cm



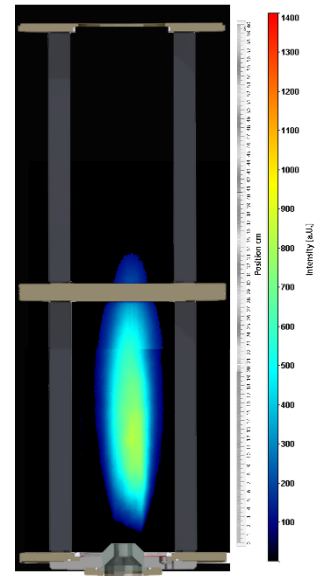
A. nozzle : Ø25.2 Semi-conical
 F. nozzle : Danfoss 1.00 45°H
 v : 110 m/s
 T : 465 °C
 λ : 2
 P_{TH} : 37.05 kW
 LOH : 12 mm
 COM : 108 mm
 FL : 294 mm
 Lance : 8 cm



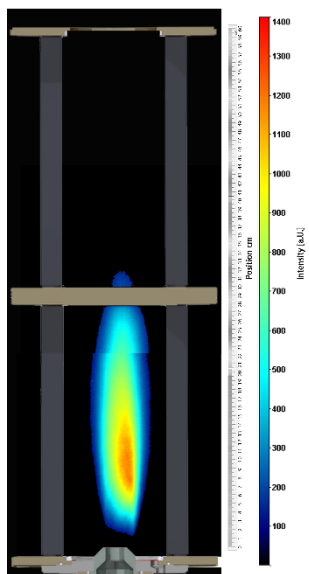
A. nozzle : Ø25.2 Semi-conical
 F. nozzle : Danfoss 1.00 45°H
 v : 110 m/s
 T : 465 °C
 λ : 2.1
 P_{TH} : 35.913 kW
 LOH : 14 mm
 COM : 124 mm
 FL : 308 mm
 Lance : 8 cm



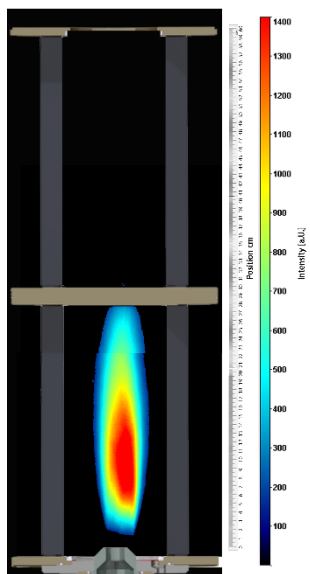
A. nozzle : Ø25.2 Semi-conical
 F. nozzle : Danfoss 1.00 45°H
 v : 120 m/s
 T : 465 °C
 λ : 2.2
 P_{TH} : 35.262 kW
 LOH : 12 mm
 COM : 140 mm
 FL : 325 mm
 Lance : 8 cm



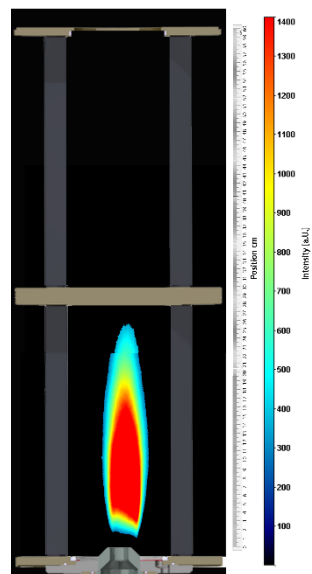
A. nozzle : Ø25.2 Semi-conical
 F. nozzle : Danfoss 1.00 45°H
 v : 120 m/s
 T : 465 °C
 λ : 2.1
 P_{TH} : 36.764 kW
 LOH : 13 mm
 COM : 122 mm
 FL : 306 mm
 Lance : 8 cm



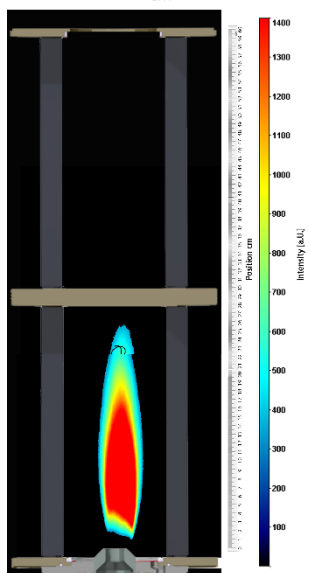
A. nozzle : Ø25.2 Semi-conical
 F. nozzle : Danfoss 1.00 45°H
 v : 120 m/s
 T : 465 °C
 λ : 2
 P_{TH} : 40.402 kW
 LOH : 13 mm
 COM : 100 mm
 FL : 290 mm
 Lance : 8 cm



A. nozzle : Ø25.2 Semi-conical
 F. nozzle : Danfoss 1.00 45°H
 v : 100 m/s
 T : 500 °C
 λ : 1.7
 P_{TH} : 37.688 kW
 LOH : 11 mm
 COM : 76 mm
 FL : 247 mm
 Lance : 8 cm



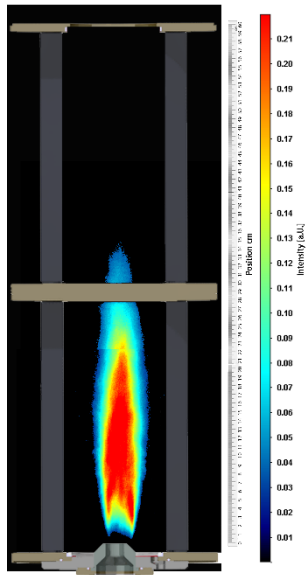
A. nozzle : Ø25.2 Semi-conical
 F. nozzle : Danfoss 1.00 45°H
 v : 100 m/s
 T : 530 °C
 λ : 1.7
 P_{TH} : 36.613 kW
 LOH : 10 mm
 COM : 76 mm
 FL : 248 mm
 Lance : 8 cm



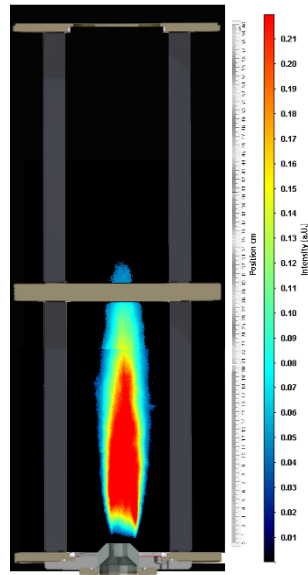
APPENDIX 3 RMS OH*-CL IMAGES

DIVA

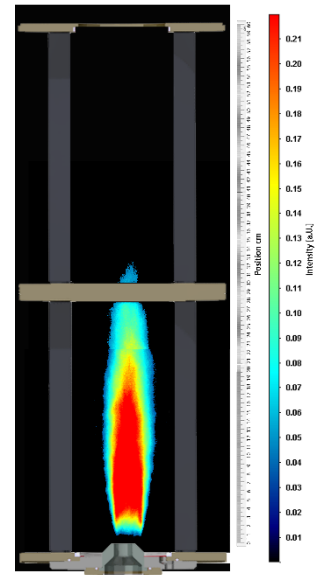
A. nozzle : Ø25.2 Semi-conical
 F. nozzle : DIVA
 v : 100 m/s
 T : 465 °C
 λ : 1.5
 P_{TH} : 45 kW
 LOH : 10 mm
 COM : 76 mm
 FL : 267 mm
 Lance : 8 cm



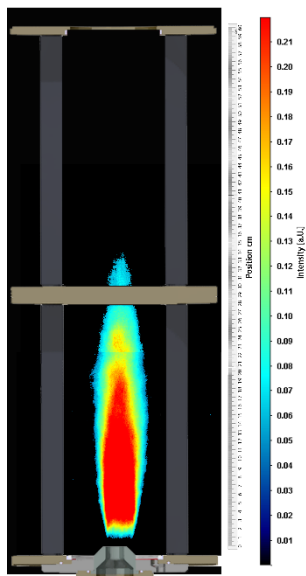
A. nozzle : Ø25.2 Semi-conical
 F. nozzle : DIVA
 v : 100 m/s
 T : 465 °C
 λ : 1.6
 P_{TH} : 42 kW
 LOH : 12 mm
 COM : 89 mm
 FL : 265 mm
 Lance : 8 cm



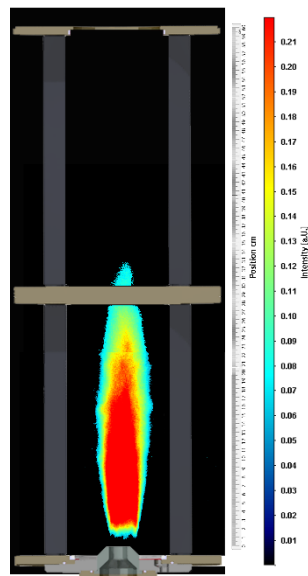
A. nozzle : Ø25.2 Semi-conical
 F. nozzle : DIVA
 v : 100 m/s
 T : 465 °C
 λ : 1.7
 P_{TH} : 40 kW
 LOH : 15 mm
 COM : 88 mm
 FL : 261 mm
 Lance : 8 cm



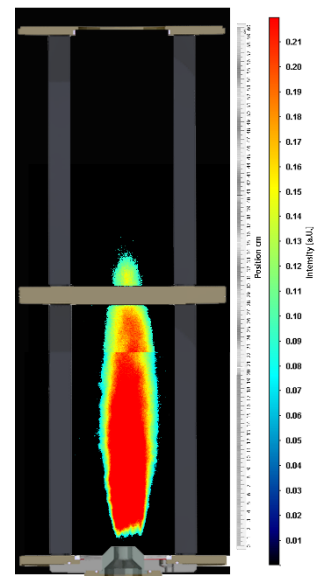
A. nozzle : Ø25.2 Semi-conical
 F. nozzle : DIVA
 v : 100 m/s
 T : 465 °C
 λ : 1.8
 P_{TH} : 38 kW
 LOH : 16 mm
 COM : 89 mm
 FL : 261 mm
 Lance : 8 cm



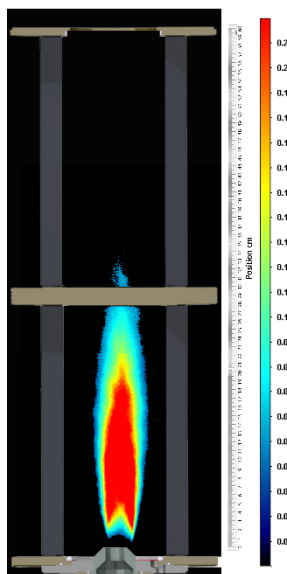
A. nozzle : Ø25.2 Semi-conical
 F. nozzle : DIVA
 v : 100 m/s
 T : 465 °C
 λ : 1.9
 P_{TH} : 36 kW
 LOH : 18 mm
 COM : 103 mm
 FL : 259 mm
 Lance : 8 cm



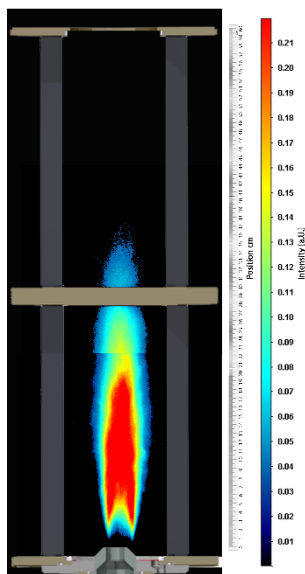
A. nozzle : Ø25.2 Semi-conical
 F. nozzle : DIVA
 v : 100 m/s
 T : 465 °C
 λ : 2
 P_{TH} : 34 kW
 LOH : 16 mm
 COM : 117 mm
 FL : 307 mm
 Lance : 8 cm



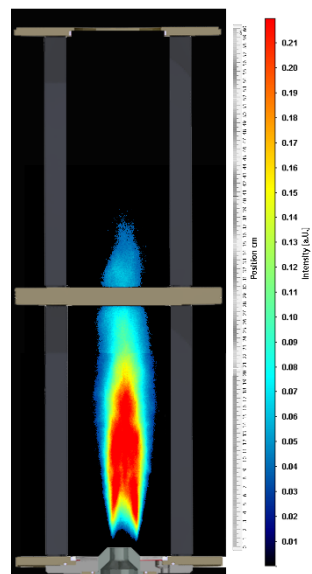
A. nozzle : Ø25.2 Semi-conical
 F. nozzle : DIVA
 v : 80 m/s
 T : 465 °C
 λ : 1.5
 P_{TH} : 36 kW
 LOH : 14 mm
 COM : 90 mm
 FL : 260 mm
 Lance : 8 cm



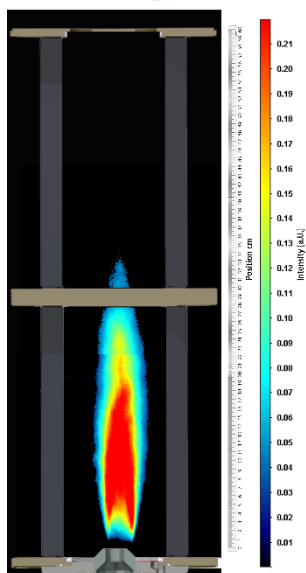
A. nozzle : Ø25.2 Semi-conical
 F. nozzle : DIVA
 v : 80 m/s
 T : 465 °C
 λ : 1.4
 P_{TH} : 39 kW
 LOH : 15 mm
 COM : 104 mm
 FL : 260 mm
 Lance : 8 cm



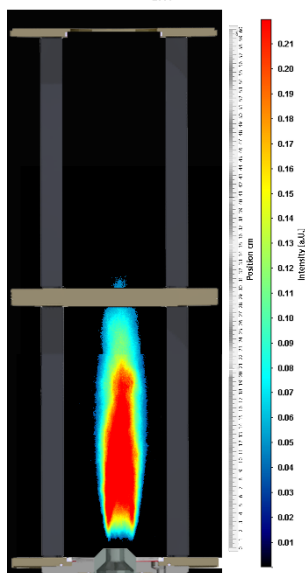
A. nozzle : Ø25.2 Semi-conical
 F. nozzle : DIVA
 v : 80 m/s
 T : 465 °C
 λ : 1.3
 P_{TH} : 42 kW
 LOH : 16 mm
 COM : 113 mm
 FL : 260 mm
 Lance : 8 cm



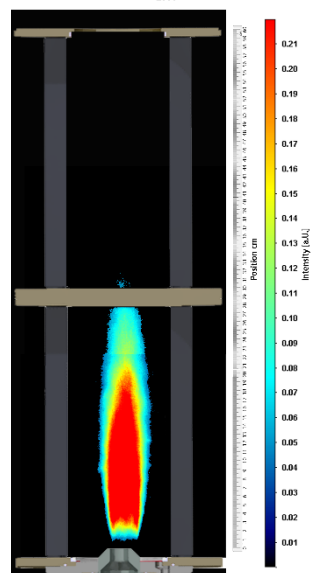
A. nozzle : Ø25.2 Semi-conical
 F. nozzle : DIVA
 v : 90 m/s
 T : 465 °C
 λ : 1.5
 P_{TH} : 41 kW
 LOH : 13 mm
 COM : 90 mm
 FL : 263 mm
 Lance : 8 cm



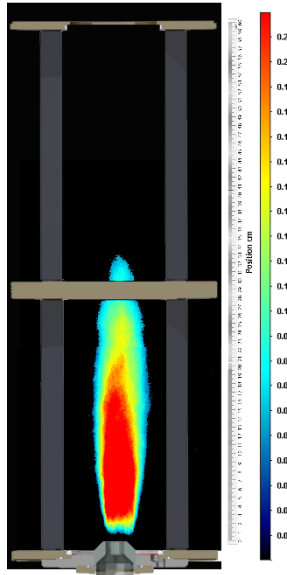
A. nozzle : Ø25.2 Semi-conical
 F. nozzle : DIVA
 v : 90 m/s
 T : 465 °C
 λ : 1.6
 P_{TH} : 38 kW
 LOH : 16 mm
 COM : 96 mm
 FL : 258 mm
 Lance : 8 cm



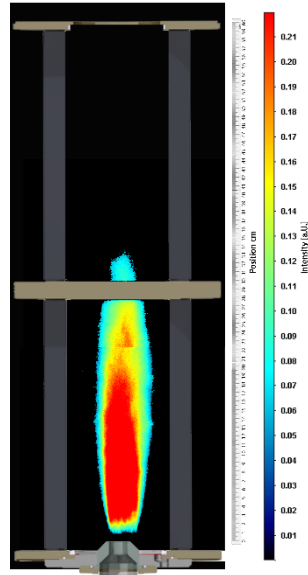
A. nozzle : Ø25.2 Semi-conical
 F. nozzle : DIVA
 v : 90 m/s
 T : 465 °C
 λ : 1.7
 P_{TH} : 36 kW
 LOH : 16 mm
 COM : 91 mm
 FL : 260 mm
 Lance : 8 cm



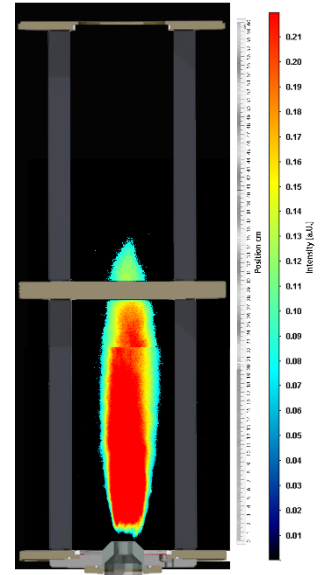
A. nozzle : Ø25.2 Semi-conical
 F. nozzle : DIVA
 v : 110 m/s
 T : 465 °C
 λ : 1.8
 P_{TH} : 41 kW
 LOH : 16 mm
 COM : 97 mm
 FL : 261 mm
 Lance : 8 cm



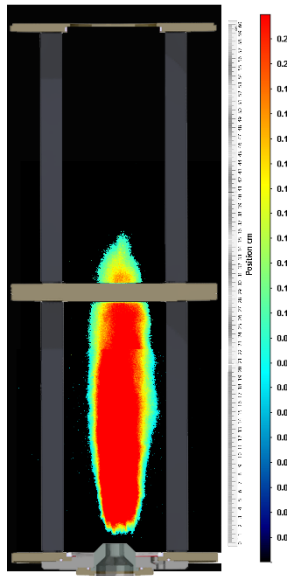
A. nozzle : Ø25.2 Semi-conical
 F. nozzle : DIVA
 v : 110 m/s
 T : 465 °C
 λ : 1.9
 P_{TH} : 39 kW
 LOH : 15 mm
 COM : 105 mm
 FL : 287 mm
 Lance : 8 cm



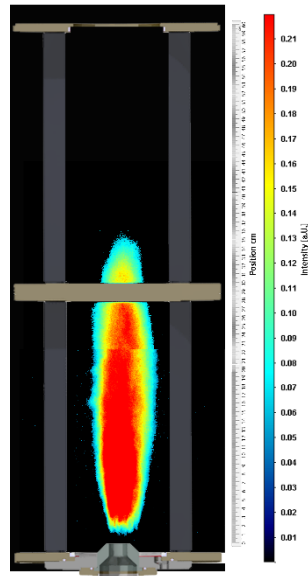
A. nozzle : Ø25.2 Semi-conical
 F. nozzle : DIVA
 v : 110 m/s
 T : 465 °C
 λ : 2
 P_{TH} : 37 kW
 LOH : 16 mm
 COM : 123 mm
 FL : 308 mm
 Lance : 8 cm



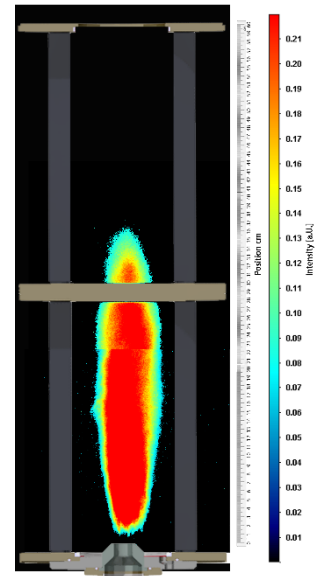
A. nozzle : Ø25.2 Semi-conical
 F. nozzle : DIVA
 v : 110 m/s
 T : 465 °C
 λ : 2.1
 P_{TH} : 35 kW
 LOH : 14 mm
 COM : 150 mm
 FL : 326 mm
 Lance : 8 cm



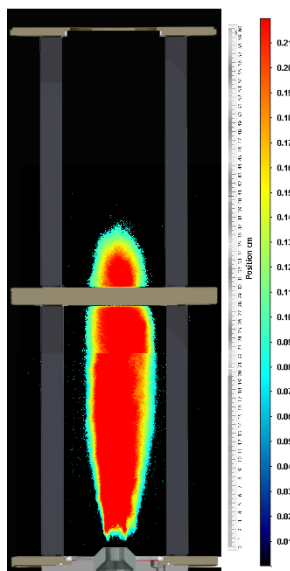
A. nozzle : Ø25.2 Semi-conical
 F. nozzle : DIVA
 v : 120 m/s
 T : 465 °C
 λ : 2
 P_{TH} : 40 kW
 LOH : 19 mm
 COM : 130 mm
 FL : 313 mm
 Lance : 8 cm



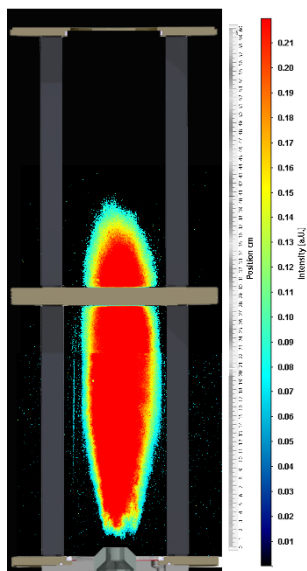
A. nozzle : Ø25.2 Semi-conical
 F. nozzle : DIVA
 v : 120 m/s
 T : 465 °C
 λ : 2.1
 P_{TH} : 38 kW
 LOH : 17 mm
 COM : 151 mm
 FL : 325 mm
 Lance : 8 cm



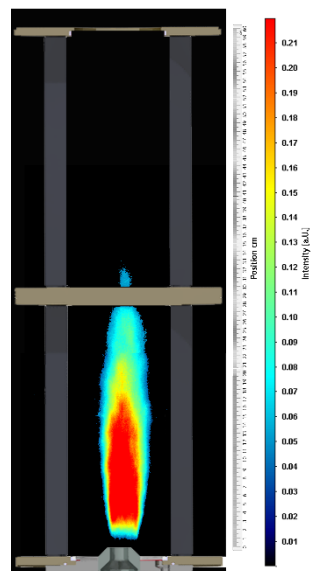
A. nozzle : Ø25.2 Semi-conical
 F. nozzle : DIVA
 v : 120 m/s
 T : 465 °C
 λ : 2.2
 P_{TH} : 37 kW
 LOH : 15 mm
 COM : 163 mm
 FL : 341 mm
 Lance : 8 cm



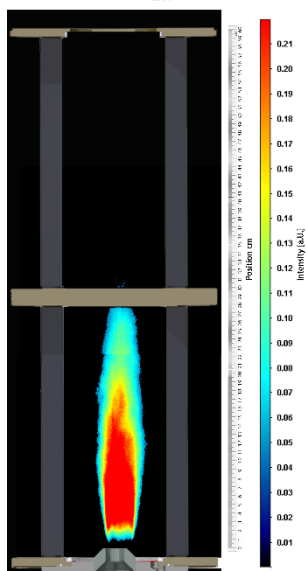
A. nozzle : Ø25.2 Semi-conical
 F. nozzle : DIVA
 v : 120 m/s
 T : 465 °C
 λ : 2.3
 P_{TH} : 35 kW
 LOH : 19 mm
 COM : 189 mm
 FL : 360 mm
 Lance : 8 cm



A. nozzle : Ø25.2 Semi-conical
 F. nozzle : DIVA
 v : 100 m/s
 T : 500 °C
 λ : 1.7
 P_{TH} : 38 kW
 LOH : 17 mm
 COM : 89 mm
 FL : 258 mm
 Lance : 8 cm

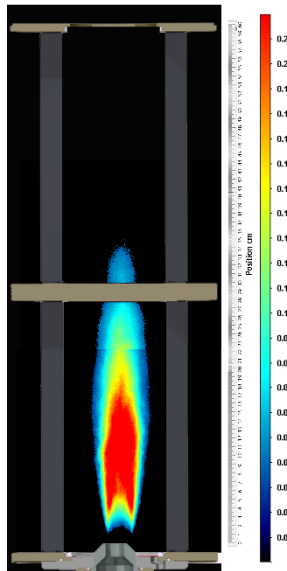


A. nozzle : Ø25.2 Semi-conical
 F. nozzle : DIVA
 v : 100 m/s
 T : 530 °C
 λ : 1.7
 P_{TH} : 36 kW
 LOH : 14 mm
 COM : 79 mm
 FL : 257 mm
 Lance : 8 cm

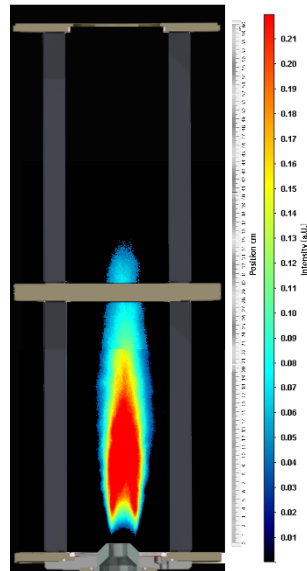


St45°H

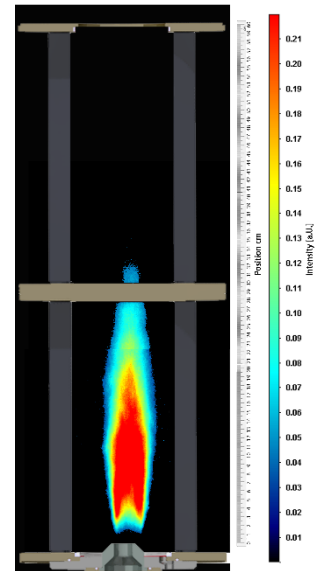
A. nozzle : Ø25.2 Semi-conical
 F. nozzle : Steinen 1.00 45°H
 v : 80 m/s
 T : 465 °C
 λ : 1.3
 P_{TH} : 41.663 kW
 LOH : 20 mm
 COM : 107 mm
 FL : 257 mm
 Lance : 8 cm



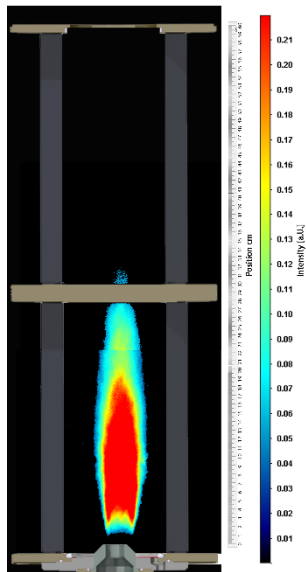
A. nozzle : Ø25.2 Semi-conical
 F. nozzle : Steinen 1.00 45°H
 v : 80 m/s
 T : 465 °C
 λ : 1.4
 P_{TH} : 38.317 kW
 LOH : 18 mm
 COM : 98 mm
 FL : 258 mm
 Lance : 8 cm



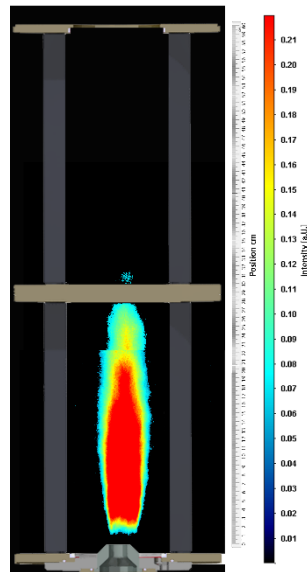
A. nozzle : Ø25.2 Semi-conical
 F. nozzle : Steinen 1.00 45°H
 v : 80 m/s
 T : 465 °C
 λ : 1.5
 P_{TH} : 36.04 kW
 LOH : 18 mm
 COM : 94 mm
 FL : 258 mm
 Lance : 8 cm



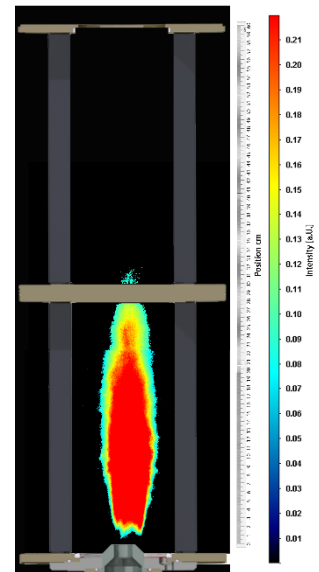
A. nozzle : Ø25.2 Semi-conical
 F. nozzle : Steinen 1.00 45°H
 v : 80 m/s
 T : 465 °C
 λ : 1.6
 P_{TH} : 33.81 kW
 LOH : 18 mm
 COM : 87 mm
 FL : 258 mm
 Lance : 8 cm



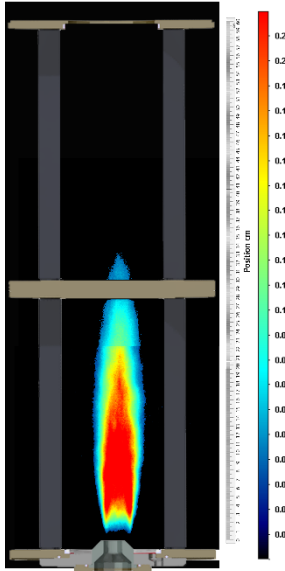
A. nozzle : Ø25.2 Semi-conical
 F. nozzle : Steinen 1.00 45°H
 v : 80 m/s
 T : 465 °C
 λ : 1.8
 P_{TH} : 29.27 kW
 LOH : 18 mm
 COM : 92 mm
 FL : 259 mm
 Lance : 8 cm



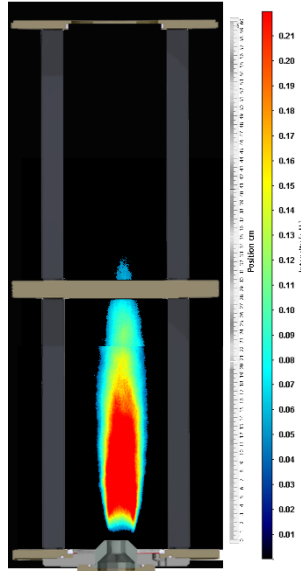
A. nozzle : Ø25.2 Semi-conical
 F. nozzle : Steinen 1.00 45°H
 v : 80 m/s
 T : 465 °C
 λ : 1.9
 P_{TH} : 28.421 kW
 LOH : 16 mm
 COM : 102 mm
 FL : 261 mm
 Lance : 8 cm



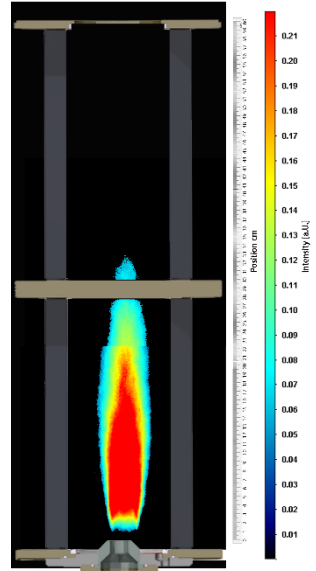
A. nozzle : Ø25.2 Semi-conical
 F. nozzle : Steinen 1.00 45°H
 v : 100 m/s
 T : 465 °C
 λ : 1.5
 P_{TH} : 41.791 kW
 LOH : 16 mm
 COM : 85 mm
 FL : 261 mm
 Lance : 8 cm



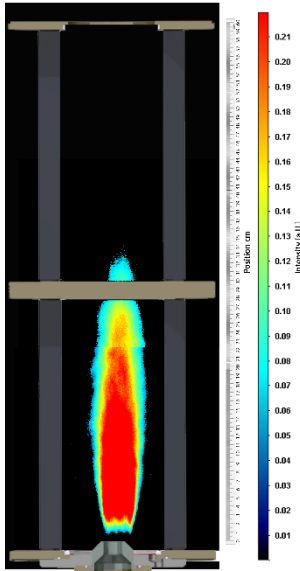
A. nozzle : Ø25.2 Semi-conical
 F. nozzle : Steinen 1.00 45°H
 v : 100 m/s
 T : 465 °C
 λ : 1.6
 P_{TH} : 42.586 kW
 LOH : 15 mm
 COM : 85 mm
 FL : 261 mm
 Lance : 8 cm



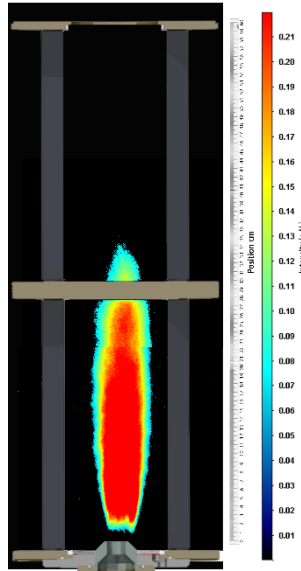
A. nozzle : Ø25.2 Semi-conical
 F. nozzle : Steinen 1.00 45°H
 v : 100 m/s
 T : 465 °C
 λ : 1.7
 P_{TH} : 40.08 kW
 LOH : 16 mm
 COM : 94 mm
 FL : 209 mm
 Lance : 8 cm



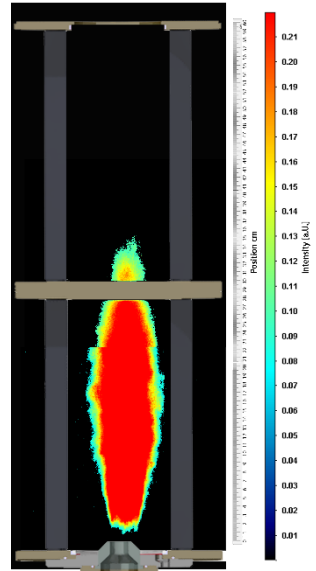
A. nozzle : Ø25.2 Semi-conical
 F. nozzle : Steinen 1.00 45°H
 v : 100 m/s
 T : 465 °C
 λ : 1.8
 P_{TH} : 37.343 kW
 LOH : 15 mm
 COM : 92 mm
 FL : 294 mm
 Lance : 8 cm



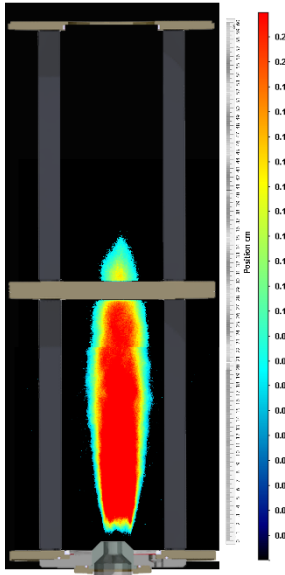
A. nozzle : Ø25.2 Semi-conical
 F. nozzle : Steinen 1.00 45°H
 v : 100 m/s
 T : 465 °C
 λ : 1.9
 P_{TH} : 35.86 kW
 LOH : 18 mm
 COM : 116 mm
 FL : 303 mm
 Lance : 8 cm



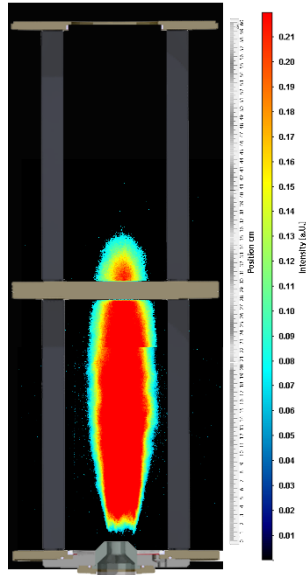
A. nozzle : Ø25.2 Semi-conical
 F. nozzle : Steinen 1.00 45°H
 v : 100 m/s
 T : 465 °C
 λ : 2
 P_{TH} : 34.0469 kW
 LOH : 16 mm
 COM : 123 mm
 FL : 313 mm
 Lance : 8 cm



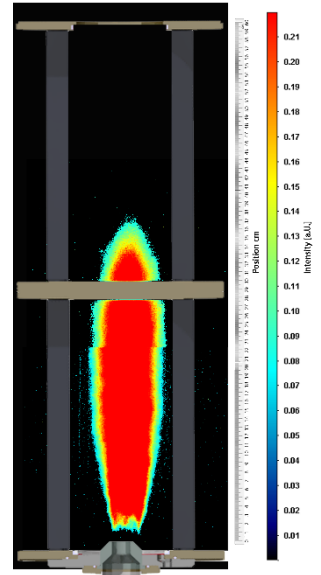
A. nozzle : Ø25.2 Semi-conical
 F. nozzle : Steinen 1.00 45°H
 v : 120 m/s
 T : 465 °C
 λ : 2
 P_{TH} : 40.44 kW
 LOH : 15 mm
 COM : 124 mm
 FL : 315 mm
 Lance : 8 cm



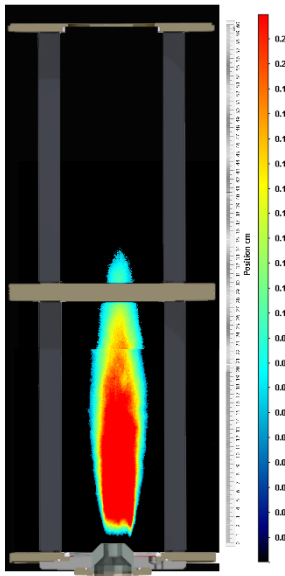
A. nozzle : Ø25.2 Semi-conical
 F. nozzle : Steinen 1.00 45°H
 v : 120 m/s
 T : 465 °C
 λ : 2.1
 P_{TH} : 38.473 kW
 LOH : 16 mm
 COM : 149 mm
 FL : 324 mm
 Lance : 8 cm



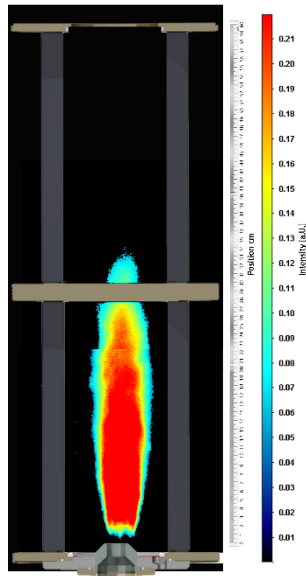
A. nozzle : Ø25.2 Semi-conical
 F. nozzle : Steinen 1.00 45°H
 v : 120 m/s
 T : 465 °C
 λ : 2.2
 P_{TH} : 36.704 kW
 LOH : 15 mm
 COM : 184 mm
 FL : 341 mm
 Lance : 8 cm



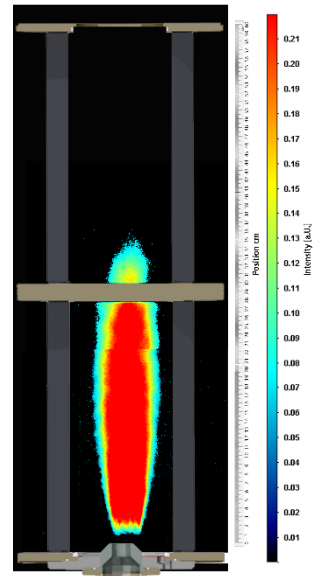
A. nozzle : Ø25.2 Semi-conical
 F. nozzle : Steinen 1.00 45°H
 v : 110 m/s
 T : 465 °C
 λ : 1.8
 P_{TH} : 41 kW
 LOH : 14 mm
 COM : 107 mm
 FL : 295 mm
 Lance : 8 cm



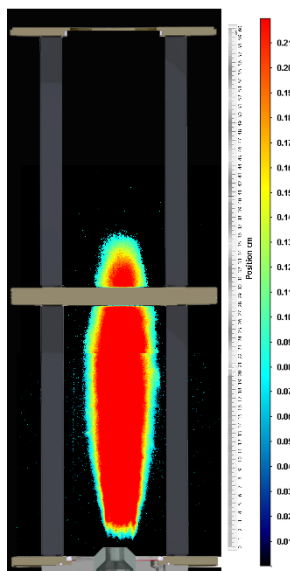
A. nozzle : Ø25.2 Semi-conical
 F. nozzle : Steinen 1.00 45°H
 v : 110 m/s
 T : 465 °C
 λ : 1.9
 P_{TH} : 39.0811 kW
 LOH : 15 mm
 COM : 122 mm
 FL : 300 mm
 Lance : 8 cm



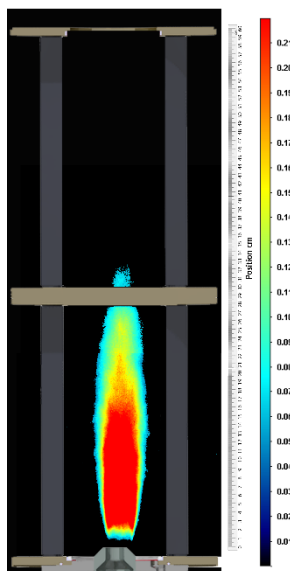
A. nozzle : Ø25.2 Semi-conical
 F. nozzle : Steinen 1.00 45°H
 v : 110 m/s
 T : 465 °C
 λ : 2
 P_{TH} : 37.025 kW
 LOH : 15 mm
 COM : 147 mm
 FL : 312 mm
 Lance : 8 cm



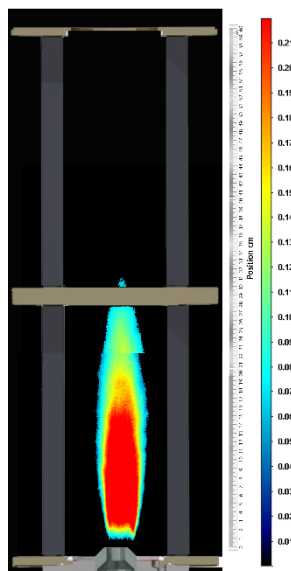
A. nozzle : Ø25.2 Semi-conical
 F. nozzle : Steinen 1.00 45°H
 v : 110 m/s
 T : 465 °C
 λ : 2.1
 P_{TH} : 35.359 kW
 LOH : 13 mm
 COM : 153 mm
 FL : 335 mm
 Lance : 8 cm



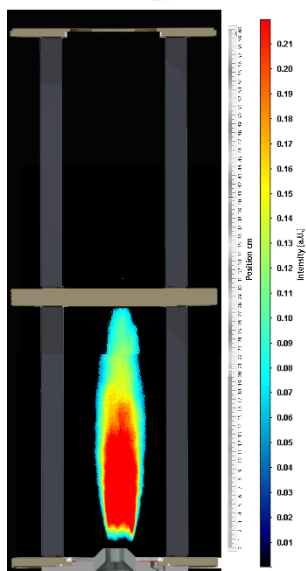
A. nozzle : Ø25.2 Semi-conical
 F. nozzle : Steinen 1.00 45°H
 v : 100 m/s
 T : 465 °C
 λ : 1.75
 P_{TH} : 38.317 kW
 LOH : 13 mm
 COM : 91 mm
 FL : 263 mm
 Lance : 8 cm



A. nozzle : Ø25.2 Semi-conical
 F. nozzle : Steinen 1.00 45°H
 v : 100 m/s
 T : 505 °C
 λ : 1.75
 P_{TH} : 36.517 kW
 LOH : 13 mm
 COM : 88 mm
 FL : 263 mm
 Lance : 8 cm

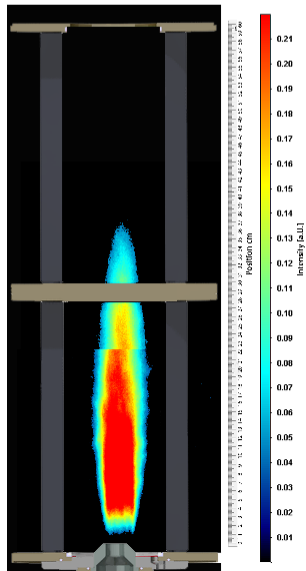


A. nozzle : Ø25.2 Semi-conical
 F. nozzle : Steinen 1.00 45°H
 v : 100 m/s
 T : 520 °C
 λ : 1.75
 P_{TH} : 35.967 kW
 LOH : 13 mm
 COM : 87 mm
 FL : 262 mm
 Lance : 8 cm

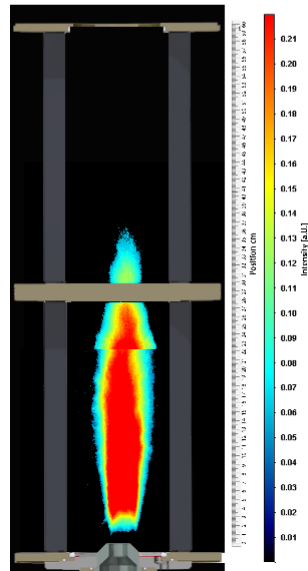


St30°S

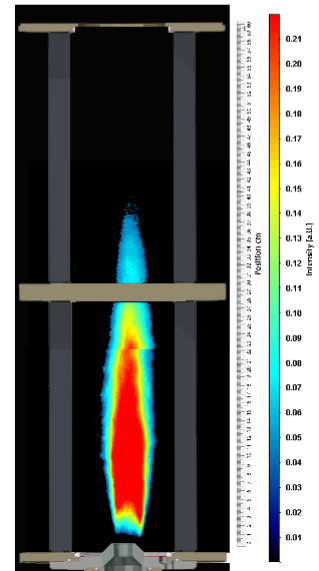
A. nozzle : Ø25.2 Semi-conical
 F. nozzle : Steinen 1.00 30°S
 v : 100 m/s
 T : 465 °C
 λ : 1.5
 P_{III} : 44.607 kW
 LOH : 20 mm
 COM : 114 mm
 FL : 319 mm
 Lance : 8 cm



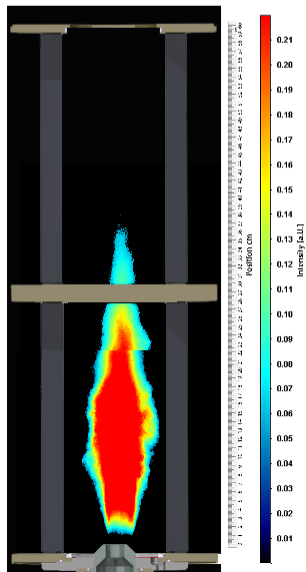
A. nozzle : Ø25.2 Semi-conical
 F. nozzle : Steinen 1.00 30°S
 v : 100 m/s
 T : 465 °C
 λ : 1.6
 P_{III} : 41.752 kW
 LOH : 21 mm
 COM : 113 mm
 FL : 320 mm
 Lance : 8 cm



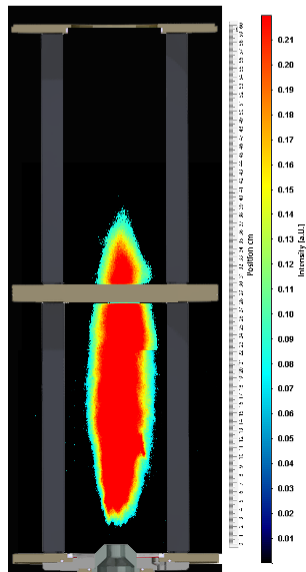
A. nozzle : Ø25.2 Semi-conical
 F. nozzle : Steinen 1.00 30°S
 v : 80 m/s
 T : 465 °C
 λ : 1.3
 P_{III} : 40.95 kW
 LOH : 14 mm
 COM : 101 mm
 FL : 321 mm
 Lance : 8 cm



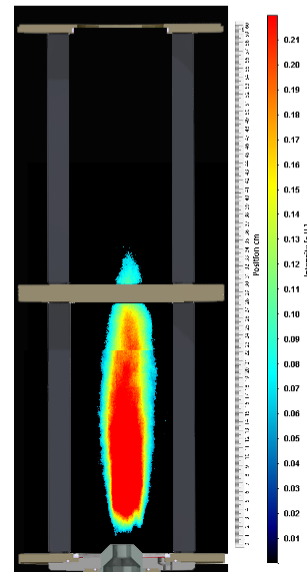
A. nozzle : Ø25.2 Semi-conical
 F. nozzle : Steinen 1.00 30°S
 v : 80 m/s
 T : 465 °C
 λ : 1.4
 P_{III} : 38.452 kW
 LOH : 16 mm
 COM : 108 mm
 FL : 320 mm
 Lance : 8 cm



A. nozzle : Ø25.2 Semi-conical
 F. nozzle : Steinen 1.00 30°S
 v : 120 m/s
 T : 465 °C
 λ : 2
 P_{III} : 40.716 kW
 LOH : 32 mm
 COM : 172 mm
 FL : 346 mm
 Lance : 8 cm

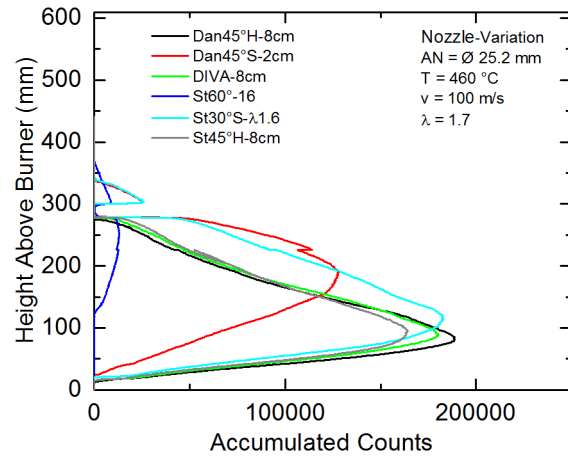
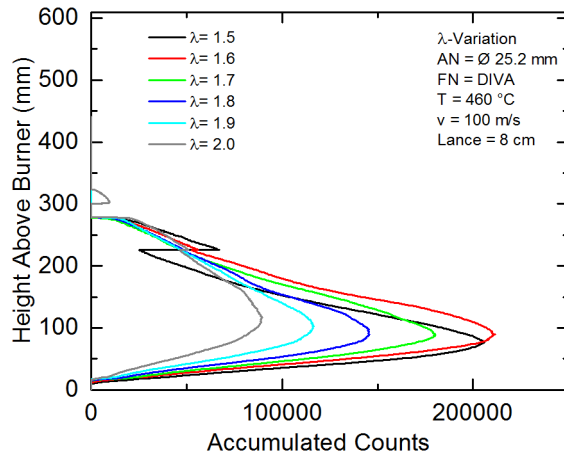


A. nozzle : Ø25.2 Semi-conical
 F. nozzle : Steinen 1.00 30°S
 v : 100 m/s
 T : 510 °C
 λ : 1.7
 P_{III} : 37.426 kW
 LOH : 23 mm
 COM : 117 mm
 FL : 300 mm
 Lance : 8 cm

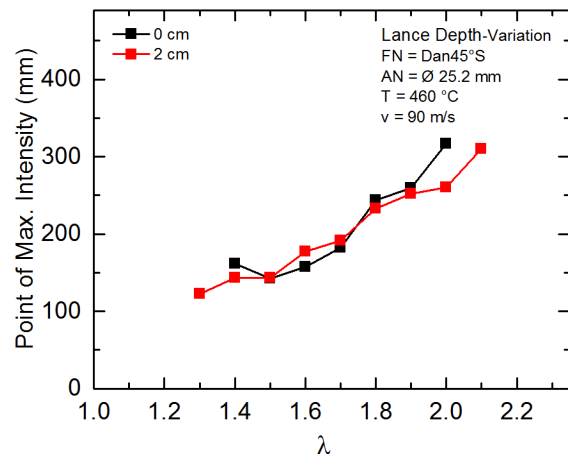
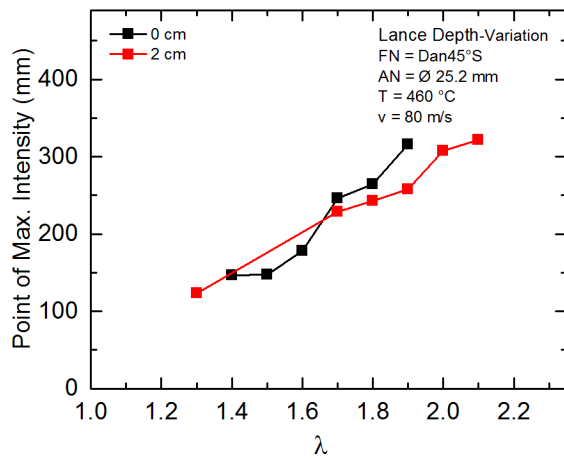


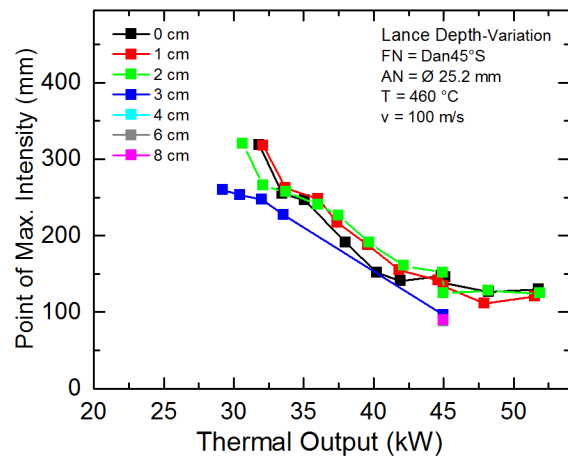
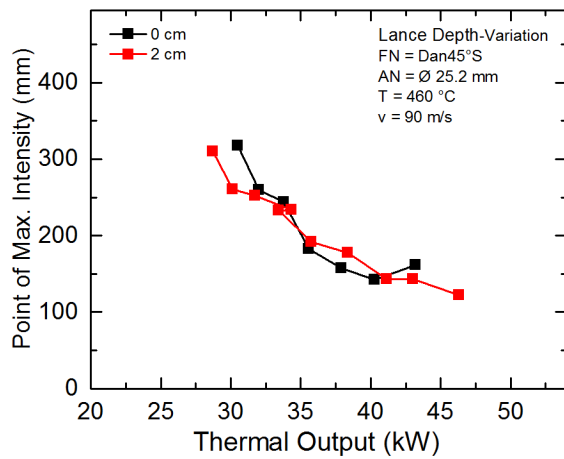
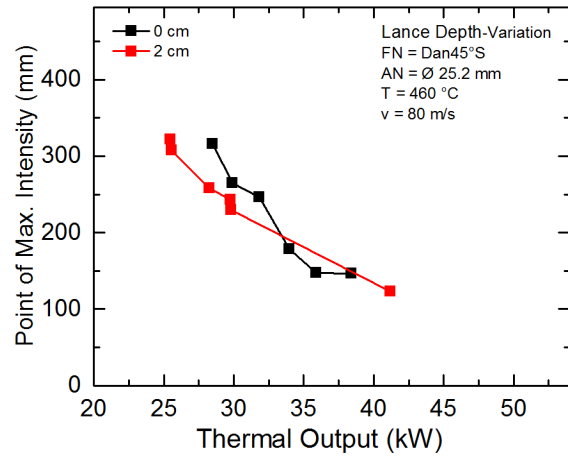
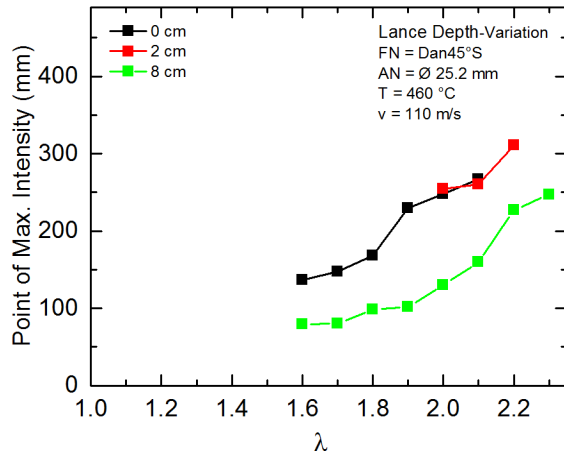
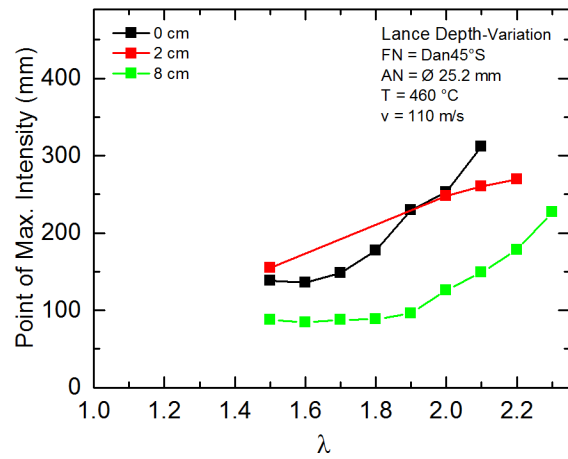
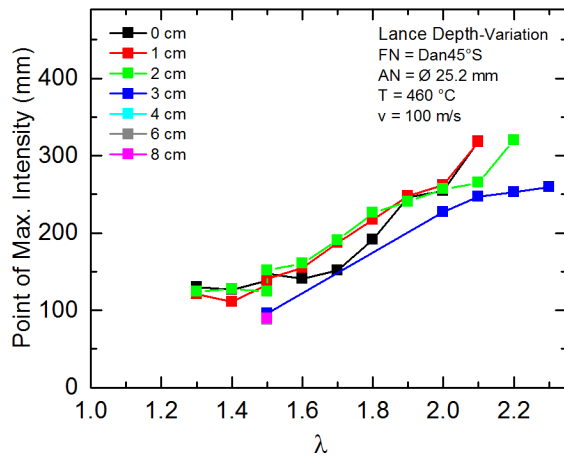
APPENDIX 4 GRAPHS: FLAME STRUCTURAL PROPERTIES

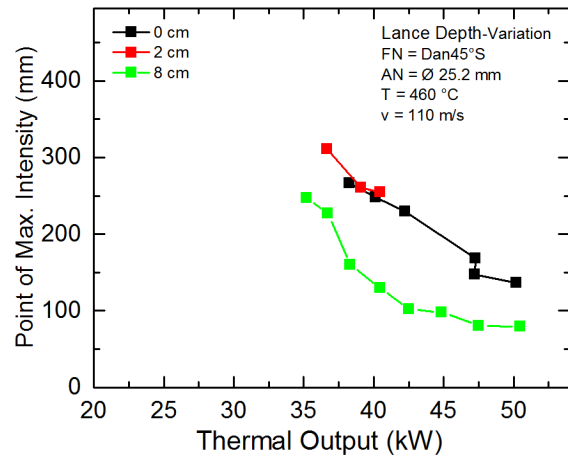
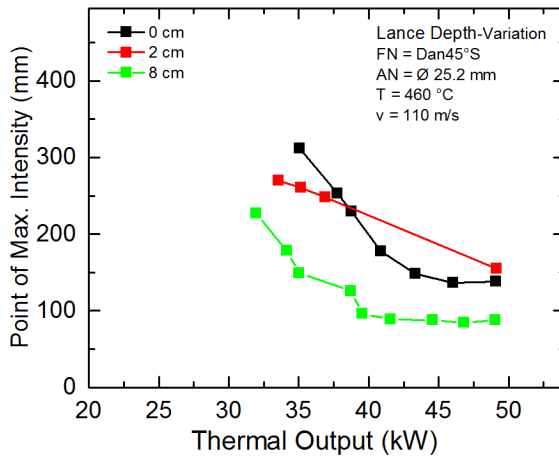
HAB vs. OH*-CL Intensity



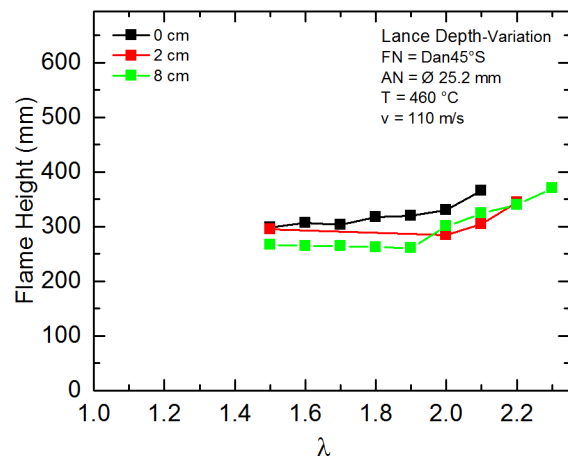
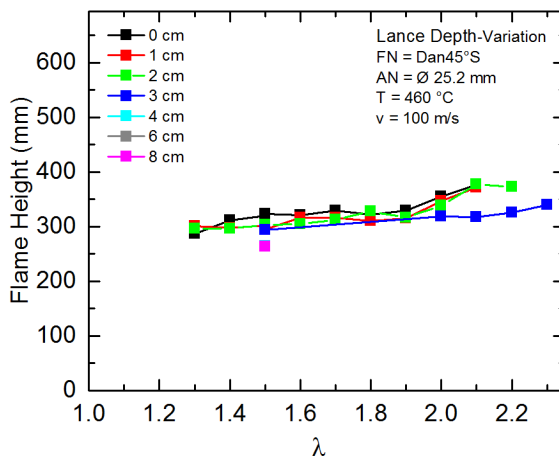
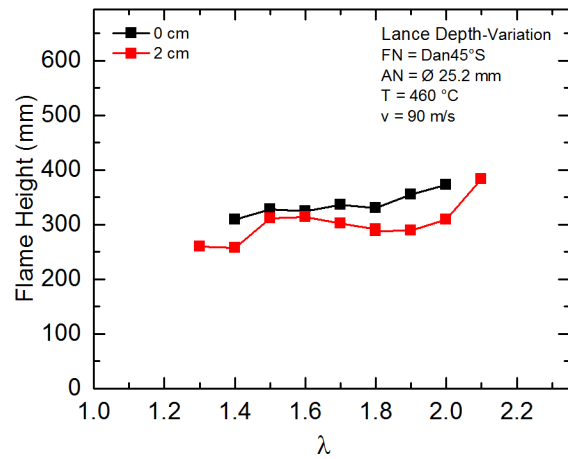
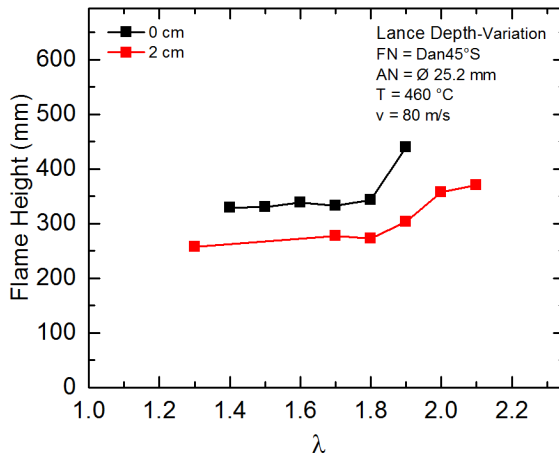
Dan45°S-LanceDepthVari-APMI

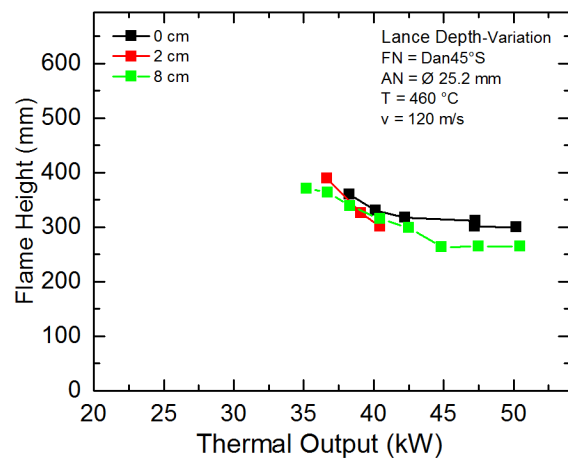
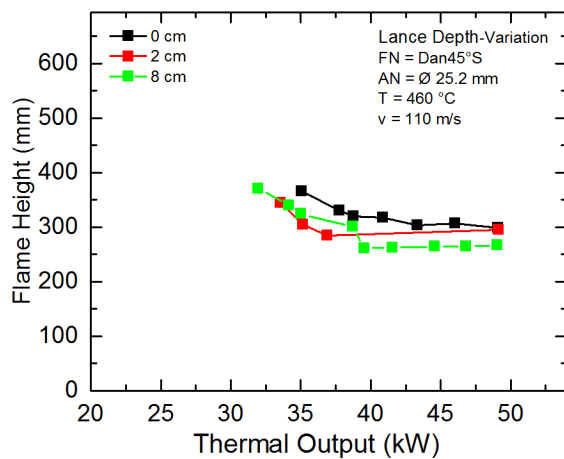
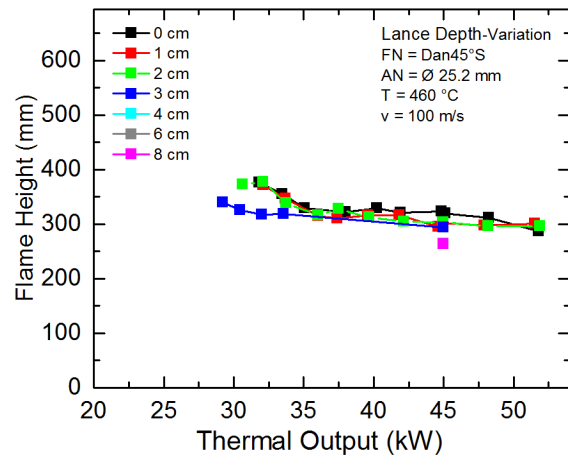
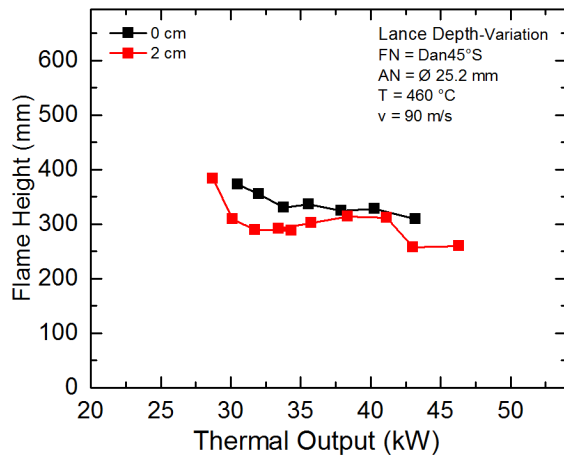
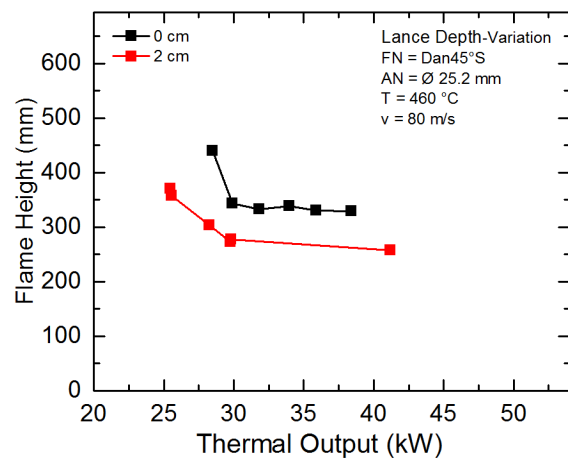
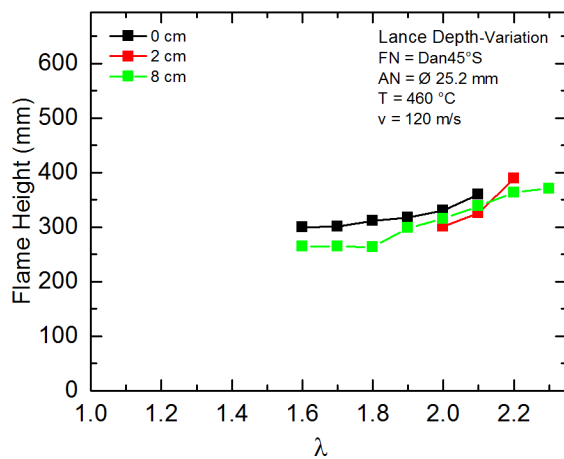




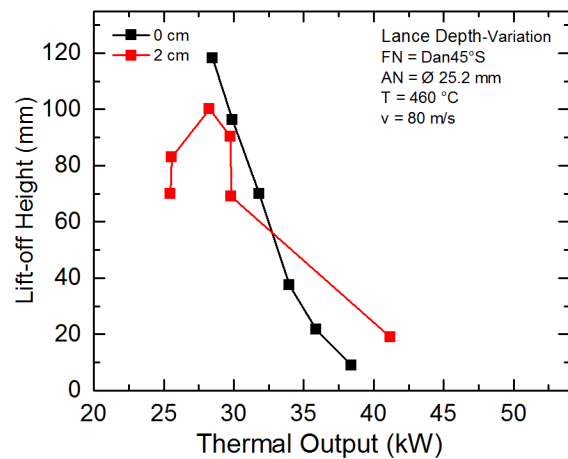
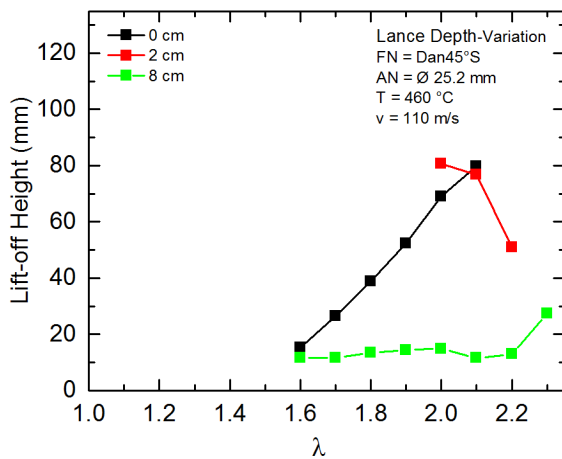
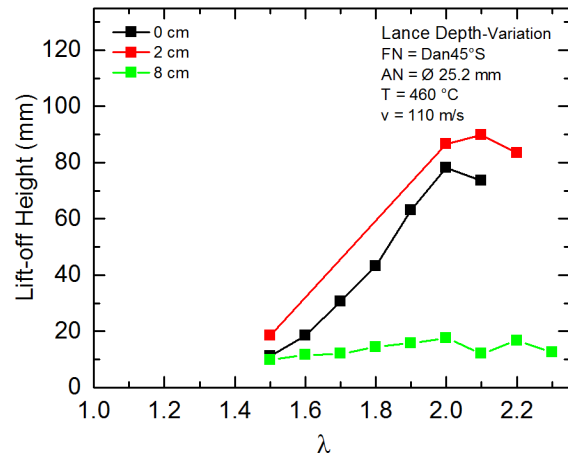
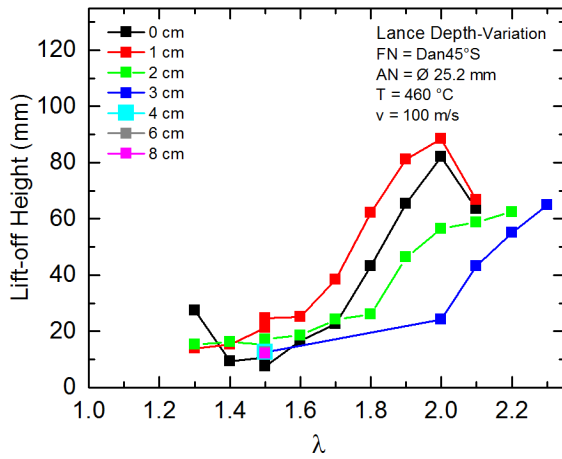
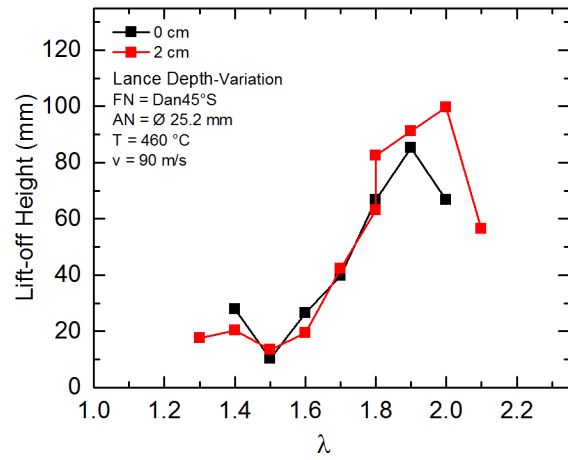
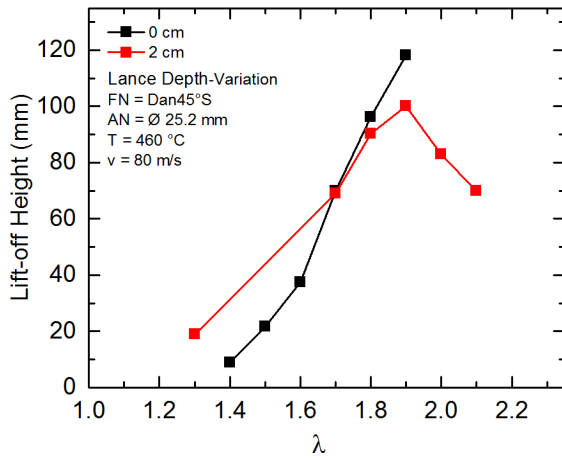


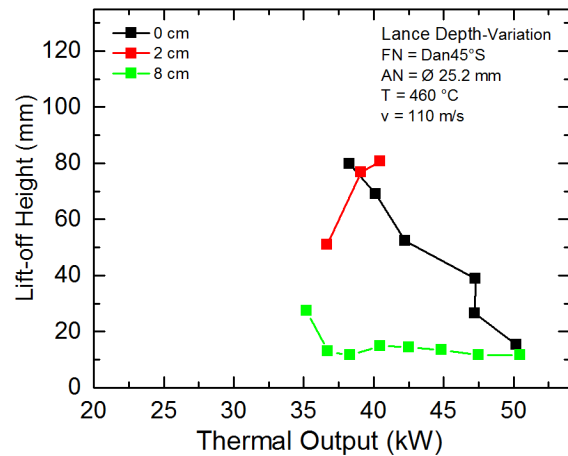
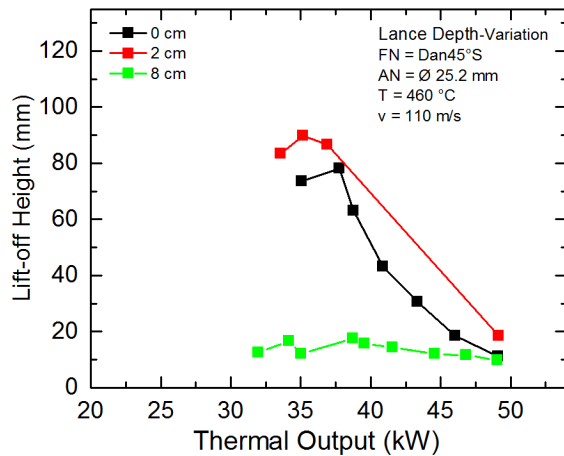
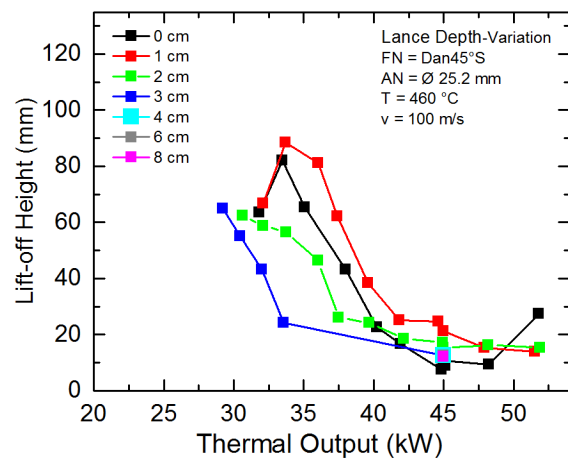
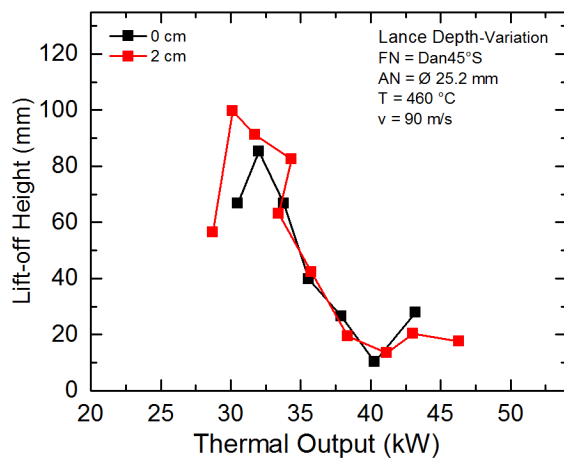
Dan45°S-LanceDepthVari-FH



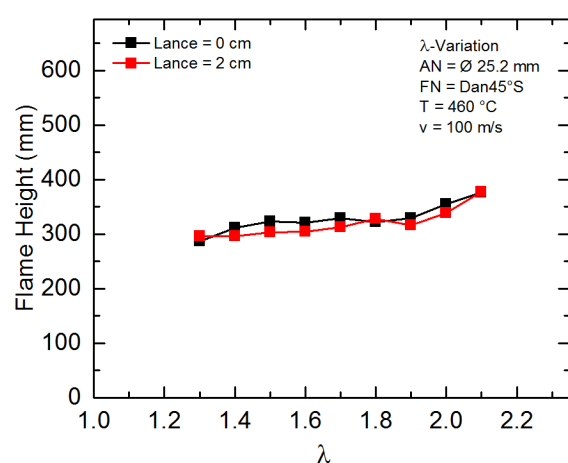
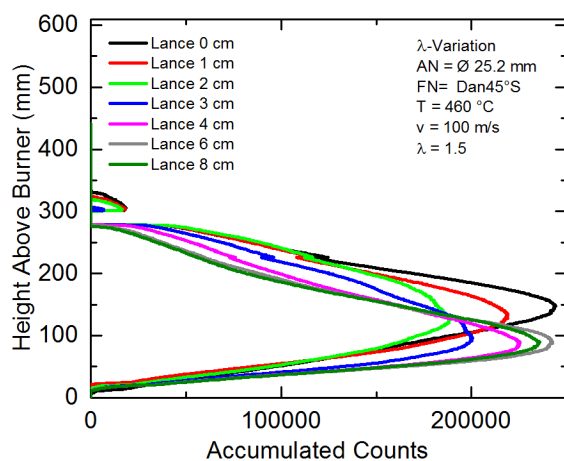


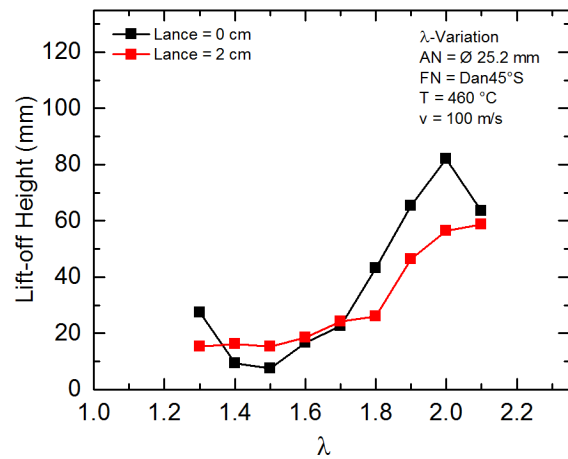
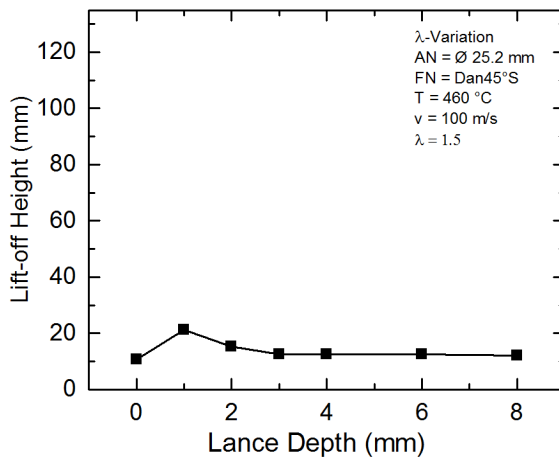
Dan45°S-LanceDepthVari-LOH



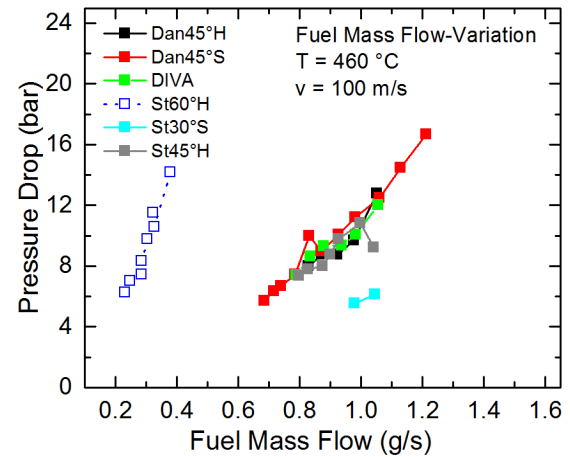
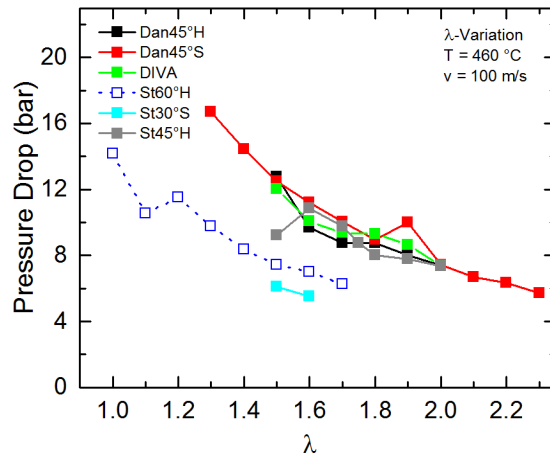


Lance Variation

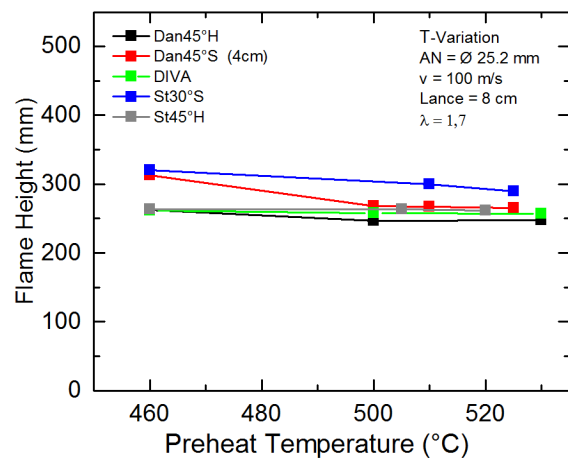
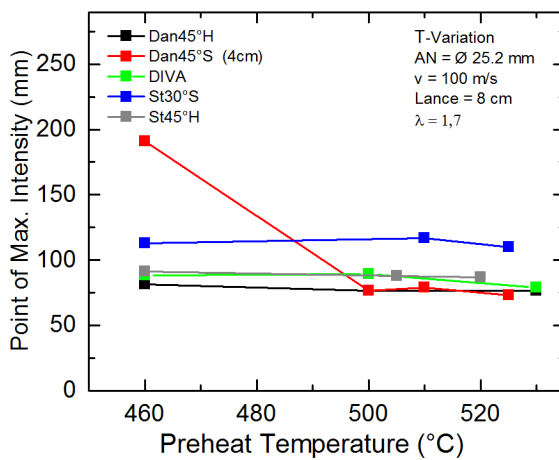


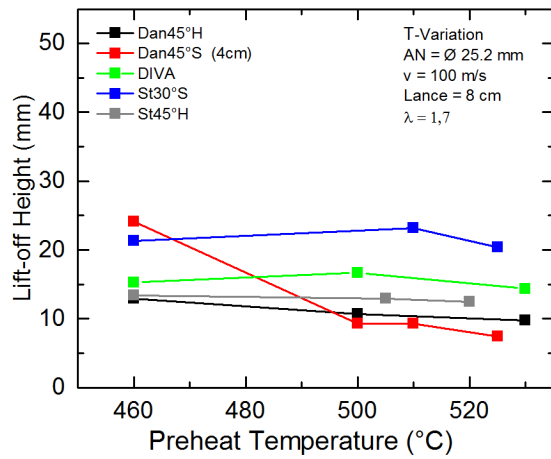


Pressure Drop

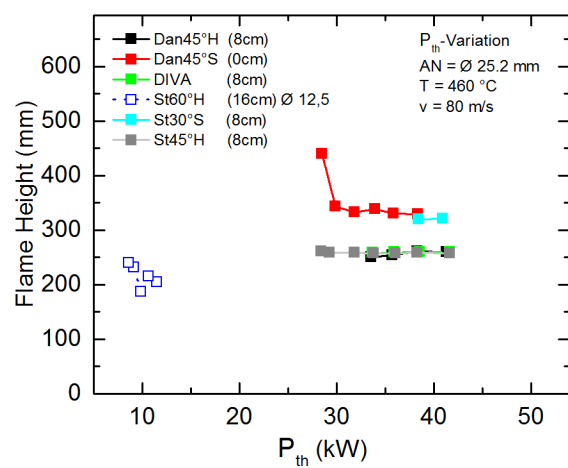
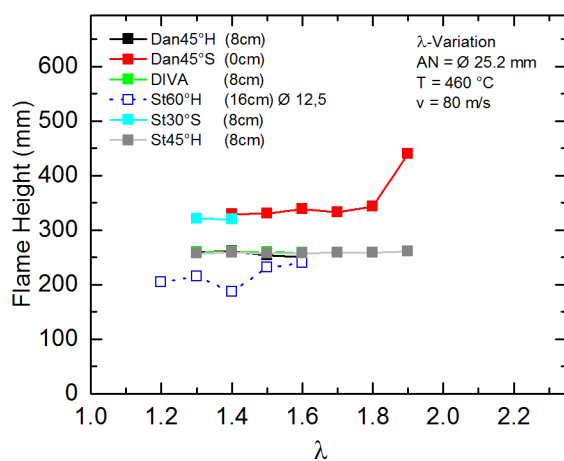
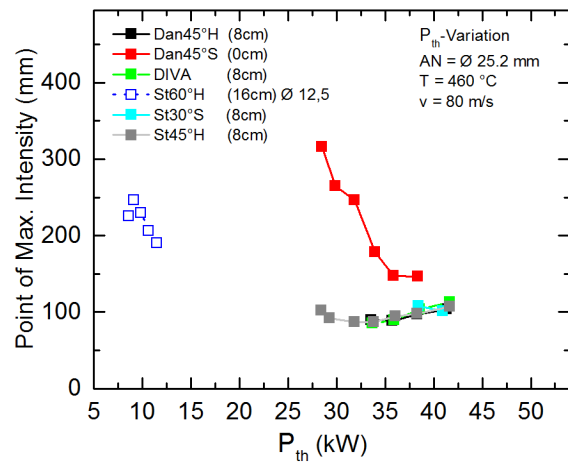
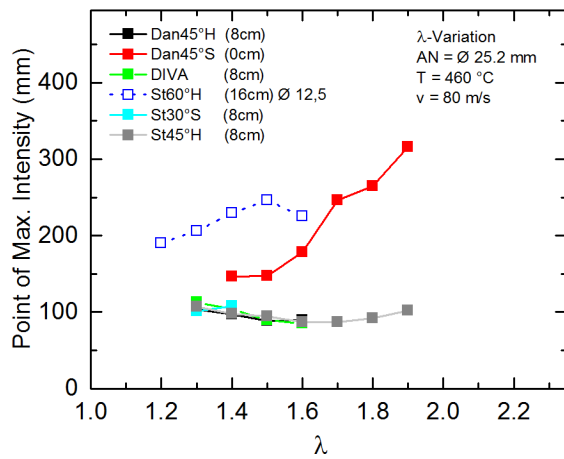


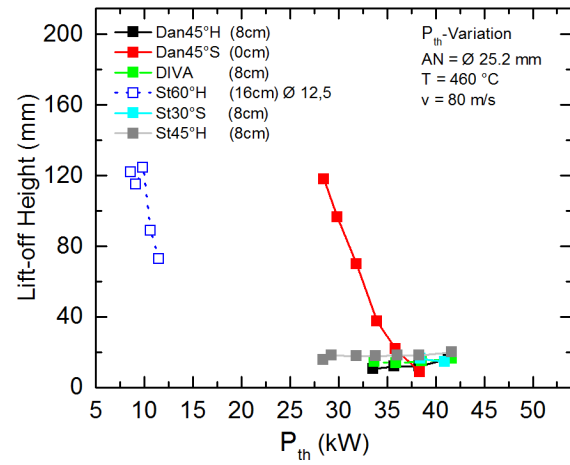
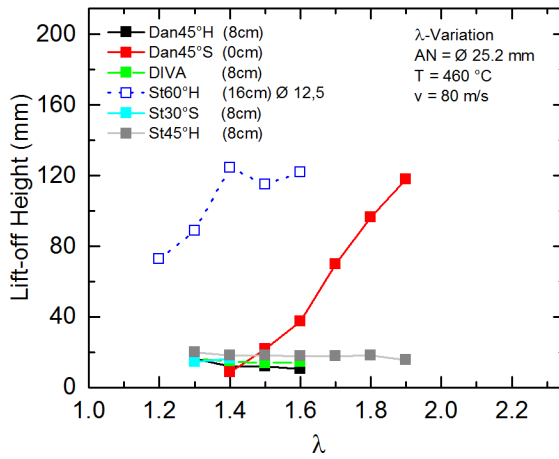
Air Preheat Temperature Variation



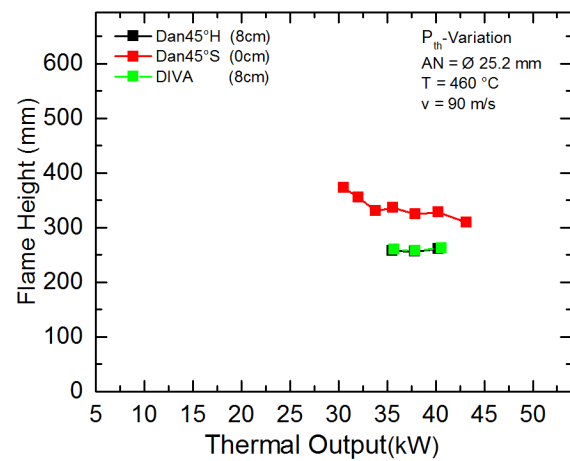
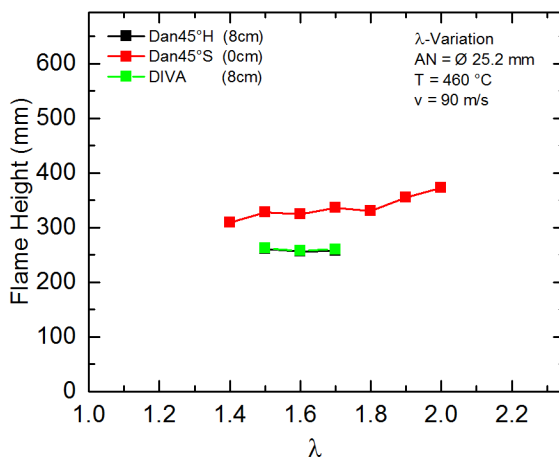
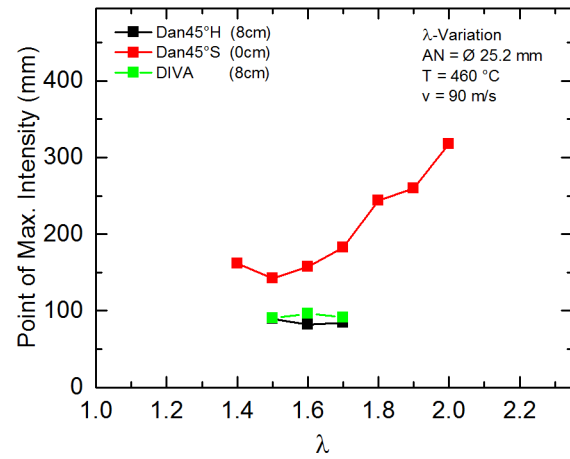
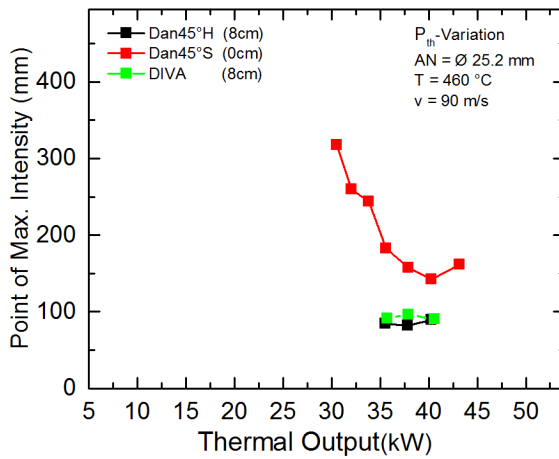


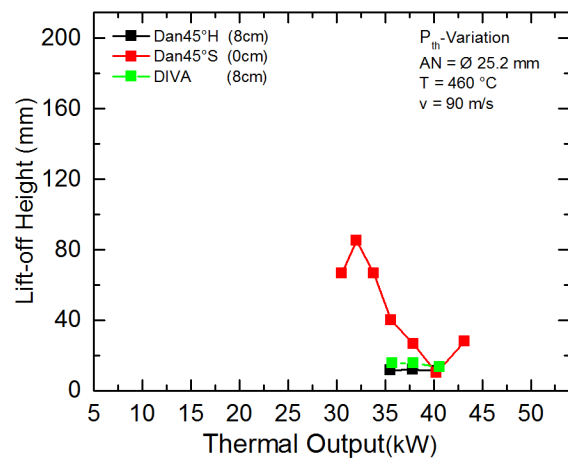
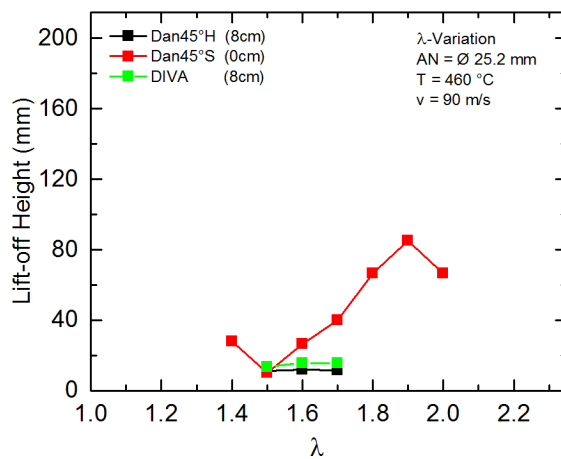
Constant Velocity 80 m/s



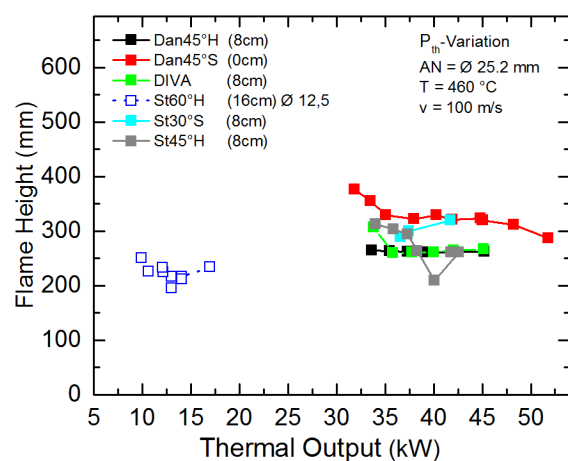
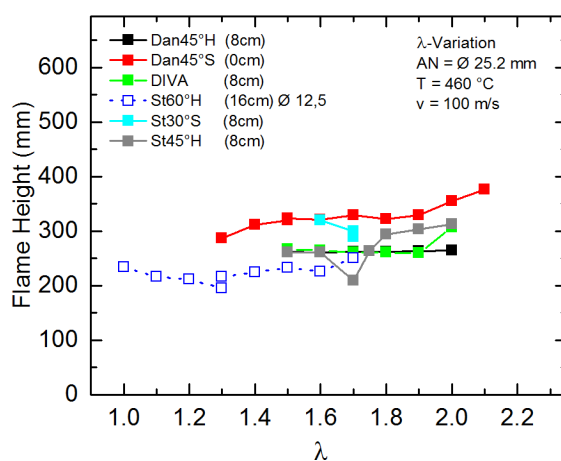
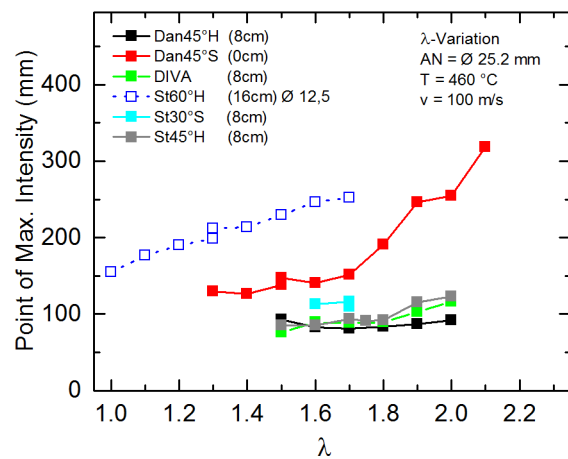
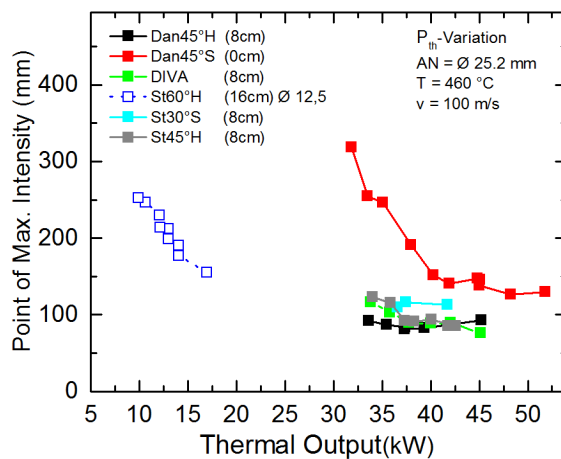


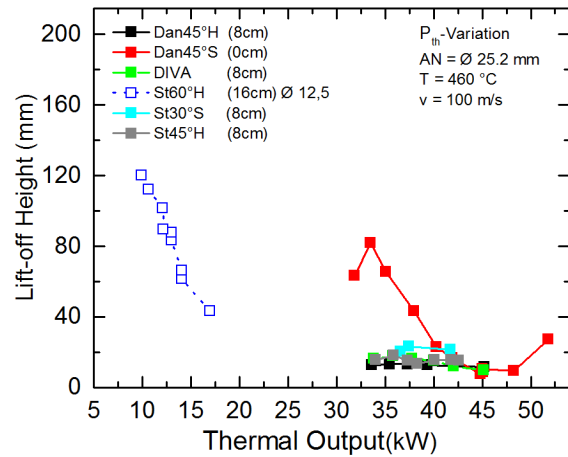
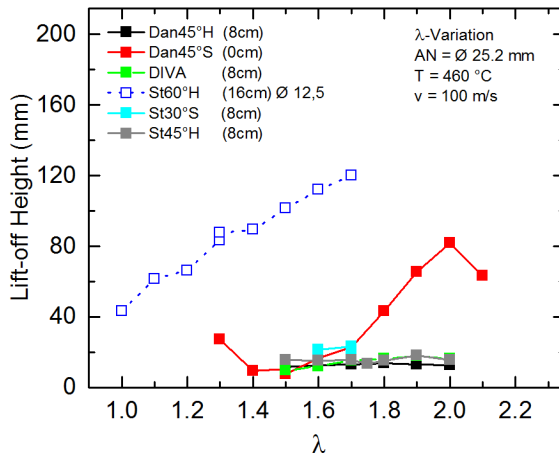
Constant Velocity 90 m/s



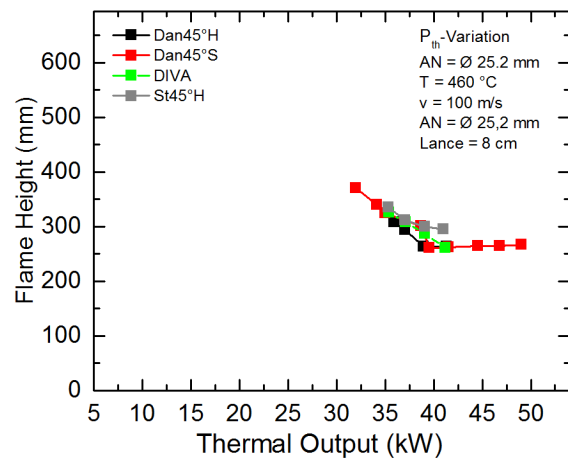
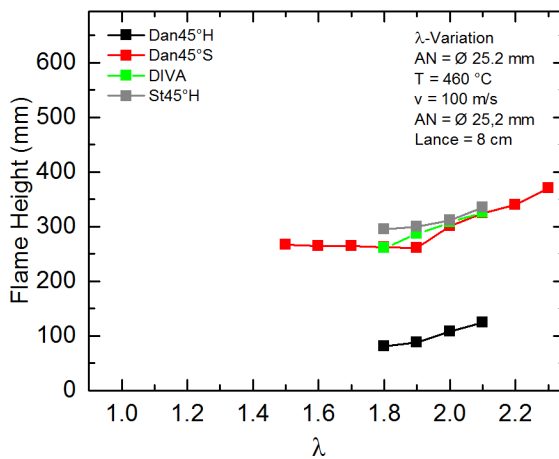
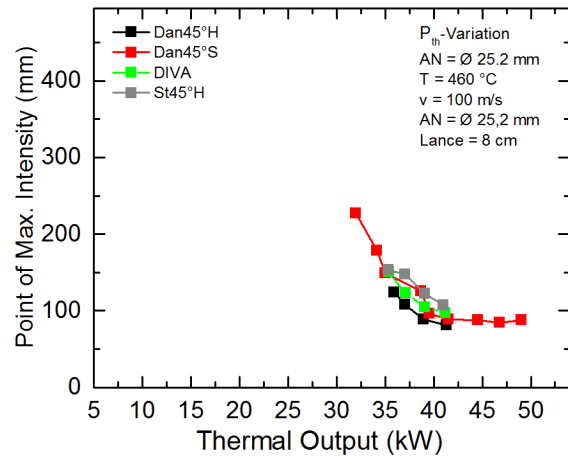
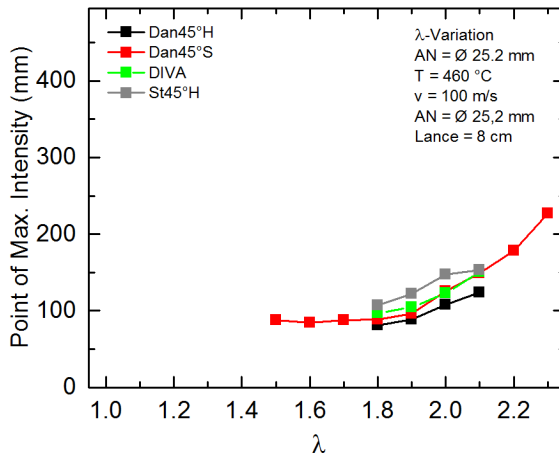


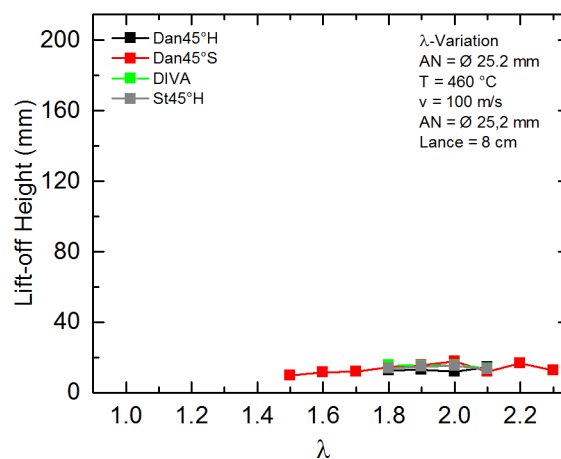
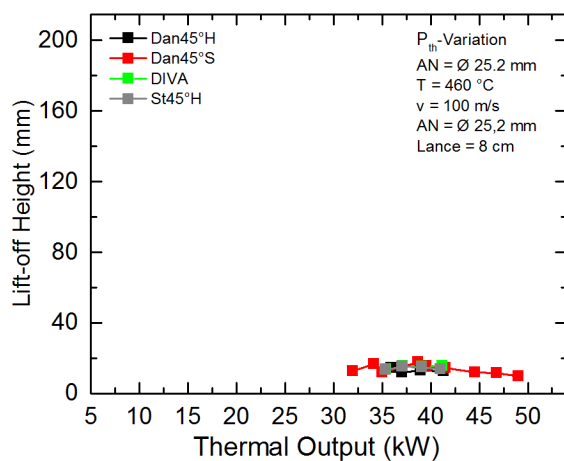
Constant Velocity 100 m/s



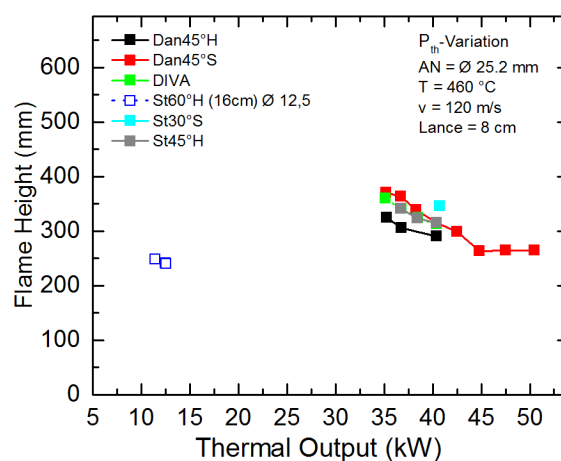
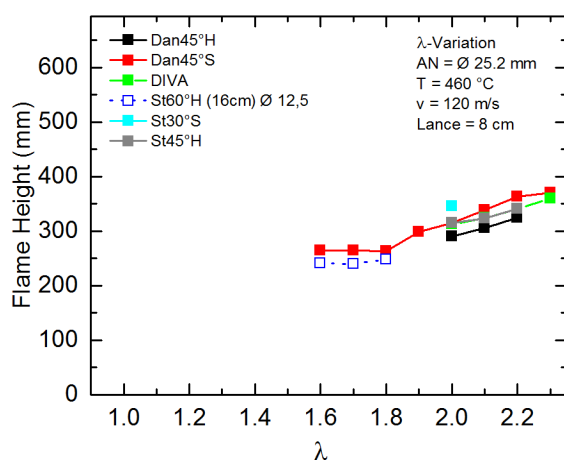
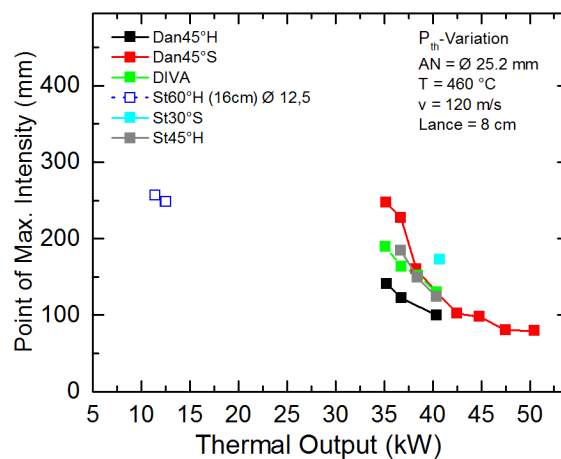
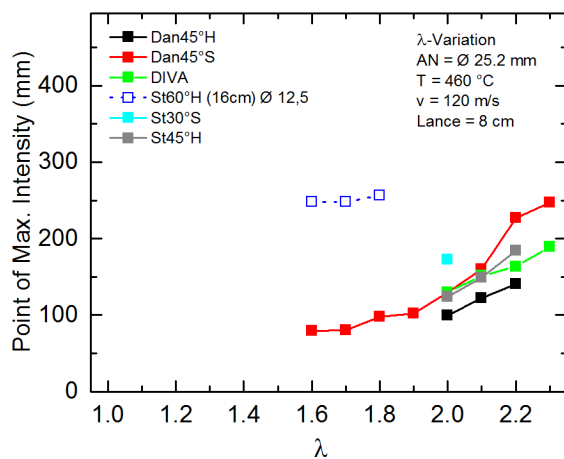


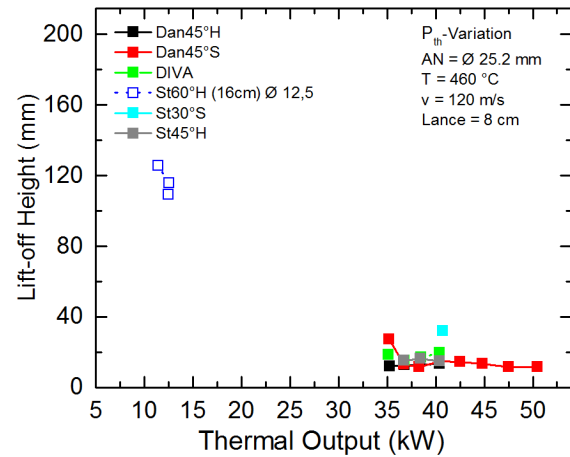
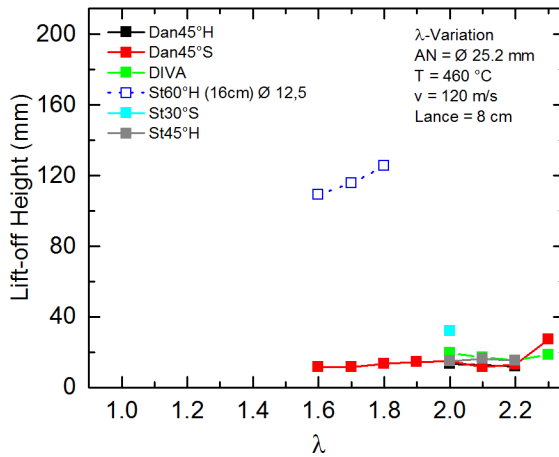
Constant Velocity 110 m/s





Constant Velocity 120 m/s





Air Velocity Variation

